UNIMORE
UNIVERSITÀ DEGLI STUDI DI
MODENA E REGGIO EMILIA

UNIVERSITÀ DEGLI STUDI
DI MODENA E REGGIO EMILIA

Dottorato di ricerca in "Physics and Nanosciences"

Ciclo XXXVIII

Modeling Correlated Excitons in Hybrid and Semiconductor Nanostructures

Tesi di Dottorato

Candidato: **Daniel López Díaz**

Relatore (Tutor): **Prof. Guido Goldoni**

Correlatori (Co-Tutors): **Prof. Stefano Corni, Dr. Gabriel Gil Pérez**

Coordinatore del Corso di Dottorato: **Prof. Marco Affronte**

Anno Accademico 2024–2025

Abstract

This thesis investigates how excitonic couplings and electron–hole correlations govern optical, photochemical, and transport phenomena in hybrid and semiconductor nanostructures. By adopting a unified excitonic framework, the present study bridges three representative platforms (chromophore–quantum dot nanohybrids, photoswitch–quantum dot nanohybrids, and coupled quantum wells driven by surface acoustic waves) demonstrating how excitonic correlations manifest across distinct physical systems.

A central focus is the accurate description of excitonic hybridization in assemblies of a chromophore and a quantum dot. To this end, the Hybrid Configuration Interaction (HyCI) framework is applied at its full theoretical scope for the first time through the explicit construction and diagonalization of the complete hybrid Hamiltonian. For a prototypical porphine–gallium nitride quantum dot nanohybrid, the results reveal the emergence of hybrid excitons characterized by avoided crossings in the excitation spectrum, accompanied by an exchange of molecular and nanoparticle character. The associated energy splittings are shown to be highly tunable with respect to quantum dot size, molecular orientation, and inter-fragment separation, and to follow clear scaling laws dominated by dipolar near-field interactions, with deviations arising from higher-order multipolar contributions involving optically dark quantum-dot states.

The thesis further identifies a previously unexplored, cavity-free mechanism for controlling photoisomerization in photoswitch–quantum dot nanohybrids. Applying HyCI for an azobenzene–cadmium selenide quantum dot system, intrinsic excitonic coupling is shown to induce avoided crossings on the excited-state potential energy surfaces along the photoisomerization coordinate. These crossings give rise to energy splittings of a few meV and to a redistribution of oscillator strength between molecular and quantum-dot excitations. The magnitude of these effects is tunable via material and geometric parameters, and operates on electronic timescales compatible with the intrinsic photoisomerization process.

Finally, the correlated two-body description of surface-acoustic-wave-driven transport of spatially indirect excitons in coupled quantum wells is extended to include localized screened impurity potentials, enabling the investigation of more realistic device scenarios. The results reveal correlation-driven transport regimes and pronounced asymmetries in exciton transmission beyond the reach of mean-field models.

Overall, this work establishes correlated excitons as the unifying physical principle underlying hybridization, photochemical control, and transport in hybrid and semiconductor nanostructures, and provides a robust theoretical foundation for the rational design of excitonic functionality.

Riassunto

Questa tesi analizza come le interazioni eccitoniche e le correlazioni tra elettroni e lacune influenzino i processi ottici, fotochimici e di trasporto in nanostrutture ibride e semiconduttori. Attraverso un approccio eccitonico unificato, il lavoro mette in relazione tre sistemi rappresentativi — nanohybrid cromoforo–quantum dot, nanohybrid fotoswitch–quantum dot e pozzi quantici accoppiati guidati da onde acustiche superficiali — evidenziando il ruolo comune delle correlazioni eccitoniche in contesti fisici differenti.

Una parte centrale dello studio è dedicata alla descrizione dell'ibridizzazione eccitonica in sistemi costituiti da una molecola e un quantum dot. A tal fine viene impiegato il formalismo Hybrid Configuration Interaction (HyCI), applicato per la prima volta nella sua formulazione completa mediante la costruzione esplicita dell'Hamiltoniana ibrida. Nel caso di un nanohybrid porfina–nitruro di gallio, emergono stati eccitonici ibridi caratterizzati da crossing evitati nello spettro di eccitazione, associati a un progressivo scambio di carattere tra componente molecolare e nanoparticellare. Gli splitting energetici risultano fortemente modulabili tramite parametri geometrici e materiali, come la dimensione del quantum dot, l'orientazione molecolare e la distanza tra i frammenti, e seguono leggi di scala dominate da interazioni dipolari di campo vicino, con contributi aggiuntivi dovuti a termini multipolari di ordine superiore e a stati otticamente scuri del quantum dot.

La tesi individua inoltre un meccanismo inedito, privo di cavità ottica, per il controllo della fotoisomerizzazione in nanohybrid fotoswitch–quantum dot. Nel sistema azobenzene–seleniuro di cadmio, l'accoppiamento eccitonico intrinseco induce crossing evitati sulle superfici di energia potenziale degli stati eccitati lungo la coordinata di reazione. Questi effetti portano a splitting energetici dell'ordine di pochi meV e a una ridistribuzione dell'intensità di transizione tra eccitazioni molecolari e del quantum dot. L'entità del fenomeno è regolabile attraverso parametri strutturali e materiali e si manifesta su scale temporali elettroniche compatibili con il processo di fotoisomerizzazione.

Infine, lo studio del trasporto di eccitoni indiretti spazialmente in pozzi quantici accoppiati, guidati da onde acustiche superficiali, viene esteso includendo impurità elettrostatiche schermate e localizzate. Questo permette di analizzare scenari più realistici per dispositivi, rivelando regimi di trasporto dominati dalle correlazioni e marcate asimmetrie nella trasmissione eccitonica che non emergono in trattamenti di tipo mean-field.

Nel loro insieme, i risultati mostrano come gli eccitoni correlati costituiscano l'elemento unificante alla base dei fenomeni di ibridizzazione, controllo fotochimico e trasporto in nanostrutture ibride e semiconduttori, fornendo un quadro teorico solido per la progettazione di nuove funzionalità eccitoniche.

To my mother, with the deepest love and admiration, to my father, and to my entire family.

Acknowledgments

I would like to express my deepest gratitude to my mother. Despite the distance, she has always been by my side, giving me her unconditional love and her time in both joyful and difficult moments. At the cost of enormous sacrifices, she has been my strongest support in every challenge I have faced. She has guided me toward becoming a better man every day of my life.

I am profoundly grateful to my father, who has supported me and contributed to shaping my path in the right direction. He has been my main inspiration as a scientist and a role model in my professional life.

I also wish to thank the rest of my family: my sister, my aunt, my uncle, my cousin, and especially my grandmother and grandfather, even though they are no longer physically with us. They have always been there for me, offering their love, support, and guidance in every circumstance. I am also thankful to my brother-in-law and my niece, who more recently became part of our family.

I am sincerely grateful to my advisors, Prof. Guido Goldoni, Prof. Stefano Corni, and Dr. Gabriel Gil Pérez, for guiding me throughout this project, sharing their knowledge, and contributing significantly to my development as a researcher. I would like to express special thanks to Dr. Gabriel Gil Pérez for his invaluable support in introducing me to this new field of research and for his continuous guidance and support throughout this PhD. I am also particularly grateful to Prof. Stefano Corni for trusting me and involving me in his current research project, as well as to Prof. Guido Goldoni for his support and understanding during my arrival in Italy and the bureaucratic challenges that accompanied it. I also thank Prof. Andrea Bertoni and Prof. Federico Grasselli for the useful discussions regarding some of the computer programs employed in this work.

During these three years, I have been fortunate to meet wonderful friends, many of whom are fellow scientists, who made me feel at home here in Italy. I would especially like to thank Michael Hernández, Olive Gonda, Darío and Daniela León, and Frank Quintela for sharing travels, laughter, and conversations that helped me step away from work and maintain balance. I am also grateful to Alessandro Bello, Davide Palma, Antonio Solida, and Matteo D'Alessio, as well as many colleagues from Physics, Chemistry, and Computer Engineering, with whom I shared many meaningful moments. I would also like to thank Payam, Erick, and Hamed for the good moments and conversations we shared.

It is difficult to mention everyone who has contributed in one way or another to this stage of my life without unintentionally leaving someone out. To all of you, thank you very much.

Contents

List of Figures

List of Tables

Chapter 1

Introduction

This chapter introduces the physical context and conceptual foundations underlying the work presented in this thesis. After outlining the general characteristics and applications of hybrid and semiconductor nanostructures (Section 1.1), the discussion focuses on three representative platforms—chromophore–quantum dot nanohybrids, photoswitch–quantum dot nanohybrids, and coupled quantum wells— that exemplify different manifestations of excitonic control phenomena (Section 1.2). Particular attention is given to how excitonic couplings and electron–hole correlations emerge in these systems and enable control over optical response, photochemical pathways, and transport. The chapter then reviews the theoretical challenges associated with modeling such excitations across disparate length scales and materials, motivating the methodologies adopted in this work (Section 1.3). Finally, the scope, research questions, objectives and overall structure of the thesis are explicitly defined (Section 1.4).

1.1 Hybrid and semiconductor nanostructures: general description and applications

Hybrid nanostructures comprise a broad class of systems in which multiple organic and inorganic components with characteristic dimensions below 100 nm are integrated to realize optical and electronic functionalities that cannot be achieved by the individual constituents alone. [1, 2, 3] By combining distinct physical mechanisms and interactions arising from the underlying building blocks, these systems provide a versatile platform for emergent collective phenomena and tailored light–matter functionality in (bio-) optoelectronics. [4, 5, 6] In this work, hybrid nanostructures are defined as such independently of the specific embedding environment, including solution, mesoporous films, biomolecular scaffolds, or solid-state matrices.

A large class of hybrid nanostructures incorporate small organic molecules (Ms) -with sizes typically below 10 nm- coupled to inorganic nanoparticles (NPs) -with sizes below 100 nm, forming molecule-nanoparticle (M-NP) nanohybrids (Fig. 1.1). [7, 8, 9, 10, 11] Discrete optical transitions arising from quantum confinement and excitonic or polaritonic responses enhance the functionalities of these assemblies. [12, 13, 14, 15, 16] In particular, coupling Ms with NPs enables efficient energy and charge transfer across the hybrid interface. [17, 18, 19, 20, 21]

As a result, M-NP nanohybrids have been widely explored in technologically and medically relevant contexts, including applications in biomedicine, [22, 23, 24, 25] photocatalysis, [26, 27,

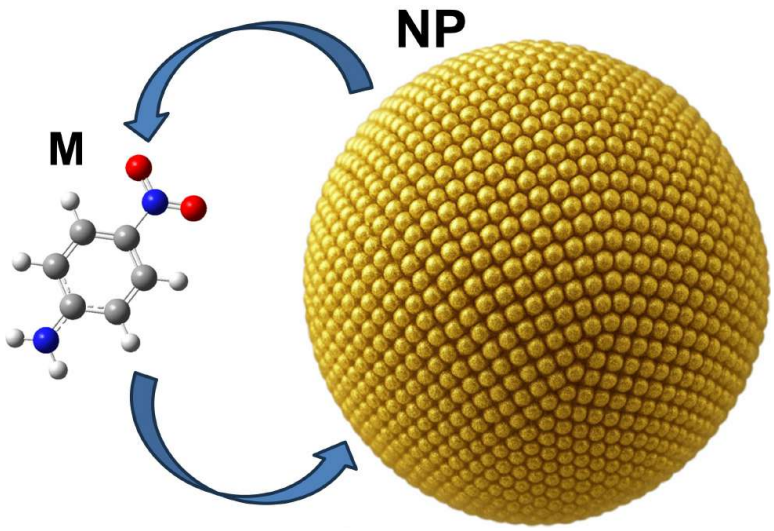

Figure 1.1: Schematic representation of a M–NP nanohybrid in which an organic molecule (p-nitroaniline) is coupled to a gold nanoparticle. Bidirectional energy- and charge-transfer processes (arrows) are typical in such assemblies.

28, 29] and (bio-) sensing [23, 24, 30, 31] These diverse applications exploit the ability of M-NP nanohybrids to transduce light into chemical, electrical, or mechanical function through controlled interactions and environments.

Chromophores (CPhs) constitute a particularly important subset of Ms in hybrid nanostructures due to their strong excited-state transitions, generally in the visible/UV spectral region, which enable them to act as bright natural or artificial transducers of light. [32, 33, 34] In addition, their modular chemical structure allows systematic modification of orientation, rigidity, functional groups, and symmetry. [35, 36] This structural control is essential for engineering molecules that interface efficiently with inorganic partners and can participate in processes such as charge separation and directional energy/charge flow within nanohybrids. [37, 38, 39]

A prototypical CPh is porphine (known as H_2P), the simplest member of the porphyrin family (Fig. 1.2). Although H_2P itself is rarely used in applications, its well-defined tetrapyrrolic macrocycle forms the archetype for porphyrin-based CPhs. These systems retain the characteristic strong Soret (UV) and Q-band (visible) absorption associated with extended conjugated π-systems. [40, 41, 42, 43] Such optical and electronic characteristics underpin the widespread use of porphyrins in photocatalysis, [44, 45, 46] energy conversion, [47, 48] photodynamic therapy, [49, 50, 51], optoelectronics, [52, 53, 54] and (bio-) sensing. [55, 56, 57]

Another relevant class of Ms in nanohybrids are photoswitches (PhSs), which constitute a family of compounds capable of undergoing reversible structural changes upon light absorption. [58, 59] These transformations typically involve E-Z isomerization, ring opening/closing, proton/electron transfer, or changes in aromaticity. [60, 61, 62, 63] Photoswitches are valued for their ability to convert optical energy into mechanical, electronic, or chemical responses, enabling dynamic control over molecular conformation, dipole orientation, and function. [64, 65] Their photochemical cycles often proceed via excited-state pathways that efficiently funnel population back to a different ground-state configuration, [66, 67] rendering them essential for applications in molecular electronics and light-controlled nanosystems. [68, 69, 70, 71]

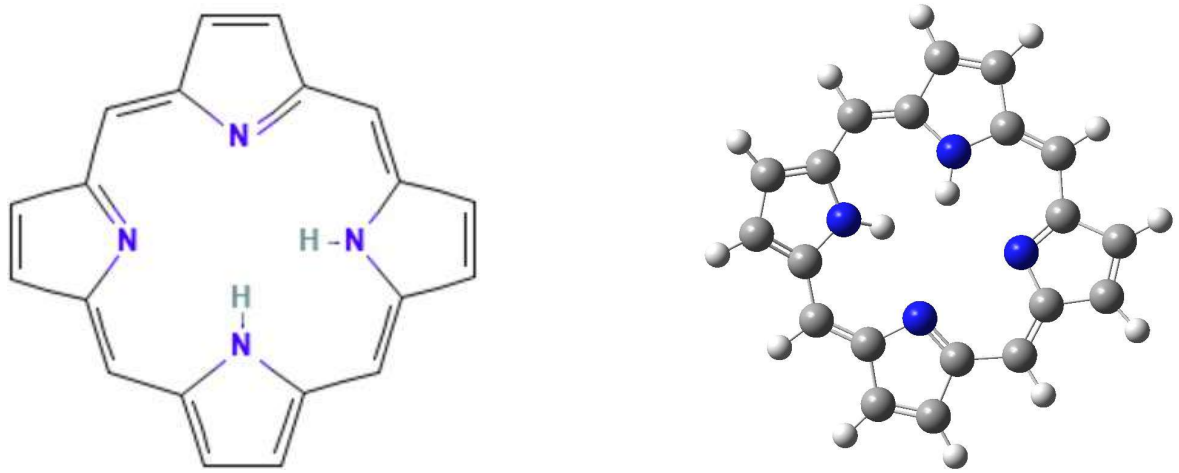

(a) (b)

Figure 1.2: Molecular structure of porphine (H_2P), the parent compound of free-base porphyrins. (a) Planar skeletal representation highlighting the tetrapyrrolic macrocycle formed by four pyrrole units linked via methine bridges. (b) Three-dimensional representation of H_2P, showing the nearly planar conjugated π-system and the two inner N-H bonds oriented toward the macrocycle center.

Among the many known photoswitchable scaffolds, azobenzene (hereafter abbreviated as AZB) and its derivatives represent the simplest and canonical class (Fig. 1.3). [72, 73] Upon photoexcitation, AZB undergoes reversible geometric rearrangement between its *trans* and *cis* configurations, a process collectively referred to as *trans-cis* photoisomerization. This reaction proceeds through a conical intersection, a nonadiabatic region of the potential energy surface (PES) where electronic states become nearly degenerate and enable rapid internal conversion back to the ground state. [74, 75] Modern theoretical and ultrafast spectroscopic studies have clarified that the C–N=N torsion and C–N=N–C dihedral angles are the key nuclear coordinates dominating the ultrafast photoisomerization dynamics (∼1 ps), [76, 77] as well as the comparatively long timescales (∼1 day) associated with thermal back-relaxation from ground-state *cis* to *trans*. [78, 79] These mechanistic insights underpin ongoing efforts to harness AZB derivatives in nanohybrids for solar-thermal energy storage, opto-mechanical actuation, and nanoscale information processing, where light-driven switching of molecular conformation enables the reversible manipulation of energy and function. [80, 81, 82]

Inorganic NPs, ranging from metal, dielectric, and semiconductor types, offer complementary optical and electronic capabilities within hybrid nanostructures. [83, 84, 85] They include plasmonic metal systems with strong near fields enhancement limited by Ohmic losses, [86,87,88] as well as as high-index dielectric nanoantennas that sustain low-loss electric and magnetic Mie resonances for controlled field confinement and directional scattering. [89, 90]

A widely employed class of NPs in hybrid nanostructures are quantum dots (QDs). [91, 92] These systems -typically smaller than 10 nm and composed of semiconductor materials such as cadmium selenide (CdSe) or gallium nitride (GaN)- are strongly quantum confined in all three dimensions and support discrete electronic states. As a consequence, they are characterized by size-tunable band gaps, high oscillator strengths, and narrow absorption and emission features. [93, 94] In hybrid architectures, their exceptional photostability, large absorption cross sections,

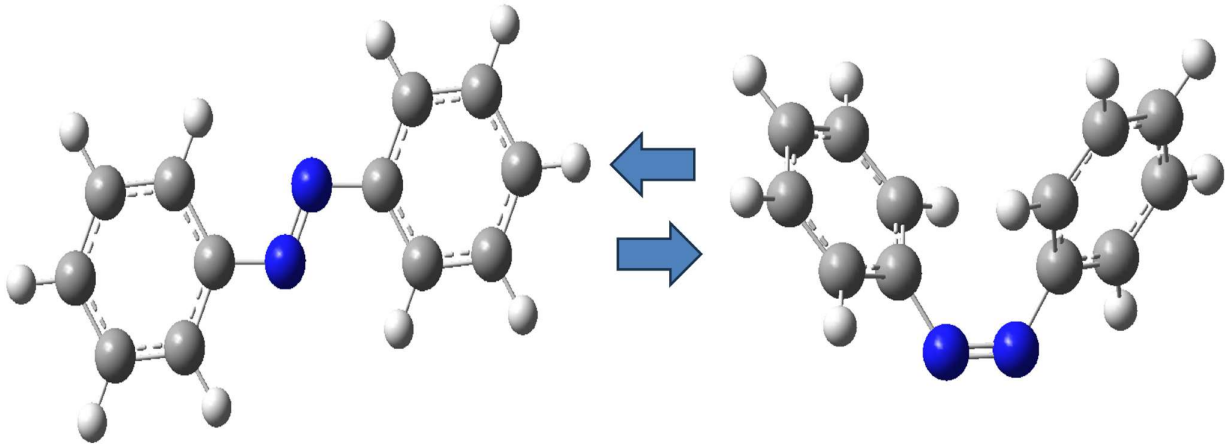

Figure 1.3: Schematic of photoisomerization in azobenzene (AZB). The molecule undergoes reversible switching (arrows) between its *trans* (left) and *cis* (right) configurations upon photoexcitation. These structural changes are mediated by passage through a conical intersection on the excited-state PES. The dominant nuclear coordinates driving this motion are the C–N=N torsion and the C–N=N–C dihedral angles. Thermal relaxation from the ground-state *cis* back to *trans* occurs on much longer timescales than photoisomerization.

and high quantum yields enable QDs to act as bright excitonic donors and acceptors, facilitating efficient energy and charge transfer with organic and inorganic partners. [95, 96] Moreover, multiexciton generation pathways distinguish them from molecular CPhs and enhance carrier-generation efficiency in nanoscale photocatalytic or photovoltaic hybrid assemblies. [97, 98]

Taken together, systems of CPhs or PhSs coupled to QDs (CPh-QD or PhS-QD) offer complementary photophysical characteristics. Organic molecules typically display relatively narrow and chemically tunable absorption bands but often suffer from shorter excited-state lifetimes and susceptibility to photobleaching. [32, 33] In contrast, QDs exhibit broad absorption with size-tunable band gaps, narrow emission lines, enhanced photostability, and longer-lived excitations. [91, 93] Hybrid nanostructures can leverage these complementary behaviors by combining molecular selectivity and synthetic modularity with the robust, tunable optical response of QDs.

Beyond organic–inorganic hybrid assemblies, a complementary and conceptually distinct approach to controlling electronic excitations is offered by purely inorganic semiconductor nanostructures. These systems constitute a broad class of nanoscale architectures in which low-dimensional semiconductor components are combined to engineer tailored excitation landscapes. Representative examples include heterostructures such as nanowires, which form quasi-one-dimensional crystals, and layered van der Waals stacks composed of atomically thin sheets. These platforms enable precise control over quantum confinement, dielectric contrast, and band alignment. [11, 99, 100] By coupling these semiconductor building blocks, complex potential landscapes can be realized that support device-relevant excitation control, enabling applications in photodetection, energy harvesting, optical modulation, and excitonic circuitry beyond the capabilities of individual elements. [101, 102]

Within this broader class of semiconductor nanostructures, coupled quantum wells (CQWs) constitute a prototypical inorganic platform composed of two thin semiconductor layers (quantum wells) separated by a narrow barrier, forming a precisely engineered multilayer struc-

ture. [103, 104] This configuration supports charge carriers residing in adjacent wells, whose spatial separation and energetics can be reconfigured through structural design or external fields. [103, 105] Such tunability has established CQWs as a central platform for applications including excitonic transistors, electro-optic modulators, photonic switches, and on-chip signal-routing schemes. [106, 107]

Across all these nanosystems, functionality ultimately rests on how electronic excitations are generated, redistributed, and converted. A natural framework for describing such neutral excitations is provided by excitons, quasiparticles formed by correlated electron–hole pairs. [99] The nature of these excitons depends sensitively on the host material: in organic molecules such as CPhs and PhSs, electronic excitation is tightly localized, giving rise to strongly bound Frenkel excitons, whereas QDs and CQWs support Wannier–Mott excitons whose spatially extended character reflects reduced dielectric screening and quantum confinement. [108, 109]

This excitonic modulation provides a common language for the three nanosystems examined in this thesis: (i) chromophore-quantum-dot (CPh-QD) assemblies, (ii) photoswitch-quantum-dot (PhS-QD) nanohybrids, and (iii) coupled quantum wells with surface acoustic waves (CQW-SAW). Accordingly, the next section reviews the state of the art in exciton control within these representative platforms.

1.2 Exciton-driven control in hybrid and semiconductor nanostructures

In what follows, *exciton-driven control* refers to the deliberate use of electronic structure, couplings, and transport to tailor optical response and energy flow in hybrid and semiconductor nanostructures. By tuning quantum confinement, structural geometry, external fields, or nanophotonic environments, one can reshape exciton energies, wavefunctions, and lifetimes beyond what is achievable in isolated molecular or semiconductor components. [4, 5]

In CPh-QD nanohybrids, excitonic control governs resonance energy transfer, hybrid transition dipoles, and charge-separation processes. [17, 33] Subtle variations in orientation, spectral alignment, or intermolecular spacing between the CPh and the QD can selectively enhance or suppress exciton transfer, making CPh-QD assemblies versatile mediators of photoinduced energy and charge. [12] The extended electronic structure and multipolar response of NPs can enable anisotropic and geometry-dependent exciton-transfer pathways, opening routes to polarization-sensitive hybrid emitters and directionally selective energy funnels. [12, 18, 19]

A more specialized realization of excitonic control arises in PhS-QD nanohybrids. To date, modulation of photoisomerization in PhSs has been pursued predominantly through *polaritonic* strategies, [110, 111, 112, 113, 114] in which molecular excitations couple strongly to confined electromagnetic modes in resonant cavities. [115, 116, 117, 118] Such states have been shown to modify photochemical reactivity in PhSs by reshaping the pathways of photoisomerization. [16, 119, 120, 121] Particularly in AZB, these hybrid light-matter states can restructure the excited-state PESs, introducing cavity-induced avoided crossings that significantly alter quantum yields and modify excited-state lifetimes. [76, 77, 122, 123, 124] Recent advances in *open photonic* architectures -including waveguides, epsilon-near-zero materials, and dielectric metasurfaces- have further extended this modality beyond traditional Fabry–Pérot cavities, enabling strong coupling and photoswitching control in mirrorless platforms. [125,126,127,128,129]

By contrast, *intrinsic excitonic interactions* in PhS-QD hybrids, where a single photoswitch couples directly to a quantum-confined semiconductor exciton, remain far less explored than their polaritonic counterparts. Although typically weaker than cavity-induced interactions, this cavity-free mechanism offers several appealing features. Excitonic coupling can naturally generate avoided crossings on excited-state PESs, modulate absorption spectra, and influence energy-transfer pathways. [130] Moreover, the relevant electronic coherences and population dynamics occur on nanosecond timescales, [95] far longer than the ultrafast (∼10 fs) lifetimes of polaritonic states, [76, 77] and therefore align more closely with the intrinsic timescale of photoisomerization (∼1 ps). [78, 79]

This thesis introduces and analyzes the first proposal for such a cavity-free, exciton-driven control mechanism. In particular, we investigate how geometric and materials parameters —such as QD size and PhS orientation— govern the emergence of avoided crossings that reshape the hybrid PES and modify the underlying excited-state manifold. A schematic of a PhS-QD system and the corresponding avoided crossing induced by excitonic coupling is shown in Fig. 1.4.

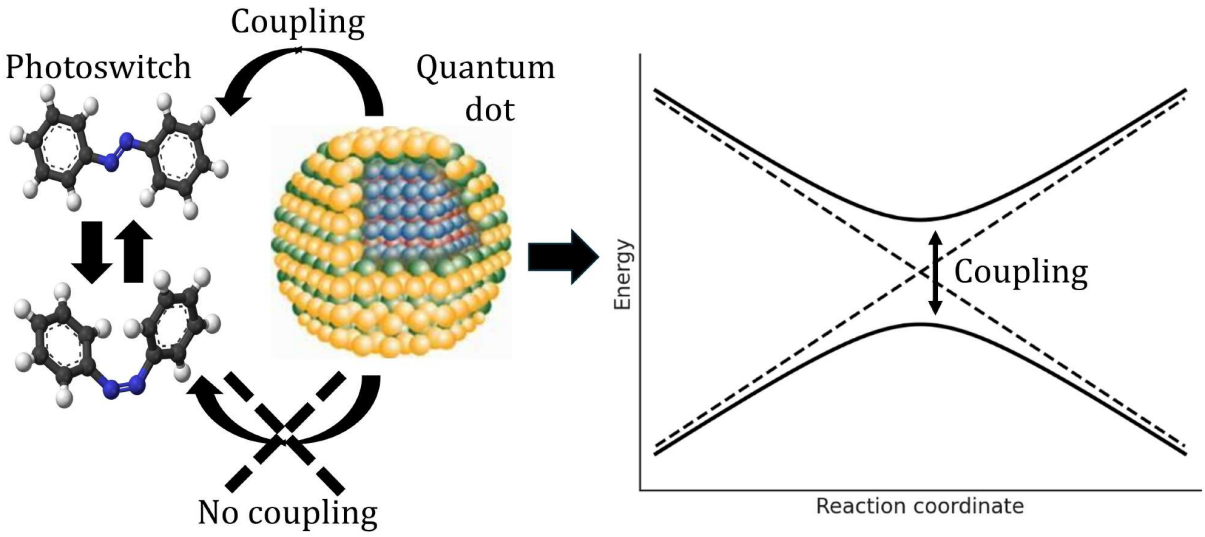

Figure 1.4: Schematic representation of a PhS-QD nanohybrid studied in this work. The figure shows an AZB molecule functionalized with a QD and illustrates the key feature: hybrid PhS-QD states exhibit avoided crossings when the tunable excitonic coupling is present (solid lines), thereby altering the energy pathways for photoisomerization dynamics, in contrast to the uncoupled case (dashed lines), where the states simply cross.

In CQWs, excitonic control takes place in an extended solid-state environment, where electronic excitations are not confined in all dimensions and can propagate across tailored potential landscapes. Within the excitonic framework introduced above, charge carriers residing in adjacent wells are naturally described as spatially indirect excitons (SIXs), whose long lifetimes and intrinsic dipole moments make them particularly suitable for external manipulation. [103] Gate fields and engineered confinement enable the tuning of the energetics and spatial distribution of SIXs while preserving their excitonic character.

A particularly powerful form of control is realized when SIXs are driven by surface acoustic

waves (SAWs). The strain and piezoelectric fields associated with a SAW generate moving potentials that can capture, transport, and release SIXs over micrometer distances. This dynamic modulation enables the routing of optical excitations across gate-defined architectures and the conversion of exciton populations into optical signals through radiative recombination. [131, 132] Recent experiments have demonstrated high-fidelity SAW-driven transport of SIXs and their controlled conversion into single photons at gigahertz repetition rates, including the remote population of localized impurity-bound centers acting as single-exciton qubits. [133] A schematic illustration of a SAW-driven SIX in a CQW in the presence of a localized impurity is shown in Fig. 1.5.

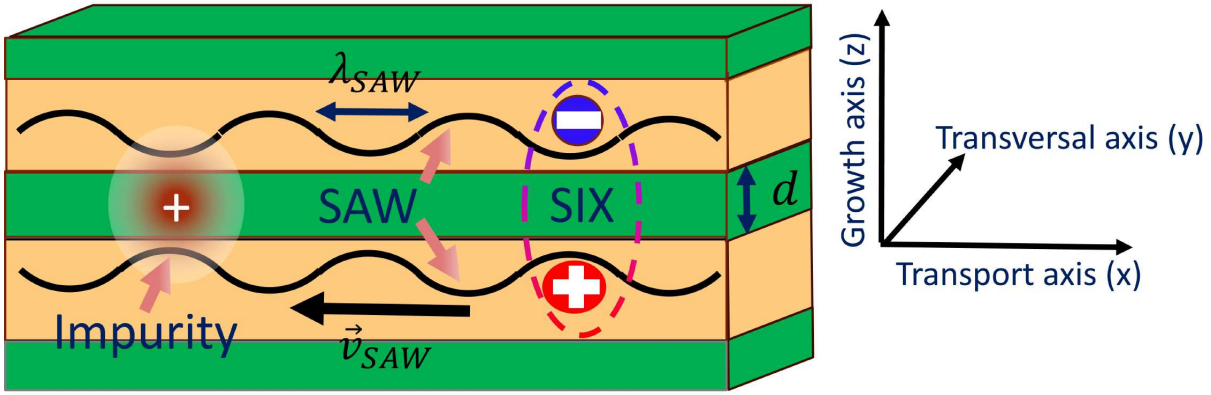

Figure 1.5: Schematic illustration of a coupled quantum well (CQW) driven by a surface acoustic wave (SAW). An electron and a hole reside in adjacent wells separated by a distance d, forming a spatially indirect exciton (SIX) with an intrinsic dipole moment. The propagating SAW, characterized by wavelength λ_{SAW} and group velocity $\vec{v}_{SAW}$, generates a moving potential that transports the SIX along the CQW plane. A localized impurity potential is shown schematically to illustrate the presence of a single scattering center in realistic devices.

Experimental and theoretical studies further indicate that SIX transport in realistic CQW devices is sensitive to local perturbations, such as electrostatic disorder, shallow traps, or defect-induced potentials. [132, 134] These observations highlight that excitonic control in CQWs emerges from the interplay between engineered driving fields and unavoidable disorder, motivating a detailed theoretical description of SIX dynamics under realistic operating conditions.

Across these nanostructures, this thesis focuses on two complementary regimes in which excitonic phenomena play a central role: static hybridization in M-NP systems (including CPh-QD and PhS-QD nanohybrids), where molecular and quantum-dot excitations mix to form hybrid states, and dynamic transport in CQWs, where SAWs drive the propagation of SIXs across potentials. The following section outlines the theoretical and computational perspective relevant to modeling excitations within this landscape.

1.3 Modeling excitons in hybrid and semiconductor nanostructures: from static hybridization to correlated transport

A first source of difficulty in modeling hybrid nanostructures arises from the mismatch of length and energy scales across molecular and semiconductor subsystems. Molecular excitations require atomistic, *ab initio* approaches capable of capturing strong electron correlation. [135] For CPhs or PhSs of order ~ 1 nm, Kohn–Sham Density Functional Theory (KS-DFT) provides a tractable description of ground-state electronic structure, while linear-response time-dependent DFT (LR-TDDFT) efficiently captures low-lying excited states at a moderate computational cost. [75] These methods are therefore well suited for treating localized molecular excitations.

By contrast, QDs contain hundreds to thousands of atoms, making atomistic *ab initio* descriptions impractical or prohibitive. Their excitations are more efficiently modeled using envelope-function approximations combined with Configuration Interaction (CI). [136,137] Reconciling these distinct electronic-structure descriptions within a single Hamiltonian is nontrivial, as it requires treating localized (molecular) and delocalized (semiconductor) excitations on the same footing.

Excitonic properties in nanohybrids also depend sensitively on structural and environmental factors. Molecular orientation, intermolecular spacing, QD size and composition, and dielectric screening all modulate excitonic couplings. [12,18,19] In photoswitches, torsional and dihedral motions along the photoisomerization coordinates can lead to substantial variations in state character and charge-transfer contributions. [76] A realistic modeling strategy must therefore remain robust across a broad range of geometries and excited-state landscapes.

These considerations motivate the use of multiscale, correlation-aware frameworks that merge fragment-specific excited-state descriptions. The Hybrid Configuration Interaction (HyCI) method, originally introduced in Ref. 12, provides a non-perturbative strategy for M-NP nanohybrids. In HyCI, each fragment -such as a chromophore (CPh), photoswitch (PhS), or quantum dot (QD)- is first described using the electronic-structure method best suited to its nature (such as DFT/TDDFT for molecules and single-exciton CI for QDs). The resulting fragment excited states are then combined to form a tensor-product basis, within which inter-fragment Coulomb interactions are evaluated explicitly. This construction yields a formally complete hybrid Hamiltonian that captures the correlated mixing of localized molecular excitations and delocalized nanoparticle excitons on equal footing.

In its original and subsequent applications, the HyCI framework was primarily employed in regimes where the quantities of interest were energy-transfer observables. Accordingly, those studies focused on inter-fragment transition rates, without explicitly constructing, diagonalizing, or analyzing the full hybrid Hamiltonian and its correlated eigenstates. Within this rate-based context, HyCI enabled a detailed and predictive description of resonance energy transfer beyond standard Förster theory, capturing effects arising from the finite size, crystalline symmetry, and multipolar response of the inorganic fragment, as well as orientation-dependent photoluminescence signatures in dye-functionalized QDs. [12,18,19]

In the present work, HyCI is applied *at its full theoretical scope for the first time*, through the explicit construction and diagonalization of the complete hybrid Hamiltonian in the tensor-product basis. While this level of description is formally contained within the original HyCI

methodology, it had not previously been carried out in practice. The full diagonalization enables a direct characterization of the energetics and eigenstates of correlated hybrid excitons, as well as their tunability with respect to material parameters and geometrical factors, particularly under resonant conditions. Within this fully diagonalized HyCI framework, we analyze hybrid excitations in CPh-QD assemblies and, as discussed above, provide also the *first cavity-free, exciton-driven description* of photoisomerization control in PhS-QD nanohybrids.

As an additional methodological advance, this work activates interaction channels that are formally allowed within the HyCI framework but had not been explored in previous applications: intraband transitions within the QD and excited-excited molecular transitions. The inclusion of these channels enables a more complete and internally consistent treatment of multistate excitonic coupling and higher-order hybridization effects in M-NP nanohybrids. From a computational perspective, this thesis also develops a scalable HyCI implementation, enabling efficient Hamiltonian construction and diagonalization and facilitating systematic, large-scale investigations of hybrid nanostructures.

While the discussion above focuses on hybrid nanostructures, correlated excitonic descriptions are also required in purely semiconductor platforms. In CQWs, SAW-SIXs evolve in a regime where center-of-mass motion and internal electron–hole dynamics are intrinsically coupled, rendering rigid or mean-field exciton approximations generally inadequate. Previous theoretical studies in Ref. 131,138,139 have shown that internal correlations can strongly affect transport, scattering, and tunneling processes, even in the absence of explicit disorder. These effects are further amplified by external perturbations such as shallow traps, gate-induced confinement, or time-dependent potentials. [132, 140]

Despite this insights, the specific role of localized ionic impurities (such as point charges embedded within or near the CQW) has not been systematically addressed within a fully correlated, time-dependent transport framework. In particular, existing models do not capture the combined influence of a moving SAW potential, internal electron–hole dynamics, and a screened impurity potential within a unified description. This thesis *addresses this gap* by explicitly incorporating a Debye-like screened impurity potential into a two-body correlated transport model, solved using the Fourier split-step (FSS) method developed in earlier works. [131, 132] This approach enables a direct investigation of how localized impurities modify the correlated real-space dynamics of SAW-SIXs, extending beyond previous scattering- or trap-based descriptions and providing a more complete picture of realistic environments in excitonic transport.

It is worth mentioning that additional complications in hybrid and semiconductor nanostructures arise in regimes where nuclear dynamics play an essential role, such as near conical intersections in PhSs or when phonon coupling reshapes excitonic structure. [141] Capturing nonadiabatic and phononic effects generally requires computational methods beyond the scope of this thesis. [142, 143, 144] The present work therefore focuses on electronic excitations in regions where conical intersections are not dominant and assumes that phonon-mediated relaxation occurs on timescales slower than the primary excitonic processes under study.

1.4 Scope, research questions, objectives, and outline of the thesis

From the state of the art discussed above, the overarching goal of this thesis is to understand how electron-hole correlations and excitonic couplings reshape hybridization, photochemical pathways, and transport in three representative platforms: (i) CPh-QD nanohybrids, (ii) PhS-QD nanohybrids, and (iii) CQWs supporting SAW-SIXs.

To reach this goal, the thesis is structured around the following research questions (RQs):

- **RQ1:** Can excitonic hybridization in M–NP systems be accurately captured using the multiscale, non-perturbative framework of HyCI, and how do geometric and material parameters influence the system behavior at resonance conditions?
- **RQ2:** Can intrinsic excitonic coupling in cavity-free PhS-QD nanohybrids be harnessed to modulate the photoisomerization pathways of PhSs, and how do geometric and materials parameters control this modulation?
- **RQ3:** How do localized ionic impurities and electron–hole correlations influence the transport of SAW-SIXs in CQWs, and under which conditions do correlation-driven regimes emerge beyond mean-field expectations?

Addressing these questions requires a set of objectives, each corresponding to one of the three platforms considered:

- **O1 (RQ1):** Apply the HyCI framework at its full theoretical scope for a prototypical $H_2P - GaN$ nanohybrid; and analyze how energy splittings and couplings change with system parameters and geometrical factors, particularly at resonance, together with addressing numerical accuracy.
- **O2 (RQ2):** Investigate exciton-driven photoisomerization in an AZB-CdSe nanohybrid and quantify the tunability of hybrid splittings and transition dipoles with QD size, molecular orientation, and intermolecular separation.
- **O3 (RQ3):** Apply a correlated two-body description to SIXs in SAW-driven CQWs with localized screened impurities, identify correlation-driven transport regimes, and contrast the results with simpler mean-field descriptions.

The thesis is organized so as to reflect the multiscale and interdisciplinary nature of the subject, illustrating how excitonic correlations shape optical, reactive, and transport processes across hybrid and semiconductor nanostructures. As a consequence, the thesis is structured as follows:

- **Chapter 1** introduces the physical context and motivation of the thesis, reviews relevant hybrid and semiconductor nanostructures, and outlines the scope, research questions, objectives and structure of the work.

- **Chapter 2** introduces the excitonic methods and numerical workflow used throughout this thesis. It includes DFT/LR-TDDFT for Ms, envelope-function and single-exciton CI models for QDs, and the HyCI framework for hybrid M-NP excitations and observables. It also presents the two-body correlated model for SAW-SIX transport in CQWs.

- **Chapter 3** applies HyCI to H_2P-GaN nanohybrids. It explores hybridization patterns and tunability with material and geometrical factors, together with interaction-driven scaling laws of energy splittings. The convergence of the HyCI results is assessed by varying the basis set and the truncation order of the multipolar expansion.

- **Chapter 4** applies HyCI to a AZB-CdSe nanohybrid. It investigates exciton-driven reshaping of photoisomerization pathways in a cavity-free setting, including a detailed analysis of hybrid PESs, its tunability with material and geometrical factors, and hybrid transition dipoles. A physical interpretation of these effects is provided in terms of coupled excitonic and charge delocalization across the molecular and QD fragments induced by near-resonant hybridization.

- **Chapter 5** presents a correlated transport study of SIXs in SAW-driven CQWs of GaAs/AlGaAs with localized impurities, emphasizing the role of electron-hole correlation and impurity screening in determining transport regimes and stability.

- **Chapter 6** summarizes the main findings, discusses broader implications for excitonic hybrid and semiconductor nanostructures, and outlines possible future research directions.

The thesis is accompanied by a set of appendices that provide additional technical details that complement the main text.

Chapter 2

Theoretical and computational methodology

A central topic of this thesis is the role of electron–hole correlations in shaping excitonic behavior across different classes of nanostructures. As introduced in Chapter 1, excitons provide a common framework for describing neutral electronic excitations in molecular, nanocrystal, and semiconductor platforms, despite the wide disparity in length scales, material composition, and physical mechanisms involved. Within this framework, correlated excitonic descriptions are shown to be essential both for static hybridization phenomena in M-NP systems and for dynamical processes in CQWs.

This chapter outlines the theoretical concepts and computational tools employed throughout this thesis to describe excitonic states and dynamics in both hybrid and purely semiconductor nanostructures. While different physical platforms are considered, all approaches presented here rely on electron–hole correlations beyond mean-field descriptions.

A first methodological pillar of the chapter is the HyCI framework, originally developed in Refs. 12, 18, 19. HyCI provides a unified, non-perturbative, multiscale description of electronic excitations in interacting M–NP nanohybrids and constitutes the theoretical backbone for the CPh–QD and PhS–QD systems analyzed in Chapters 3 and 4. Within this approach, localized molecular excitations and delocalized semiconductor excitons are treated on equal footing through the explicit construction and diagonalization of a hybrid Hamiltonian.

The general HyCI scheme for hybrid excitations proceeds in two steps. First, the molecular and nanoparticle fragments are treated independently to obtain their many-body electronic ground and excited states using electronic-structure methods suited to each subsystem. Second, the electronic excitations of the full hybrid system are obtained by constructing and diagonalizing the total HyCI Hamiltonian. This strategy exploits the natural separation of length, energy, and correlation scales characteristic of hybrid systems, while retaining an explicit description of inter-fragment Coulomb coupling.

A second methodological milestone addressed in this chapter concerns the correlated transport of SIXs in CQWs driven by SAWs. In this purely semiconductor platform, excitons form extended electron–hole pairs whose internal dynamics and center-of-mass motion are intrinsically coupled. When subject to time-dependent SAW potentials and localized scattering centers, rigid-exciton or mean-field descriptions become inadequate, requiring a fully correlated, two-body treatment.

To this end, the chapter presents a real-space, time-dependent description of SIX dynamics based on the explicit propagation of the electron–hole wave function, following the correlated two-body framework originally developed in Refs.131,132. The resulting two-body Schrödinger equation is solved numerically using a Fourier split-step (FSS) scheme, providing the methodological foundation for the transport studies presented in Chapter 5.

The chapter is organized as follows. Section 2.1 introduces the theoretical and numerical framework used to describe hybrid excitations in M–NP nanohybrids, including the fragment-level electronic structure and the HyCI approach. Section 2.2 presents the theoretical and numerical framework for modeling the correlated transport of SAW-diven SIXs in CQWs. All equations in Section 2.1 are expressed in atomic units, whereas those in Section 2.2 are formulated in SI units. Finally, Section 2.3 connects the methodological developments to the case studies presented in the following chapters.

2.1 Hybrid excitons in molecule-nanoparticle systems

2.1.1 Molecular excitations

The molecular (M) fragments considered in this thesis are chromophores (CPhs) such as porphine (H_2P) and photoswitches (PhSs) such as azobenzene (AZB). Their electronic structure is dominated by localized $\pi \rightarrow \pi^*$ and $n \rightarrow \pi^*$ valence excitations. [145] In weak-field, linear optical regime, these low-lying excited states and the associated transition properties can be accurately described using standard Kohn-Sham Density Functional Theory (KS-DFT) for the ground state [146, 147] and linear-response time-dependent DFT (LR-TDDFT) in Casida formalism. [148, 149]

The key theoretical ingredients for the ground state within KS-DFT are summarized in the following subsection, while subsection 2.1.1.2 addresses the computation of molecular excitation energies and approximate excited states within LR-TDDFT. These quantities constitute key inputs to the HyCI method discussed in Section 2.1.3. In close analogy with the present section, the excitations of the NP fragment are described in Section 2.1.2.

2.1.1.1 Ground-state: Kohn-Sham DFT

A common underlying assumption in the description of molecular electronic structure is the *Born-Oppenheimer (BO) approximation*, which exploits the large mass difference between nuclei and electrons to separate their dynamics. Within this approximation, electronic states are defined for fixed nuclear geometries, allowing electronic excitations to be treated independently of nuclear motion. This separation constitutes a standard starting point for essentially all ground- and excited-state electronic-structure methods, [147] including those employed in this work for nanoparticles, and hybrid systems (Sections 2.1.2 and 2.1.3). As a consequence, nuclear degrees of freedom enter the present treatment only indirectly, through optimized equilibrium geometries.

Within this BO approximation, Density Functional Theory (DFT) provides a formally exact framework for ground-state electronic structure, in which all observables are functionals of the ground-state electron density $\rho_0(\mathbf{r})$. In practice, its most widely used realization is the Kohn-Sham (KS) formulation, which introduces an auxiliary system of non-interacting particles

constructed to reproduce the exact ground-state density. [147] This formulation underlies most contemporary quantum-chemistry software packages and forms the basis of the ground-state molecular calculations employed in this work.

Within KS-DFT, the ground-state electronic structure of a molecular fragment is described by a set of single-particle (SP) orbitals $\{\phi_k(\mathbf{r})\}$ satisfying the KS equations

$$\left[-\frac{1}{2}\nabla^2 + v_{\text{ext}}(\mathbf{r}) + v_{\text{H}}(\mathbf{r}) + v_{\text{xc}}(\mathbf{r})\right]\phi_k(\mathbf{r}) = \epsilon_k\,\phi_k(\mathbf{r}), \tag{2.1}$$

where $\{\epsilon_k\}$ are the KS energies.

The effective potential in Eq. (2.1) consists of three contributions. The external potential acting on the electrons is given explicitly by $v_{\text{ext}}(\mathbf{r}) = -\sum_A Z_A/|\mathbf{r}-\mathbf{R}_A|$, which represents the Coulomb attraction between electrons and nuclei at positions $\mathbf{R}_A$. The Hartree potential

$$v_{\text{H}}(\mathbf{r}) = \int \frac{\rho_0(\mathbf{r}')}{|\mathbf{r}-\mathbf{r}'|}\,d\mathbf{r}' \tag{2.2}$$

accounts for the classical electrostatic electron-electron interaction, while the exchange-correlation (xc) potential $v_{\text{xc}}(\mathbf{r})$ incorporates effectively the effects due to many-body and exchange interactions beyond the Hartree term.

These many-body effects are described through the exchange-correlation energy functional $E_{\text{xc}}[\rho]$, whose functional derivative with respect to the density defines the xc potential,

$$v_{\text{xc}}(\mathbf{r}) = \frac{\delta E_{\text{xc}}[\rho_0]}{\delta\rho_0(\mathbf{r})}. \tag{2.3}$$

The ground-state electron density is constructed from the KS orbitals as

$$\rho_0(\mathbf{r}) = \sum_k f_k\,|\phi_k(\mathbf{r})|^2, \tag{2.4}$$

where f_k are the orbital occupation numbers (equal to 1 for occupied orbitals and 0 for virtual, i.e., unoccupied, orbitals).

Because the effective potential in Eq. (2.1) depends explicitly on $\rho_0(\mathbf{r})$, the KS equations and the density definition must be solved self-consistently. Once convergence is achieved, the total ground-state energy of the molecular fragment is obtained as

$$E_0^{\text{M}} = T_s[\{\phi_k\}] + \int \rho_0(\mathbf{r})\left[v_{\text{ext}}(\mathbf{r}) + \frac{1}{2}v_{\text{H}}(\mathbf{r})\right]d\mathbf{r} + E_{\text{xc}}[\rho_0] + E_{\text{nn}}, \tag{2.5}$$

where $E_{\text{nn}} = \frac{1}{2}\sum_{A\neq B} Z_A Z_B/|\mathbf{R}_A - \mathbf{R}_B|$ is the nuclear–nuclear repulsion energy. The non-interacting kinetic energy is evaluated explicitly from the KS orbitals as

$$T_s[\{\phi_k\}] = -\frac{1}{2}\sum_k f_k \int \phi_k^*(\mathbf{r})\,\nabla^2\,\phi_k(\mathbf{r})\,d\mathbf{r}. \tag{2.6}$$

The practical realization of the Kohn-Sham framework requires specifying an approximation for the exchange-correlation functional $E_{\text{xc}}[\rho]$ and a representation of the KS orbitals $\{\phi_k(\mathbf{r})\}$.

In this work, the ground-state electronic structure of molecular fragments is described using hybrid and range-separated hybrid exchange-correlation approximations, specifically B3LYP and CAM-B3LYP. By incorporating a fraction of exact Hartree-Fock exchange, these functionals provide an improved treatment of self-interaction effects and nonlocal exchange, which is essential for molecules exhibiting significant charge delocalization. [147]

The KS orbitals are expanded in atom-centered Gaussian-type basis sets. In particular, the aug-cc-pVDZ and def2-pVTZ basis sets are employed, defining the spatial resolution of the electronic degrees of freedom. These basis sets provide a balanced description of valence, polarization, and diffuse character, ensuring numerical stability and sufficient accuracy for the ground-state properties. [146]

The molecular ground-state density $\rho_0(\mathbf{r})$ and energy E_0^{M} constitute the relevant ground-state input for subsequent excited-state calculations. In addition, the occupied KS orbitals define a single Slater-determinant reference state $|M_0\rangle$, which is used as the molecular ground-state reference throughout this thesis.

2.1.1.2 Excited states: Linear-Response TDDFT

TDDFT provides a formally exact framework for describing the electronic dynamics and excitation spectrum of interacting many-electron systems in terms of the time-dependent electron density $\rho(\mathbf{r}, t)$. In the weak-field regime relevant for optical spectroscopy, vertical neutral excitations can be accessed within the linear-response formulation of TDDFT (LR-TDDFT), where excitation frequencies correspond to the poles of the density-density response function $\chi(\mathbf{r}, \mathbf{r}'; \omega)$. [149]

Building on the KS energies $\{\epsilon_k\}$ and orbitals $\{\phi_k(\mathbf{r})\}$ introduced in the previous subsection, the linear density response can be expanded in a basis of KS electron-hole (exciton) configurations. This leads to the Casida formalism of LR-TDDFT, which provides a convenient pseudo-eigenvalue representation for optical excitations. [148, 149, 150]

In practical applications and in most available computational codes, LR-TDDFT calculations are performed within the *adiabatic approximation*, in which the exchange-correlation (xc) kernel is assumed to be frequency independent and equal to its static (zero-frequency) limit. [149] Under this assumption, the Casida equations reduce to a linear pseudo-eigenvalue problem, which can be written in compact matrix form as [148, 150]

$$\begin{pmatrix} \mathbf{A} & \mathbf{B} \\ \mathbf{B}^* & \mathbf{A}^* \end{pmatrix} \begin{pmatrix} \mathbf{X}^\alpha \\ \mathbf{Y}^\alpha \end{pmatrix} = \omega_\alpha \begin{pmatrix} \mathbf{I} & \mathbf{0} \\ \mathbf{0} & -\mathbf{I} \end{pmatrix} \begin{pmatrix} \mathbf{X}^\alpha \\ \mathbf{Y}^\alpha \end{pmatrix}, \tag{2.7}$$

where positive (negative) ω_α corresponds to excitation (de-excitation) frequencies, $\mathbf{X}^\alpha$ and $\mathbf{Y}^\alpha$ are the associated excitation and de-excitation amplitudes, and $\mathbf{I}$ is the identity matrix.

The orbital-rotation Hessians $\mathbf{A}$ and $\mathbf{B}$ are defined element-wise as

$$A_{fu,gv} = (\epsilon_u - \epsilon_f)\,\delta_{fg}\delta_{uv} + K_{fu,gv}, \tag{2.8}$$

$$B_{fu,gv} = K_{fu,vg}, \tag{2.9}$$

where ϵ_f and ϵ_u are KS energies, occupied orbitals are labeled by f, g and virtual orbitals by u, v, such that each composite index (f, u) represents an electron-hole excitation from f to u. The effective electron-hole interaction matrix reads

$$K_{fu,gv} = \iint \phi_f^*(\mathbf{r})\phi_u(\mathbf{r}) \left[\frac{1}{|\mathbf{r} - \mathbf{r}'|} + f_{\mathrm{xc}}^{\mathrm{A}}(\mathbf{r}, \mathbf{r}')\right] \phi_g(\mathbf{r}')\phi_v^*(\mathbf{r}')\, d\mathbf{r}\, d\mathbf{r}', \tag{2.10}$$

where the adiabatic xc kernel is given by

$$f_{\mathrm{xc}}^{\mathrm{A}}(\mathbf{r},\mathbf{r}') = \frac{\delta v_{\mathrm{xc}}(\mathbf{r})}{\delta\rho_0(\mathbf{r}')} = \frac{\delta^2 E_{\mathrm{xc}}[\rho_0]}{\delta\rho_0(\mathbf{r})\,\delta\rho_0(\mathbf{r}')}. \tag{2.11}$$

It is worth noting that the general Casida formulation is, in principle, non-linear because the exact xc kernel depends explicitly on the frequency,

$$f_{\mathrm{xc}}(\mathbf{r},\mathbf{r}';\omega) = \int_{-\infty}^{\infty} d(t-t')\, e^{i\omega(t-t')}\, \frac{\delta v_{\mathrm{xc}}[\rho(\mathbf{r},t)]}{\delta\rho(\mathbf{r}',t')}\bigg|_{\rho=\rho_0(\mathbf{r})}, \tag{2.12}$$

reflecting the non-locality of the time-dependent xc potential. [149] The adiabatic approximation not only eliminates explicit memory effects but it also restricts the excitation manifold. The absence of frequency dependence in f_{xc} prevents the correct description of genuine double and higher-order excitations, which require a dynamical kernel to generate additional poles in $\chi(\mathbf{r},\mathbf{r}';\omega)$ beyond those associated with single KS electron-hole configurations. [149]

Despite of its limitations, the adiabatic approximation is computationally efficient and often accurate for low-lying valence excitations. [148, 149] Besides, the explicit frequency dependence of the kernel is unknown for most systems or very difficult to evaluate, [148] motivating even more the widespread adoption of the adiabatic approximation.

Within the adiabatic approximation, the vertical excitation energy of the α-th excited state is obtained as

$$E_\alpha^{\mathrm{M}} = E_0^{\mathrm{M}} + \omega_\alpha, \tag{2.13}$$

where E_0^{M} is the KS ground-state energy from Eq.(2.5).

Following Ref. 151, excited states can be approximately represented in a CI-like form as

$$|M_\alpha\rangle \approx \sum_f^{\mathrm{occ}} \sum_u^{\mathrm{vir}} (X_{fu}^\alpha + Y_{fu}^\alpha)\, |\Phi_f^u\rangle\,, \qquad |\Phi_f^u\rangle = \hat{a}_u^\dagger \hat{a}_f\, |M_0\rangle\,, \tag{2.14}$$

where $|M_0\rangle$ denotes the KS ground state and $|\Phi_f^u\rangle$ is a singly-excited Slater determinant obtained by promoting one electron from an occupied KS orbital f to a virtual orbital u. The operators $\hat{a}_u^\dagger$ ($\hat{a}_f$) are the corresponding fermionic creation (annihilation) operators. The Casida excitation (X_{fu}^α) and de-excitation (Y_{fu}^α) amplitudes are obtained from Eq.(2.7).

We emphasize that this representation, commonly adopted in the literature, provides only a practical but approximate CI-like description of the exact many-body excited-state wavefunction. In particular, orbital relaxation effects specific to individual excited states are not explicitly included within LR-TDDFT, independently of the approximation adopted for the xc kernel. [149] This is due to the fact that excited states are constructed as linear density fluctuations around the ground-state reference $|M_0\rangle$ and are therefore described entirely in terms of ground-state KS orbitals.

As in the ground-state case, the accuracy of LR-TDDFT excitation energies and transition properties depends on the exchange-correlation approximation entering the adiabatic kernel. In this thesis, hybrid and range-separated hybrid functionals (B3LYP and CAM-B3LYP) are employed, as the inclusion of exact exchange improves the description of electron-hole interactions and mitigates self-interaction effects in molecular excitations. [149]

The representation of the underlying KS orbitals further defines the level of approximation of the excited-state model. Here, the aug-cc-pVDZ and def2-pVTZ basis sets are adopted, providing sufficient polarization and diffuse character to reliably describe excitation energies and transition dipole moments relevant to the systems considered. [146]

The excited-state energies E_α^{M} and excited molecular state $|M_\alpha\rangle$, together with their ground-state counterparts E_0^{M} and $|M_0\rangle$ introduced in the previous subsection, constitute key inputs for the HyCI method discussed in Section 2.1.3. Before addressing hybrid excitations, however, the analogous quantities for the NP fragment must be introduced, which is the focus of the next section.

2.1.2 Nanoparticle excitations

The inorganic nanoparticles (NPs) considered in this thesis are spherical quantum dots (QDs) composed of semiconductor materials with wurtzite crystal structure, such as CdSe or GaN. Their electronic excitations originate from discrete electron and hole states derived from the bulk band structure and modified by quantum confinement and dielectric effects. [152] For the nanoparticle sizes and materials considered here, the single-particle electron and hole states are accurately described within the envelope-function approximation (EFA). [153, 154] In the weak-excitation, linear-response regime, neutral excited states are well described using a Full Configuration Interaction (Full-CI) approach within the single-exciton manifold. [154]

In analogy with the molecular excitations discussed in Section 2.1.1, this section summarizes the theoretical framework used to compute the energies and electronic states of the NP subsystem. First, we introduce the single-particle (SP) states in Section 2.1.2.1. Then, the multiparticle (MP) excitations within the single-exciton manifold are described at the level of Full-CI in Section 2.1.2. The corresponding energies and states constitute essential inputs for the HyCI method introduced in Section 2.1.3.

2.1.2.1 Single-particle states: envelope-function approximation

The electronic structure of the nanoparticle fragment is described at the SP level using the EFA, which provides an effective and accurate framework to model quantum-confined carriers in semiconductor quantum dots when the QD radius R_{QD} is much larger than the characteristic length scale of the underlying lattice structure. [153, 154] Within this approach, the fast oscillations associated with the crystal lattice are separated from the slowly varying spatial dependence induced by confinement, allowing the electronic states to be expressed in terms of effective-mass envelope functions.

We follow Ref. [12,18,19] in the one-band effective-mass EFA adopted here for quasi-particle electrons (e) and heavy holes (h). The corresponding wavefunctions are written as

$$\psi_i^{(e)}(\mathbf{r}) = f_i^{(e)}(\mathbf{r})\, u_c(\mathbf{r}), \qquad \psi_p^{(h)}(\mathbf{r}) = f_p^{(h)}(\mathbf{r})\, u_v(\mathbf{r}), \tag{2.15}$$

where $u_c(\mathbf{r})$ and $u_v(\mathbf{r})$ are the Bloch functions associated with the conduction and valence band edges at the Γ point, respectively, and the set $\{f_i^{(e)}(\mathbf{r})\}$ ($\{f_p^{(h)}(\mathbf{r})\}$) are the slowly varying envelopes of electrons (holes). This envelope functions satisfy the Schrödinger-like equations

$$\left[-\frac{1}{2m_{e,h}^*}\nabla^2 + V_{\mathrm{eff}}(x)\right] f_{i,p}^{(e,h)}(\mathbf{r}) = E_{i,p}^{(e,h)}\, f_{i,p}^{(e,h)}(\mathbf{r}), \tag{2.16}$$

where $m^*_{e,h}$ are the electron and heavy-hole effective masses, $E_i^{(e)}$ and $E_p^{(h)}$ are the corresponding SP energies and $x = r/R_{\mathrm{QD}}$ denotes the radial coordinate scaled by the QD radius.

The effective potential is given by

$$V_{\mathrm{eff}}(x) = \begin{cases} \left(\dfrac{\varepsilon - 1}{2\varepsilon_{\mathrm{QD}} R_{\mathrm{QD}}}\right) \displaystyle\sum_{k=0}^{\infty} \frac{k+1}{1 + k(\varepsilon+1)}\, x^{2k}, & x < 1 \\ \infty, & x > 1 \end{cases} \tag{2.17}$$

where $\varepsilon = \varepsilon_{\mathrm{QD}}/\varepsilon_{\mathrm{out}}$ is the ratio between the dielectric constant of the nanoparticle material and that of the surrounding medium. This effective potential accounts for both hard-wall confinement and polarization effects arising from dielectric mismatch at the nanoparticle surface. [155]

Because the Hamiltonian in Eq. (2.16) is spherically symmetric, the envelope functions can be chosen as simultaneous eigenfunctions of angular momentum. They therefore separate into radial and angular components according to

$$f^{(e,h)}(\mathbf{r}) = R_{nl}^{(e,h)}(r)\, Y_{lm}(\Omega), \tag{2.18}$$

where $Y_{lm}(\Omega)$ are spherical harmonics with $\Omega = (\theta, \phi)$ as angular coordinates and (n, l, m) are the principal, orbital, and magnetic quantum numbers, respectively. This symmetry greatly simplifies the computation of many envelope-function integrals throughout this work.

The SP energies $E_{i,p}^{(e,h)}$ and states $\psi_{i,p}^{(e,h)}$ introduced in this subsection form the basis for the subsequent excited-state computation.

2.1.2.2 Multiparticle states: Full-CI expansion

In general, excited states in NPs arise from Coulomb-coupled electron-hole configurations and may involve one or more electron-hole pairs, depending on the excitation conditions and the level of theory employed. In the quantum-confined regime relevant to this work and under weak-excitation conditions, the optical response is dominated by single electron-hole pairs (excitons). Consequently, excitonic states can be accurately described by a full configuration-interaction (Full-CI) treatment restricted to the single-exciton manifold, neglecting higher-order excitations such as biexcitons. [154]

We follow Refs. [137, 156, 157, 158, 159] for the specific single-exciton Full-CI framework adopted here. Starting from the SP electron and hole eigenstates $\{|i\rangle \equiv \psi_i^{(e)}\}$ and $\{|p\rangle \equiv \psi_p^{(h)}\}$, a basis of electron-hole product states is defined as $|ip\rangle = |i\rangle \otimes |p\rangle$, where each configuration corresponds to an electron occupying a conduction-band state i and a hole occupying a valence-band state p.

The nanoparticle excitonic eigenstates are expanded in this basis as

$$|\mathrm{NP}_\nu\rangle = \sum_{i,p} c_{ip}^{\nu}\, |ip\rangle\,, \tag{2.19}$$

where the CI coefficients c_{ip}^{ν} quantify the contribution of each electron-hole configuration to the ν-th excitonic state. The coefficients are eigenvectors obtained by fully diagonalizing the excitonic Hamiltonian in the $\{|ip\rangle\}$ basis,

$$\langle ip|\, \hat{H}_{\mathrm{exc}}\, |jq\rangle = \left(E_i^{(e)} + E_p^{(h)}\right) \delta_{ij}\delta_{pq} - \langle ip|\, \hat{V}_{\mathrm{ren}}(\mathbf{x}_e, \mathbf{x}_h)\, |jq\rangle\,, \tag{2.20}$$

where $E_i^{(e)}$ and $E_p^{(h)}$ are the SP energies obtained from Eq. (2.16), and $\mathbf{x}_e = \mathbf{r}_e/R_{QD}$ and $\mathbf{x}_h = \mathbf{r}_h/R_{QD}$ are the dimensionless electron and hole position vectors. The interaction operator $\hat{V}_{\text{ren}}$ is a renormalized Coulomb potential that includes dielectric mismatch effects at the nanoparticle surface. For a spherical NP, $\hat{V}_{\text{ren}}$ can be expressed as [155]

$$\hat{V}_{\text{ren}}(\mathbf{x}_e, \mathbf{x}_h) = \left(\frac{1}{\varepsilon_{\text{QD}} R_{\text{QD}}}\right) \sum_{\ell=0}^{\infty} \left[\frac{x_<^{\ell}}{x_>^{\ell+1}} + \frac{(\ell+1)(\varepsilon-1)}{1+\ell(\varepsilon+1)}(x_e x_h)^{\ell}\right] P_\ell(\cos\Theta_{eh}), \tag{2.21}$$

where $x_< = \min\{x_e, x_h\}$ and $x_> = \max\{x_e, x_h\}$, P_ℓ is the Legendre polynomial of order ℓ, and Θ_{eh} is the angle between the electron and hole position vectors.

In practice, the corresponding two-particle matrix elements are evaluated by retaining the dominant envelope-function contributions (see Appendix A.1). Although the renormalized interaction includes additional contributions arising from surface polarization, its angular dependence is identical to that of the bare Coulomb potential. As a result, the interaction preserves full spherical symmetry and obeys the same angular momentum and parity selection rules, which render finite the ℓ-summation in the matrix elements of Eq. (2.21) (see Appendix A.1.1). Dielectric effects enter only through modifications of the radial coupling strengths.

Diagonalization of Eq. (2.20) yields the correlated excitonic shifts $\{E_\nu^{\text{exc}}\}$, measured relative to the conduction- and valence-band edges. The absolute energy of the ν-excited state is obtained by simply adding the bulk band gap $E_{\text{gap}}^{\text{bulk}}$ of the NP material,

$$E_\nu^{\text{NP}} = E_{\text{gap}}^{\text{bulk}} + E_\nu^{\text{exc}}. \tag{2.22}$$

In this work, the nanoparticle ground state $|\text{NP}_0\rangle$ (corresponding to the vacuum configuration with no electron-hole pairs) is always taken as the reference for energies, both in the isolated NP and the hybrid M-NP system. Its value is therefore set to zero ($E_0^{\text{NP}} = 0$).

In materials with a wurtzite crystal structure, such as CdSe or GaN, the heavy-hole band edge exhibits a twofold degeneracy associated with distinct spin–orbit–coupled Bloch functions. [18] Optical interband excitation creates a spin-singlet (total spin zero) exciton formed by a conduction-band electron and a heavy hole, where the twofold degeneracy of the hole band gives rise to two distinct but degenerate excitonic states with identical envelope functions. In this work, such twofold degeneracy is relevant only for *interband* transitions in the quantum dot. Accordingly, both excitonic states are denoted hereafter as $|\text{NP}_\nu\rangle$ unless the explicit spin-index distinction (+ or −) is required.

Together with their molecular counterparts, the excited-state energies E_ν^{NP} and excitonic states $|\text{NP}_\nu\rangle$ of the NP constitute essential inputs for the HyCI method discussed in the following section.

2.1.3 Hybrid molecule-nanoparticle excitations

The M-NP nanohybrids, such as the CPh-QD and PhS-QD systems studied in this thesis, span a wide range of length and energy scales. Localized molecular excitations coexist and interact with delocalized semiconductor excitons, whose spatial extent and energy spectrum are governed by quantum confinement. Depending on the relative energies, symmetries, and coupling strength, the resulting excited states may retain a predominantly M or NP character, or acquire a genuinely hybrid nature through excitonic mixing.

The Hybrid Configuration Interaction (HyCI) method, originally introduced in Refs. 12, 18, 19, describes electronic excitations in M-NP nanohybrids by diagonalizing an explicit inter-fragment interaction Hamiltonian in a tensor-product basis of fragment excited states, thereby providing a multiscale and non-perturbative description of hybrid excitations.

In this section, we provide an overview of the key theoretical and computational ingredients of the HyCI method. We begin in the following subsection with the formulation of the general HyCI scheme and the corresponding Hamiltonian for the M-NP system. Subsection 2.1.3.2 then describes the dipole-field approximation adopted throughout this thesis for the evaluation of the M-NP interaction operator. Finally, Subsections 2.1.3.3, 2.1.3.4 and 2.1.3.5 present the theoretical framework used to compute molecular dipole moments, nanoparticle electric-field matrix elements, and hybrid dipoles based on the fragment-specific inputs introduced in Sections 2.1.1 and 2.1.2.

2.1.3.1 Hybrid states: the HyCI Hamiltonian

From a formal standpoint, the HyCI method only requires that the fragment MP excited states admit an expansion in a basis of non-interacting Slater determinants constructed from SP states. [12] In this work, such MP states are obtained for the molecular fragment in Section 2.1.1 using KS-DFT and LR-TDDFT, and for the nanoparticle fragment in Section 2.1.2 using EFA/Full-CI.

Ground and excited molecular many-body states are denoted by $\{|M_\alpha\rangle\}$ with energies $\{E^{\mathrm{M}}_\alpha\}$, where $\alpha = 0, 1, 2, \ldots$. The corresponding nanoparticle excitonic states are denoted by $\{|\mathrm{NP}_\nu\rangle\}$ with energies $\{E^{\mathrm{NP}}_\nu\}$, where $\nu = 0, 1, 2, \ldots$. Greek indices $\alpha, \beta, \ldots$ label molecular states, while $\nu, \mu, \ldots$ label nanoparticle states.

The non-interacting basis for the hybrid system is therefore defined as

$$|\alpha\nu\rangle \equiv |M_\alpha\rangle \otimes |\mathrm{NP}_\nu\rangle \,. \tag{2.23}$$

In this basis, the HyCI Hamiltonian reads [12]

$$H_{\alpha\nu,\beta\mu} = \left(E^{\mathrm{M}}_\alpha + E^{\mathrm{NP}}_\nu\right)\delta_{\alpha\beta}\delta_{\nu\mu} + \langle M_\alpha\,\mathrm{NP}_\nu|\,\hat{V}^{\mathrm{M-NP}}\,|M_\beta\,\mathrm{NP}_\mu\rangle\,, \tag{2.24}$$

where $\hat{V}^{\mathrm{M-NP}}$ is the molecule-nanoparticle interaction operator (explicitly defined in Section 2.1.3.2). Diagonalization of Eq. (2.24) yields the hybrid excitonic states

$$|\Psi_{\mathcal{I}}\rangle = \sum_{\alpha,\nu} C^{\mathcal{I}}_{\alpha\nu}\;|M_\alpha\rangle \otimes |\mathrm{NP}_\nu\rangle\,, \tag{2.25}$$

with energies $E_{\mathcal{I}}$. The HyCI coefficients $C^{\mathcal{I}}_{\alpha\nu}$ quantify the degree of hybridization between molecular and nanoparticle excitations and provide a natural measure of excitonic mixing.

One key ingredient in the HyCI Hamiltonian matrix is the form of the interaction operator, coupling molecular and nanoparticle states. An explicit and practical form of $\hat{V}^{\mathrm{M-NP}}$ depends on the relative geometry and separation of both subsystems. In the following subsection, we introduce the dipole-field approximation, which provides the leading contribution to the HyCI coupling considered throughout this work.

2.1.3.2 The M-NP interaction operator in dipole-field approximation

In principle, $\hat{V}^{\mathrm{M-NP}}$ originates from the Coulomb interaction between all charges of the two fragments. In the most general case, it may include finite overlap between molecular and nanoparticle electronic wavefunctions, giving rise to exchange and antisymmetrization effects between electrons belonging to different fragments. [12]

In this thesis, however, we enforce *negligible overlap* between molecular and nanoparticle electronic wavefunctions. This is appropriate when the separation $\mathbf{R}$ between the center-of-mass (CoM) of each fragment satisfies

$$|\mathbf{R}| \gtrsim R_{\mathrm{NP}} + R_{\mathrm{M}} + R^{\mathrm{H}}_{\mathrm{VdW}}. \tag{2.26}$$

Here, R_{NP} and R_{M} are the characteristic radii of the nanoparticle and molecule, respectively, and $R^{\mathrm{H}}_{\mathrm{VdW}}$ is the van der Waals length of hydrogen atoms from the organic molecule.

In this work, the NP CoM is always placed at the origin, while the molecular CoM is located at the center-to-center separation $\mathbf{R}$ satisfying Eq.(2.26). Under these conditions, the interaction operator can be expanded in multipoles of the molecular charge distribution interacting with the electric field generated by the nanoparticle. [12] The leading contribution of such expansion is given by the dipole-field term,

$$\hat{V}^{\mathrm{M-NP}}_{(leading)} = -\hat{\mathbf{d}}^{\mathrm{M}} \cdot \hat{\mathbf{E}}^{\mathrm{NP}}(\mathbf{R}), \tag{2.27}$$

where $\hat{\mathbf{d}}^{\mathrm{M}}$ is the dipole operator due to nuclear and electronic charges in the molecule, and $\hat{\mathbf{E}}^{\mathrm{NP}}(\mathbf{R})$ is the electric-field operator generated by the nanoparticle charges, evaluated at the molecule CoM in $\mathbf{R}$.

Throughout this thesis, we consider molecular fragments that are nearly three and a half times smaller than the corresponding nanoparticles. In such systems, the spatial extent of the molecular charge distribution is small compared to the characteristic length scale over which the nanoparticle electric field varies. This separation of length scales naturally leads to the *dipole-field approximation*, in which higher-order multipole contributions of the molecule are neglected. [12] Within this approximation, the interaction matrix elements in the HyCI basis read

$$\langle M_\alpha\, \mathrm{NP}_\nu |\, \hat{V}^{\mathrm{M-NP}}\, | M_\beta\, \mathrm{NP}_\mu \rangle = -\mathbf{d}^{\mathrm{M}}_{\alpha\beta} \cdot \mathbf{E}^{\mathrm{NP}}_{\nu\mu}(\mathbf{R}), \tag{2.28}$$

where $\mathbf{d}^{\mathrm{M}}_{\alpha\beta}$ are molecular dipole matrix elements between states $|M_\alpha\rangle$ and $|M_\beta\rangle$, and $\mathbf{E}^{\mathrm{NP}}_{\nu\mu}(\mathbf{R})$ are nanoparticle's electric-field matrix elements between excitonic states $|\mathrm{NP}_\nu\rangle$ and $|\mathrm{NP}_\mu\rangle$, evaluated at the molecular center-of-mass position $\mathbf{R}$. We emphasize that, while the molecular fragment is truncated at the dipole level, the nanoparticle electric field $\hat{\mathbf{E}}^{\mathrm{NP}}(\mathbf{R})$ fully accounts for the spatial structure of the nanoparticle charge distribution. As a result, all multipolar contributions of the nanoparticle are implicitly included in the interaction.

As a direct consequence of the dipole-field approximation, the construction of the interaction matrix in Eq. (2.24) is reduced to the evaluation of fragment-specific quantities, namely the M dipole matrix elements and the NP electric-field matrix elements. These quantities must therefore be computed explicitly using the fragment-level electronic-structure methods introduced in Sections 2.1.1 and 2.1.2.

We address their explicit evaluation in the following subsections. We begin with the M contribution, while the computation of NP electric-field matrix elements is discussed separately in subsection 2.1.3.4.

2.1.3.3 Molecular dipole moments

The molecular electric dipole operator can be written as the sum of electronic and nuclear contributions,

$$\hat{\mathbf{d}}^{\mathrm{M}} = \hat{\mathbf{d}}^{e} + \mathbf{d}^{N}(\{\mathbf{R}_A\}), \qquad \hat{\mathbf{d}}^{e} = -\sum_{n} \hat{\mathbf{r}}_n, \qquad \mathbf{d}^{N}(\{\mathbf{R}_A\}) = \sum_{A} Z_A \mathbf{R}_A, \tag{2.29}$$

where $\{\mathbf{R}_A\}$ denotes the set of fixed nuclear positions. Given the molecular electronic states $|M_\alpha\rangle$ and $|M_\beta\rangle$, the corresponding matrix elements read

$$\langle M_\alpha | \, \hat{\mathbf{d}}^{\mathrm{M}} \, | M_\beta \rangle = \langle M_\alpha | \, \hat{\mathbf{d}}^{e} \, | M_\beta \rangle + \delta_{\alpha\beta} \sum_{A} Z_A \mathbf{R}_A, \tag{2.30}$$

where the Kronecker delta follows from the fact that the nuclear contribution is a geometry-fixed c-number within the BO approximation, and therefore contributes only to diagonal matrix elements between orthonormal electronic states.

Ground-state dipole. In KS-DFT, the electronic contribution in Eq. (2.30) can be obtained directly as an observable of the electronic density, [147] leading to the ground-state dipole

$$\mathbf{d}^{\mathrm{M}}_{00} = -\int \mathbf{r}\, \rho_0(\mathbf{r})\, d\mathbf{r} + \sum_{A} Z_A \mathbf{R}_A. \tag{2.31}$$

Here ρ_0 is the ground-state density given by Eq. (2.4).

Ground-to-excited transition dipoles. As shown by Eq. (2.30), ground-to-excited transition dipoles $\mathbf{d}^{\mathrm{M}}_{0\alpha} = \langle M_0 | \, \hat{\mathbf{d}}^{e} \, | M_\alpha \rangle$ are purely electronic in origin. In LR-TDDFT, these electronic contributions are obtained as residues of the density-density response function $\chi(\mathbf{r}, \mathbf{r}'; \omega)$. [149] Within Casida formalism, this leads to a weighted sum of one-body dipole matrix elements between occupied and virtual KS orbitals, [148, 149]

$$\mathbf{d}^{\mathrm{M}}_{0\alpha} = \sum_{fu} \left(X^{\alpha}_{fu} + Y^{\alpha}_{fu} \right) \langle \phi_f | \hat{\mathbf{r}} | \phi_u \rangle, \tag{2.32}$$

where the amplitudes X^{α}_{fu} and Y^{α}_{fu} come from Eq. (2.7) and the KS orbitals are obtained from Eq.(2.1).

Excited-to-excited transition dipoles. Unlike ground-to-excited transition dipoles, excited-to-excited dipole moments are not direct outputs of standard LR-TDDFT, which is formulated as a response around the ground-state density $\rho_0(\mathbf{r})$. In this thesis, these quantities are evaluated using the CI-like approximate singles construction defined in Subsection 2.1.1.2 [see Eq. (2.14)] for molecular excited states.

Inserting this representation into Eq. (2.30) and applying Slater-Condon rules for a one-body operator, the resulting expression is [151, 160]

$$\begin{aligned}\mathbf{d}^{\mathrm{M}}_{\alpha\beta} = &\sum_{fu}\left(X^{\alpha}_{fu}X^{\beta}_{fu} - Y^{\alpha}_{fu}Y^{\beta}_{fu}\right)\left(\sum_{g\in\mathrm{occ}}\langle\phi_g|\hat{\mathbf{r}}|\phi_g\rangle - \langle\phi_f|\hat{\mathbf{r}}|\phi_f\rangle + \langle\phi_u|\hat{\mathbf{r}}|\phi_u\rangle\right)\\ &+\sum_{\substack{f,u\\ v\neq u}}\left(X^{\alpha}_{fu}X^{\beta}_{fv} - Y^{\alpha}_{fu}Y^{\beta}_{fv}\right)\langle\phi_u|\hat{\mathbf{r}}|\phi_v\rangle\\ &-\sum_{\substack{f,u\\ g\neq f}}\left(X^{\alpha}_{fu}X^{\beta}_{gu} - Y^{\alpha}_{fu}Y^{\beta}_{gu}\right)\langle\phi_f|\hat{\mathbf{r}}|\phi_g\rangle + \delta_{\alpha\beta}\sum_{A} Z_A\mathbf{R}_A. \end{aligned} \tag{2.33}$$

The resulting static and transition dipole moments $\mathbf{d}^{\mathrm{M}}_{\alpha\beta}$ from Eqs. (2.31)-(2.33) constitute the molecular part of the interaction in Eq. (2.28) required by the HyCI method, as discussed in Subsection 2.1.3.2. The next subsection is dedicated to the computation of the nanoparticle electric-field matrix elements entering the same interaction.

2.1.3.4 Electric-field matrix elements of the nanoparticle

The electric-field matrix elements $\mathbf{E}^{\mathrm{NP}}_{\nu\mu}(\mathbf{R}) \equiv \langle \mathrm{NP}_\nu|\, \hat{\mathbf{E}}^{\mathrm{NP}}(\mathbf{R})\, |\mathrm{NP}_\mu\rangle$, entering the HyCI coupling in Eq. (2.28), are evaluated in the MP excitonic basis. The electric-field operator is defined as the sum of all one-particle field operators generated by the nuclear and electronic charges of the nanoparticle.

Following the strategy introduced in Ref.[12, 18, 19] the electric-field operator is treated in second quantization and projected onto the single-exciton manifold. By inserting the MP expansion of the excitonic states defined in Eq. (2.19) into the field operator, one obtains CI-level working expressions for the electric-field matrix elements, which naturally separate into ground-to-exciton (interband) and exciton-to-exciton (intraband) contributions.

Interband and intraband matrix elements. The ground-to-exciton (*interband*) matrix elements between the nanoparticle ground state $|\mathrm{NP}_0\rangle$ and a single-exciton state $|\mathrm{NP}_\mu\rangle$ read [12]

$$\langle \mathrm{NP}_0|\, \hat{\mathbf{E}}^{\mathrm{NP}}(\mathbf{R})\, |\mathrm{NP}_\mu\rangle = \sum_{i,p} c^{\mu}_{ip}\ \langle p|\, \mathbf{E}(\mathbf{r};\mathbf{R})\, |i\rangle\,, \tag{2.34}$$

where i labels electron (conduction-band) states and p labels hole (valence-band) states. Here $\mathbf{E}(\mathbf{r};\mathbf{R})$ denotes the single-particle electric-field operator evaluated at $\mathbf{R}$ due to a unit charge at position $\mathbf{r}$ (defined below), and c^{μ}_{ip} is the Full-CI coefficient from Eq.(2.19).

Similarly, the exciton-to-exciton (*intraband*) electric-field matrix elements between $|\mathrm{NP}_\nu\rangle$ and $|\mathrm{NP}_\mu\rangle$ are given by [12]

$$\langle \mathrm{NP}_\nu|\, \hat{\mathbf{E}}^{\mathrm{NP}}(\mathbf{R})\, |\mathrm{NP}_\mu\rangle = -\sum_{i,j,p} c^{\nu\,*}_{ip} c^{\mu}_{jp}\, \langle i|\, \mathbf{E}(\mathbf{r};\mathbf{R})\, |j\rangle + \sum_{i,p,q} c^{\nu\,*}_{ip} c^{\mu}_{iq}\, \langle q|\, \mathbf{E}(\mathbf{r};\mathbf{R})\, |p\rangle\,, \tag{2.35}$$

where the first and second terms describe electron-electron and hole-hole contributions, respectively.

Implicit in Eqs. (2.34) and (2.35) is the assumption that the NP in its ground state is unpolarized, so that $\langle \mathrm{NP}_0 |\, \hat{\mathbf{E}}^{\mathrm{NP}}(\mathbf{R}) \,| \mathrm{NP}_0 \rangle = 0$, as a consequence of the cancellation between electronic and nuclear contributions. [12] This condition justifies the absence of additional diagonal terms in the intraband expression.

Multipole expansion of the one-particle electric field. To evaluate all SP matrix elements in Eqs. (2.34) and (2.35), we use a spherical multipole expansion of the Coulomb field including polarization effects at the NP surface. [12] The resultant expression (analogously valid for hole-hole or electron-hole contributions) can be written as

$$\langle i |\, \mathbf{E}(\mathbf{r};\mathbf{R}) \,| j \rangle = \frac{1}{\varepsilon_{\mathrm{out}}} \sum_{\ell,m} \frac{4\pi}{(\varepsilon+1)\ell+1}\, \langle i |\, r^{\ell} Y_{\ell m}(\Omega) \,| j \rangle\, \mathbf{G}_{\ell m}(\mathbf{R}). \tag{2.36}$$

Here, the geometry-dependent G-vector is defined by $\mathbf{G}_{\ell m}(\mathbf{R}) \equiv \nabla_{\mathbf{r}} \big(r^{-\ell-1} Y^*_{\ell m}(\Omega) \big) \big|_{\mathbf{r}=\mathbf{R}}$, which can be written explicitly as:

$$\begin{aligned} \mathbf{G}_{\ell m}(\mathbf{R}) = \Big\{ & -(\ell+1)\, r^{-\ell-2}\, Y^*_{\ell m}(\Omega)\, \mathbf{e}_r \\ & + r^{-\ell-2} \Big[\sqrt{(\ell+m+1)(\ell-m)}\, e^{i\phi}\, Y^*_{\ell,m+1}(\Omega) + m \cot\theta\, Y^*_{\ell m}(\Omega) \Big] \mathbf{e}_\theta \\ & - im\, r^{-\ell-2}\, \csc\theta\, Y^*_{\ell m}(\Omega)\, \mathbf{e}_\phi \Big\} \Big|_{\mathbf{r}=\mathbf{R}}, \end{aligned} \tag{2.37}$$

where $\mathbf{e}_r$, $\mathbf{e}_\theta$, and $\mathbf{e}_\phi$ are the spherical basis unit vectors.

On the other hand, matrix elements $\langle i |\, r^{\ell} Y_{\ell m}(\Omega) \,| j \rangle$ are referred to as *spherical multipole moments* and constitute the only quantities that depend explicitly on the electronic structure of the NP.

Spherical multipole moments within the EFA. Under the EFA, the dominant contribution to the spherical multipole moments reduces to a sum of two terms in which envelope-function matrix elements are multiplied by integrals of the Bloch conduction and/or valence band-functions. [12] Applying the orthonormality of the latter functions and keeping only the leading term of the sum, one can then obtain distinct expressions for the *intraband* and *interband* cases in Eqs. (2.34) and (2.35).

For *intraband* matrix elements, the previous procedure yields

$$\langle i |\, r^{\ell} Y_{\ell m}(\Omega) \,| j \rangle \approx \langle f_i |\, r^{\ell} Y_{\ell m}(\Omega) \,| f_j \rangle\,, \qquad \langle q |\, r^{\ell} Y_{\ell m}(\Omega) \,| p \rangle \approx \langle f_q |\, r^{\ell} Y_{\ell m}(\Omega) \,| f_p \rangle\,. \tag{2.38}$$

In the case of *interband* matrix elements, one obtains

$$\langle p |\, r^{\ell} Y_{\ell m}(\Omega) \,| i \rangle \approx \langle f_p |\, \nabla \big(r^{\ell} Y_{\ell m}(\Omega) \big) \,| f_i \rangle \cdot \langle u_v |\, \mathbf{r} \,| u_c \rangle_{\mathrm{cell}}\,. \tag{2.39}$$

where $\langle | \cdot | \rangle_{\mathrm{cell}} \equiv \frac{1}{V_{cell}} \int_{\mathrm{cell}} d^3 r$ with V_{cell} the unit cell volume. The matrix element $\langle u_v |\, \mathbf{r} \,| u_c \rangle_{\mathrm{cell}}$ is called the bulk transition dipole. [153, 154]

Semi-analytical expressions for all envelope-function integrals appearing above are reported in Appendix A.2. Importantly, owing to the spherical symmetry of the NP, these matrix elements obey strict angular-momentum selection rules, which lead to an exact truncation of

the multipole expansion in Eq. (2.36). As a result, only a finite number of multipole orders ℓ contribute to the electric-field matrix elements in Eqs. (2.34) and (2.35). This allows all relevant multipolar contributions to be included, in principle.

The overall strength and polarization in Eq. (2.39) depend on the bulk transition dipole, which is a material-specific parameter.

Bulk transition dipole and spin channels in wurtzite. In materials with a wurtzite crystal structure, such as CdSe or GaN, two distinct bulk transition dipoles arise from different spin channels (+ and −) of the excitonic states (see subsection 2.1.2.2). The magnitude of these dipoles is set by the ratio $P/E_{\mathrm{gap}}^{\mathrm{bulk}}$, where P denotes the bulk transition momentum and $E_{\mathrm{gap}}^{\mathrm{bulk}}$ is the bulk band gap. [153, 154] Their orientations, however, are determined by the intrinsic anisotropy of the hexagonal wurtzite lattice, which defines a bright-excitation plane within the otherwise nearly spherical quantum dot. [19] Each spin channel therefore selects a preferred polarization direction, with the two polarizations being mutually orthogonal.

Following the spin-resolved description adopted in Refs. [18, 19], the bulk transition dipoles originate from in-plane Kane matrix elements between S-like conduction and P-like valence Bloch states, but admit an equivalent representation through a rotation of the polarization frame such that each spin channel is associated with a single effective component along a chosen quantization axis, without loss of generality. We therefore select the coordinate system so that the z axis is aligned with the spin-up channel, leading to the bulk transition dipole

$$\langle u_v |\, \mathbf{r} \,| u_c \rangle_{\mathrm{cell}}^{+} = \frac{iP}{E_{\mathrm{gap}}^{\mathrm{bulk}}}\, \mathbf{e}_z. \tag{2.40}$$

In this reference framework, only the z-component of the gradient contributes to the scalar product in Eq. (2.39). Consequently, the evaluation of the envelope-function integrals can be restricted to the z component only, $F_{\ell m}^{z} \equiv \mathbf{e}_z \cdot \nabla\big(r^{\ell} Y_{\ell m}(\Omega)\big)$, thereby reducing the calculation effort. Such component admits semi-analytical expressions reported in Appendix A.2.

The *interband* electric field associated with the spin-down channel (−) can be obtained from the spin-up (+) one through a unitary transformation in the complex plane. [12] Explicitly, one finds

$$\langle \mathrm{NP}_0 |\, \mathbf{E}(\mathbf{R}) \,| \mathrm{NP}_{\mu}^{-} \rangle = -i\, T^{-1} \langle \mathrm{NP}_0 |\, \mathbf{E}(T\mathbf{R}) \,| \mathrm{NP}_{\mu}^{+} \rangle\,, \tag{2.41}$$

where T denotes a real-space rotation about the x axis, defined by $T\mathbf{e}_x = \mathbf{e}_x$ and $T\mathbf{e}_y = \mathbf{e}_z$. Note that the electric field on the right-hand side has to be evaluated at the rotated coordinate $T\mathbf{R}$. Spin-up and spin-down electric fields are not required to be mutually orthogonal in real space, even though their associated bulk transition dipoles are. The *intraband* spherical multipoles, and consequently the MP *intraband* electric fields, do not depend on the bulk transition dipole (see Eqs. (2.38) and (2.35)), and are therefore identical for both spin channels.

Equations (2.34)–(2.41) provide the interband electric-field matrix elements $\mathbf{E}_{0\mu^+}^{NP}(\mathbf{R})$ and $\mathbf{E}_{0\mu^-}^{NP}(\mathbf{R})$, together with the intraband $\mathbf{E}_{\nu\mu}^{NP}(\mathbf{R})$ ones, required for the HyCI interaction in Eq. (2.28). The following section introduces the hybrid dipole moments, which are used to characterize the nature of the excitations in hybrid nanosystems.

2.1.3.5 Hybrid M-NP dipoles moments

The total dipole operator of the M-NP nanohybrid is written as

$$\hat{\mathbf{d}} = \hat{\mathbf{d}}^{\mathrm{M}} \otimes \hat{\mathbb{I}}^{\mathrm{NP}} + \hat{\mathbb{I}}^{\mathrm{M}} \otimes \hat{\mathbf{d}}^{\mathrm{NP}}. \tag{2.42}$$

where $\hat{\mathbf{d}}^{\mathrm{M}}$ acts only on the M subspace and $\hat{\mathbf{d}}^{\mathrm{NP}}$ only on the NP subspace. After diagonalizing the HyCI Hamiltonian in Eq.(2.24), and given the HyCI expansion by Eq.(2.25), the molecular contribution to the dipole matrix element between two hybrid states is

$$\langle \Psi_{\mathcal{I}} | \, \hat{\mathbf{d}}^{\mathrm{M}} \, | \Psi_{\mathcal{J}} \rangle = \sum_{\alpha,\beta,\nu} C^{\mathcal{I}\,*}_{\alpha\nu} \, C^{\mathcal{J}}_{\beta\nu} \, \langle M_{\alpha} | \, \hat{\mathbf{d}}^{\mathrm{M}} \, | M_{\beta} \rangle \, , \tag{2.43}$$

where $C^{\mathcal{I}}_{\alpha\nu}$ are the HyCI coefficients and the molecular dipole moments are computed in Section 2.1.3.3. Analogously, the nanoparticle contribution is given by

$$\langle \Psi_{\mathcal{I}} | \, \hat{\mathbf{d}}_{\mathrm{NP}} \, | \Psi_{\mathcal{J}} \rangle = \sum_{\alpha,\nu,\mu} C^{\mathcal{I}\,*}_{\alpha\nu} \, C^{\mathcal{J}}_{\alpha\mu} \, \langle \mathrm{NP}_{\nu} | \, \hat{\mathbf{d}}^{\mathrm{NP}} \, | \mathrm{NP}_{\mu} \rangle \, . \tag{2.44}$$

These relations allow the optical response of each hybrid excitation to be resolved into molecular and nanoparticle components, enabling analysis of oscillator-strength redistribution under changes in geometry, NP size, or photoswitch-reaction coordinates.

In Eq(2.44), we are left to computing the NP dipole moments. Their derivation follows exactly the same strategy adopted in the previous subsection for the electric-field operator, as detailed in Ref.12, 18, 19. Starting from the second-quantized form of the dipole operator and projecting it onto the single-exciton manifold, one obtains CI-level expressions that naturally separate into interband and intraband contributions.

The ground-to-exciton (*interband*) dipole matrix elements between the NP ground state $|\mathrm{NP}_0\rangle$ and a single-exciton state $|\mathrm{NP}_{\mu}\rangle$ read

$$\langle \mathrm{NP}_0 | \, \hat{\mathbf{d}}^{\mathrm{NP}} \, | \mathrm{NP}_{\mu} \rangle = - \sum_{i,p} c^{\mu}_{ip} \, \langle p | \, \mathbf{r} \, | i \rangle \, , \tag{2.45}$$

where $\langle p | \, \mathbf{r} \, | i \rangle$ denotes the SP interband dipole matrix element and c^{μ}_{ip} is the Full-CI coefficient from Eq.(2.19). Similarly, the exciton-to-exciton (*intraband*) dipole matrix elements between $|\mathrm{NP}_{\nu}\rangle$ and $|\mathrm{NP}_{\mu}\rangle$ are given by

$$\langle \mathrm{NP}_{\nu} | \, \hat{\mathbf{d}}^{\mathrm{NP}} \, | \mathrm{NP}_{\mu} \rangle = - \sum_{i,j,p} c^{\nu\,*}_{ip} c^{\mu}_{jp} \, \langle i | \, \mathbf{r} \, | j \rangle + \sum_{i,p,q} c^{\nu\,*}_{ip} c^{\mu}_{iq} \, \langle q | \, \mathbf{r} \, | p \rangle \, , \tag{2.46}$$

where the first and second terms correspond to electron-electron and hole-hole contributions, respectively. As in the case of the electric-field operator, the assumption of an unpolarized NP ground state implies $\langle \mathrm{NP}_0 | \, \hat{\mathbf{d}}^{\mathrm{NP}} \, | \mathrm{NP}_0 \rangle = 0$, so that no additional diagonal terms appear in Eq.(2.46).

The explicit evaluation of the SP dipole matrix elements proceeds using the same envelope-function and symmetry considerations discussed in the previous section. For *intraband* SP dipole matrix elements, the dominant contribution originates from the envelope-function part, yielding

$$\langle i | \, \mathbf{r} \, | j \rangle \approx \langle f_i | \, \mathbf{r} \, | f_j \rangle \, , \qquad \langle q | \, \mathbf{r} \, | p \rangle \approx \langle f_q | \, \mathbf{r} \, | f_p \rangle \, . \tag{2.47}$$

For *interband* SP dipole matrix elements, the leading contribution is instead governed by the bulk transition dipole, multiplied by the overlap of the envelope functions. One obtains

$$\langle p|\,\mathbf{r}\,|i\rangle \approx \langle f_p|f_i\rangle\ \langle u_v|\,\mathbf{r}\,|u_c\rangle_{\text{cell}}\,. \tag{2.48}$$

Choosing the z axis to be aligned with the spin-up channel (+) of the bulk transition dipole directly makes the SP *interband* dipoles to be polarized along z (see Eqs. (2.40) and (2.48)). As a consequence, the MP *interband* dipoles in Eq.(2.45) are always polarized along z, while *intraband* ones depend on envelope-function integrals.

Once the spin-up *interband* MP dipoles are known, the corresponding spin-down counterparts follow directly from the transformation

$$\langle \mathrm{NP}_0|\,\hat{\mathbf{d}}^{NP}\,|\mathrm{NP}_\nu^-\rangle = -i\,T^{-1}\,\langle \mathrm{NP}_0|\,\hat{\mathbf{d}}^{NP}\,|\mathrm{NP}_\nu^+\rangle\,, \tag{2.49}$$

where T denotes a real-space rotation about the x axis, defined by $T\mathbf{e}_x = \mathbf{e}_x$ and $T\mathbf{e}_y = \mathbf{e}_z$. Similar to the electric-field case, the *intraband* MP dipoles are identical for both spin channels.

All envelope-function integrals appearing in Eqs. (2.47)-(2.48) admit semi-analytical expressions. Their explicit forms, together with the associated angular-momentum selection rules, are reported in the Appendix A.3.

2.1.4 Numerical workflow and implementation of HyCI

The full HyCI methodology and description of hybrid states can be summarized as the computation of the fragment-level inputs

$$\Big\{\,|M_\alpha\rangle\,,\ E_\alpha^{\mathrm{M}},\ \mathbf{d}_{\alpha\beta}^{\mathrm{M}}\Big\},\qquad \Big\{\,|\mathrm{NP}_\nu\rangle\,,\ E_\nu^{\mathrm{NP}},\ \mathbf{E}_{\nu\mu}^{NP}(\mathbf{R}),\mathbf{d}_{\nu\mu}^{\mathrm{NP}}\Big\}, \tag{2.50}$$

followed by assembly and diagonalization of the HyCI Hamiltonian in Eq. (2.24) to obtain the hybrid quantities

$$\Big\{\,|\Psi_{\mathcal{I}}\rangle\,,\ E_{\mathcal{I}},\ C_{\alpha\nu}^{\mathcal{I}},\ \mathbf{d}_{\mathcal{I}\mathcal{J}}\Big\}. \tag{2.51}$$

For clarity and future reference, we briefly summarize how these quantities are defined and computed within the formalism introduced in this chapter. Molecular ground and excited states $|M_\alpha\rangle$ and energies E_α^{M} are obtained from DFT and LR-TDDFT calculations (Sections 2.1.1.1 and 2.1.1.2), with ground-state and excited-state energies defined by Eqs. (2.5) and (2.13), respectively. Molecular dipole matrix elements $\mathbf{d}_{\alpha\beta}^{\mathrm{M}}$ are computed as detailed in Section 2.1.3.3. Nanoparticle excitonic states $|\mathrm{NP}_\nu\rangle$ and energies E_ν^{NP} are obtained by diagonalization of the excitonic Hamiltonian, yielding the states defined in Eq. (2.19). The excitonic electric-field matrix elements $\mathbf{E}_{\nu\mu}^{\mathrm{NP}}(\mathbf{R})$ entering the HyCI coupling and the nanoparticle dipole matrix elements $\mathbf{d}_{\nu\mu}^{\mathrm{NP}}$ are computed as described in Section 2.1.3.4.

The numerical workflow mirrors the fragment-first philosophy of HyCI and is organized into three main stages: molecular calculations, nanoparticle calculations, and hybrid-state construction.

Molecular fragment. Molecular electronic-structure calculations and post-processing are carried out using the following programs:

- **Gaussian 16** [161]: used to optimize molecular geometries and compute ground-state and excited-state energies and properties within KS-DFT and LR-TDDFT. It provides ground-state energies E_0^{M}, excitation energies ω_I, the ground-state dipole $\mathbf{d}_{00}^{\mathrm{M}}$, ground-to-excited-state transition dipoles $\mathbf{d}_{0\alpha}^{\mathrm{M}}$, and orbital information required for post-processing.
- **Multiwfn** [162]: employed to compute excited-excited static and transition dipoles $\mathbf{d}_{\alpha\beta}^{\mathrm{M}}$ via transition-density-matrix analysis.
- **Rodrigues.py** (custom): used to explore different mutual orientations between fragments by rotating molecular dipole vectors using Rodrigues' rotation formula, which provides the exact rotation of a vector about an arbitrary axis. The same rotation is applied consistently to all static and transition dipoles used as HyCI inputs. [163]

Nanoparticle fragment. The electronic structure of the quantum dot is computed within EFA using a sequence of FORTRAN programs introduced in Ref. 18, 19, 137, 156, 157, 158, 159:

- `spsolver.x`: solves the effective-mass single-particle problem on a finite-difference grid to obtain electron and hole envelope functions $f_{i,p}^{(e,h)}$ and energies $E_{i,p}^{(e,h)}$.
- `coulombel3D.x`: evaluates the two-particle Coulomb integrals entering the excitonic Hamiltonian.
- `citool.x`: diagonalizes the single-exciton Full-CI Hamiltonian, yielding QD exciton energies E_ν^{NP} and expansion coefficients c_{ip}^{ν}.
- `fields.x`: computes excitonic electric-field matrix elements $\mathbf{E}_{\nu\mu}^{\mathrm{NP}}(\mathbf{R})$ in the excitonic basis.
- `dipoles.x`: computes nanoparticle dipole matrix elements $\mathbf{d}_{\nu\mu}^{\mathrm{NP}}$ in the excitonic basis.

Hybrid M-NP states. Hybrid excitonic states are obtained using a dedicated FORTRAN implementation of the HyCI method, originally developed by Gil *et al.* [12, 18, 19]:

- `hyci.x`: constructs the HyCI Hamiltonian matrix in Eq. (2.24) using the dipole–field coupling, diagonalizes it, and evaluates hybrid dipole matrix elements $\mathbf{d}_{\mathcal{I}\mathcal{J}}$. The resulting HyCI Hamiltonian matrices can reach large dimensions depending on the retained fragment manifolds, motivating efficient construction and diagonalization strategies. For large basis sizes, a Lanczos scheme is employed to target selected spectral windows; convergence is controlled by energy cutoffs on the fragment manifolds and by multipole truncation in the QD field expansion.

Workflow automation and post-processing. The preparation, execution, and analysis of HyCI calculations are supported by a custom workflow package developed in this work:

- `hyci_workflow` (custom package): a collection of Python scripts and PBS shell utilities that automates directory creation and input-file generation for electronic-structure and HyCI calculations, performs systematic parameter sweeps over QD size, inter-fragment separation, HyCI energy cutoffs, multipole truncation, molecular orientation, and internal

molecular coordinates (e.g. the CNNC dihedral angle in AZB), enables automated execution on HPC infrastructures, and provides post-processing tools for data aggregation, fitting, and visualization.

The Lanczos diagonalization scheme, compact storage and vector-matrix multiplication of sparse HyCI matrices, as well as the shared-memory parallelization of the `fields.x`, `dipoles.x`, and `hyci.x` programs (including matrix construction and diagonalization), were implemented in this work.

2.2 Transport of indirect excitons in Coupled Quantum Wells

We follow Ref. 131 and model a SAW-driven SIX in a CQW as a correlated quasi-electron and heavy-hole pair confined to move along the SAW transport axis x. The coordinate system is defined such that the growth direction of the nanostructure is denoted by z, while y labels the transverse in-plane direction perpendicular to transport. The x axis is chosen midway between the electron and hole layers, so that the electron and hole are located at fixed positions $z = +d/2$ and $z = -d/2$, respectively, where d denotes the inter-well separation. A schematic of this geometry is provided in Section 1.2 (see Fig. 1.5).

In the presence of external potentials that act differently on the electron and hole, such as piezoelectric SAW fields and localized electrostatic impurities, the internal and center-of-mass (CoM) degrees of freedom of the exciton become dynamically coupled. As a result, a reduced single-particle description is generally insufficient to capture excitonic transport and scattering processes, motivating a fully correlated two-body treatment.

2.2.1 Correlated two-particle model for SAW-driven SIXs

We introduce the center-of-mass (CoM) and relative coordinates,

$$X_{\mathrm{cm}} = \frac{m_e x_e + m_h x_h}{M}, \qquad x_r = x_e - x_h, \tag{2.52}$$

where m_e and m_h denote the effective masses of the quasi-electron and heavy hole, respectively, and $M = m_e + m_h$ is the total mass, with reduced mass $m = (m_e^{-1} + m_h^{-1})^{-1}$. Within this representation, the excitonic dynamics along the transport direction can be treated fully quantum mechanically.

For computational convenience, the transport problem is formulated in the reference frame co-moving with the SAW, which propagates along the negative x direction with group velocity v_{SAW} (see Fig. 1.5). In this frame, the Hamiltonian reads [131]

$$\hat{H}(t) = \frac{\hat{P}^2}{2M} + \frac{\hat{p}^2}{2m} + U_{\mathrm{Coul}}(x_r) + U_{\mathrm{SAW}}(X_{\mathrm{cm}}, x_r) + U_{\mathrm{imp}}(X_{\mathrm{cm}}, x_r; t), \tag{2.53}$$

where $\hat{P}$ and $\hat{p}$ are the momenta conjugate to X_{cm} and x_r, respectively. The first two terms describe the free propagation of the excitonic CoM and the internal relative motion. The remaining contributions account for Coulomb binding, SAW-induced confinement, and impurity-induced time-dependent scattering, which together define a driven quantum system in which correlation effects can emerge during transport.

The electron-hole interaction is described by a softened interlayer Coulomb potential that naturally incorporates the inter-well separation d,

$$U_{\text{Coul}}(x) = \frac{q_e q_h}{4\pi\varepsilon_0\varepsilon_r\sqrt{x_r^2 + d^2}}, \tag{2.54}$$

where ε_r is the relative dielectric constant of the CQW semiconductor material and $q_e(q_h)$ is the electron (hole) charge. The static screening approximation is appropriate for transport due to the low-frequency SAWs investigated in this work.

The SAW generates piezoelectric potentials that act differently on the electron and hole,

$$U_{\text{SAW}}(X_{cm}, x_r) = U_{e,0}\sin\left(\frac{2\pi}{\lambda_{\text{SAW}}}\left(X_{cm} + \frac{m_h}{M}x_r\right)\right) + U_{h,0}\sin\left(\frac{2\pi}{\lambda_{\text{SAW}}}\left(X_{cm} - \frac{m_e}{M}x_r\right)\right). \tag{2.55}$$

Here $U_{e,0}$ and $U_{h,0}$ denote the amplitudes of the piezoelectric SAW potential acting on the electron and hole, respectively, and λ_{SAW} is the SAW wavelength. This form makes explicit that the SAW potential depends simultaneously on the CoM and relative coordinates, thereby coupling translational motion to the internal electron–hole dynamics and allowing internal excitations even in the absence of disorder. [131]

Because the SAW wavelength is much larger than the effective Bohr radius of the exciton, $\lambda_{\text{SAW}} \gg a_B^*$, the initial wave packet trapped at a SAW valley can be well approximated by a separable product, [132]

$$\Psi(X_{cm}, x_r, 0) = \chi_{\text{HO}}(X_{cm})\,\phi_0(x_r), \tag{2.56}$$

where $\phi_0(x_r)$ is the ground state obtained by diagonalizing the free-relative part of the Hamiltonian in Eq.(2.53) including U_{Coul}. The function $\chi_{\text{HO}}(X_{cm})$ is the CoM ground state associated with the harmonic approximation of the SAW potential at one of its minima, denoted by X_0, and evaluated at $x_r \simeq 0$. The resulting ground-state CoM wave function reads [131]

$$\chi_{\text{HO}}(X_{cm}) = \left(\frac{M\omega_{\text{HO}}}{\pi\hbar}\right)^{1/4} e^{-\frac{(X_{cm}-X_0)^2}{4\sigma_{\text{HO}}^2}}, \tag{2.57}$$

where $\omega_{\text{HO}} = \frac{2\pi}{\lambda_{\text{SAW}}}\sqrt{\frac{|U_{e,0}+U_{h,0}|}{M}}$ and $\sigma_{\text{HO}}^2 = \hbar/(2M\omega_{\text{HO}})$. This construction ensures that the internal excitonic motion is initially well localized compared to the spatial variation of the SAW potential.

Electrostatic scattering is modeled by a single screened impurity located at $(x_{\text{imp}}^0, y_{\text{imp}}, z_{\text{imp}})$ with $x_{\text{imp}}^0 < X_0 - \lambda_{SAW}/2$ (see Fig. 1.5). The transverse coordinate satisfies $y_{\text{imp}} \neq 0$ in order to avoid the on-axis singularity of a point-like impurity potential, while the growth coordinate z_{imp} can take arbitrary values.

In the frame co-moving with the SAW, the position of the impurity along the transport axis changes in time and is given by $x_{\text{imp}}(t) = x_{imp}^0 + v_{\text{SAW}}t$. The resulting scattering potential is described by a time-dependent 3D Debye-like Coulomb interaction centered at $(x_{\text{imp}}(t), y_{\text{imp}}, z_{\text{imp}})$,

$$U_{\text{imp}}(X_{cm}, x_r; t) = \frac{q_{\text{imp}}}{4\pi\varepsilon_0\varepsilon_r}\left[q_e\,\frac{\exp[-r_e(X_{cm}, x_r; t)/l_D]}{r_e(X_{cm}, x_r; t)} + q_h\,\frac{\exp[-r_h(X_{cm}, x_r; t)/l_D]}{r_h(X_{cm}, x_r; t)}\right], \tag{2.58}$$

where the electron– and hole–impurity distances are given by

$$r_e(X_{cm}, x_r; t) = \sqrt{\left[X_{cm} + \frac{m_h}{M}x_r - x^0_{imp} - v_{\mathrm{SAW}}t\right]^2 + y^2_{\mathrm{imp}} + z^2_{\mathrm{imp}}}, \tag{2.59}$$

$$r_h(X_{cm}, x_r; t) = \sqrt{\left[X_{cm} - \frac{m_e}{M}x_r - x^0_{imp} - v_{\mathrm{SAW}}t\right]^2 + y^2_{\mathrm{imp}} + z^2_{\mathrm{imp}}}. \tag{2.60}$$

Here q_{imp} denotes the impurity charge, q_e (q_h) is the electron (hole) charge, and l_D is an effective Debye screening length accounting for static screening by mobile carriers in the nanostructure. For simplicity, a single screening length is used for both electron and hole impurity interactions.

Assuming a non-degenerate carrier gas, the screening length can be estimated as [164]

$$l_D = \sqrt{\frac{\varepsilon_0 \varepsilon_r k_B T_K}{n q_e^2}}, \tag{2.61}$$

where ε_r is the relative dielectric constant, T_K is the temperature, n is the effective 3D free-carrier density and k_B is the Boltzmann constant.

2.2.2 Numerical propagation and observables of SAW-SIXs

The time evolution of the full two-particle wave function $\Psi(X_{cm}, x_r; t)$ is obtained using a unitary Fourier split-step (FSS) scheme, [131]

$$\Psi(t+\Delta t) = e^{-\frac{i}{\hbar}U(t+\Delta t/2)\frac{\Delta t}{2}} e^{-\frac{i}{\hbar}K\Delta t} e^{-\frac{i}{\hbar}U(t+\Delta t/2)\frac{\Delta t}{2}} \Psi(t), \tag{2.62}$$

where $K = \hat{P}^2/2M + \hat{p}^2/2m$ and $U = U_{\mathrm{Coul}} + U_{\mathrm{SAW}} + U_{\mathrm{imp}}$.

The FSS scheme is second-order accurate in the time steps, and exploits the fact that the kinetic operator is diagonal in momentum space, whereas the potential terms are diagonal in coordinate space. External potentials are evaluated at half time to allow time-reversal symmetry and numerical stability.

In practice, the kinetic propagator is applied in the conjugate momentum variables (P, p) via a 2D Fast Fourier Transform (FFT) in the (X_{cm}, x_r) grid. [165] Denoting by $\mathcal{F}_{X_{cm},x_r}$ the Fourier transform $\Psi(X_{cm}, x_r) \mapsto \tilde{\Psi}(P, p)$, one time step reads

$$\begin{aligned}\Psi^{n+1}(X_{\mathrm{cm}}, x_r) = e^{-\frac{i}{\hbar}U(X_{\mathrm{cm}},x_r;t_{n+1/2})\frac{\Delta t}{2}}\, \mathcal{F}^{-1}_{X_{\mathrm{cm}},x_r} \times \\ \times \left[e^{-\frac{i}{\hbar}\left(\frac{P^2}{2M}+\frac{p^2}{2m}\right)\Delta t}\, \mathcal{F}_{X_{\mathrm{cm}},x_r}\left(e^{-\frac{i}{\hbar}U(X_{\mathrm{cm}},x_r;t_{n+1/2})\frac{\Delta t}{2}} \Psi^n(X_{\mathrm{cm}}, x_r)\right)\right],\end{aligned} \tag{2.63}$$

with $t_{n+1/2} = t_n + \Delta t/2$. To suppress finite-domain artifacts, the X_{cm} grid is chosen sufficiently large that the scattered wave packet does not reach the numerical boundaries over the simulated time window, so that periodic wrap-around effects inherent to FFT-based propagation are negligible.

Transport is characterized with a transmission coefficient, which in the co-moving frame with the SAW is defined as

$$T = \int_{|X_{cm}-X_0|<\lambda_{\mathrm{SAW}}/2} \rho_{\mathrm{cm}}(X_{cm}; t_f)\, dX_{cm}, \tag{2.64}$$

where t_f is chosen sufficiently large that scattering is complete, and the CoM marginal density is defined as

$$\rho_{\rm cm}(X_{cm};t) = \int dx_r \, |\Psi(X_{cm},x_r;t)|^2. \tag{2.65}$$

In the co-moving frame, this definition measures the probability for the exciton to remain localized within the potential valley associated with its initial SAW minimum. In the laboratory frame, this corresponds to the probability that the exciton is successfully transported along the SAW without being scattered out of its initial SAW valley.

To assess the role of electron-hole correlations, the transmission coefficient is also computed within a rigid-exciton (RIX) approximation. [131] In this model, the internal relative-coordinate state of the exciton is frozen to its ground state $\phi_0(x_r)$, and only the CoM motion is propagated. The resulting effective potential acting on the center of mass is obtained by averaging the external fields over the relative coordinate,

$$U_{\rm RIX}(X_{cm};t) = \int dx \left[U_{\rm SAW}(X_{cm},x_r) + U_{\rm imp}(X_{cm},x_r;t)\right]|\phi_0(x_r)|^2, \tag{2.66}$$

yielding the effective 1D Hamiltonian:

$$H_{\rm RIX}(t) = \frac{\hat{P}^2}{2M} + U_{\rm RIX}(X_{cm};t), \tag{2.67}$$

that neglects internal excitations and dissociation channels. [131] Deviations between the RIX and full two-body results therefore provide a direct measure of correlation-driven transport effects.

The computational workflow for SAW-driven SIX transport proceeds as follows. First, the free relative Hamiltonian associated with Eq. (2.53) is diagonalized (including the Coulomb interaction in Eq. (2.54)) to obtain the relative ground state wave function $\phi_0(x_r)$ entering the separable initial condition in Eq. (2.56). Second, the CoM ground state $\chi_{\rm HO}(X_{cm})$ is constructed from the Gaussian form in Eq. (2.57), and the initial excitonic wave packet is prepared as $\Psi(X_{cm},x_r;0) = \chi_{\rm HO}(X_{cm})\phi_0(x_r)$ [Eq. (2.56)] localized at a SAW minimum X_0. Third, the full two-body wave function is propagated according to the Fourier split-step (FSS) scheme in Eq. (2.63), using the total potential $U = U_{\rm Coul} + U_{\rm SAW} + U_{\rm imp}$ with $U_{\rm SAW}$ and $U_{\rm imp}$ given by Eqs. (2.55) and (2.58), respectively, and the screening length set by Eq. (2.61). Finally, transport observables are extracted from the propagated wave function by evaluating the CoM marginal density $\rho_{\rm cm}(X_{cm};t)$ [Eq. (2.65)] and the transmission coefficient T [Eq. (2.64)], and compared against the RIX approximation defined through the effective Hamiltonian in Eq. (2.67).

All these steps are carried out with a FORTRAN program (`std2P1Drc_TDH.x`) originally developed in Ref. 131. In the present work, this code has been extended to include the additional impurity-like external potential $U_{\rm imp}(X_{cm},x_r;t)$ introduced in Eq. (2.58), while all remaining components of the numerical framework follow the original implementation. Finally, post-processing of the propagated wave functions, including the evaluation of marginal densities and transmission coefficients, is performed using custom analysis scripts in Python.

2.3 Connection to the Following Chapters

The methods outlined in Section 2.1 provide the theoretical backbone for the two M-NP case studies developed in this thesis. Chapter 3 assesses HyCI on a prototypical CPh-QD system of H_2P-GaN, focusing on energy convergence and scaling trends for hybrid splittings. Chapter 4 applies the same methodology along a key photoisomerization coordinate of an AZB-CdSe nanohybrid, demonstrating how intrinsic excitonic coupling can reshape the hybrid excited-state landscape and modulate photoisomerization pathways in a cavity-free setting.

In addition, the methods outlined in Section 2.2 underpin the modeling of time-dependent two-body exciton dynamics in the presence of a localized impurity presented in Chapter 5 for a prototypical GaAs/AlGaAs CQW. This framework shows that exciton transport is strongly influenced by impurity position and highlights the essential role of electron–hole correlations in shaping the resulting dynamics.

Chapter 3

Hybrid excitonic states in chromophore–quantum dot nanohybrids

3.1 Introduction and scope

In this chapter, the Hybrid Configuration Interaction (HyCI) framework introduced in Section 2.1 is applied to chromophore–quantum dot (CPh–QD) nanohybrids to characterize the formation and properties of hybrid excitonic states. We focus on a prototypical system composed of porphine (H_2P) coupled to a gallium nitride quantum dot (GaNQD), where localized molecular excitations interact with size-tunable, delocalized nanoparticle excitons.

Within the HyCI approach, molecular and nanoparticle excitations are first characterized independently, and their interaction is then treated explicitly at the excitonic level. This enables a non-perturbative description of hybrid excited states, capturing resonance conditions, avoided crossings, and the redistribution of oscillator strength that arise from genuine molecule–nanoparticle coupling.

A central milestone of this chapter is to establish a detailed and controlled description of excitonic hybridization in CPh–QD systems. We disentangle the roles of QD size, molecular orientation, and center-to-center separation in shaping the hybrid excitonic spectrum, with particular emphasis on the emergence of avoided crossings and on the associated exchange of molecular and nanoparticle state character.

In addition, the interaction mechanisms governing hybridization are rationalized through the analysis of scaling laws with respect to molecular orientation and intermolecular distance at resonance. Numerical convergence with respect to basis-set truncation and multipole cutoff is then examined at representative resonance conditions, providing quantitative estimates of truncation errors and validating the robustness of the physical interpretation.

In realistic colloidal realizations of chromophore–quantum dot nanohybrids, the semiconductor core is typically surrounded by organic surface ligands that passivate dangling bonds, suppress non-radiative recombination, and ensure optical activity. [166, 167] In the present study, these ligands are intentionally neglected to isolate the intrinsic excitonic interaction between molecular and quantum-dot excitations within a well-defined reference framework. Their inclusion would primarily lead to quantitative renormalizations of the effective coupling—through

increased molecule–quantum-dot separation and dielectric screening of the near-field Coulomb interaction—and could introduce additional localized electronic states outside the band-edge excitonic manifold considered here. [168] These effects are therefore expected to modify parameter values rather than the underlying physical mechanism captured by the present description, which should be regarded as a controlled starting point for extensions toward more realistic ligand-passivated nanohybrids.

The results presented in this chapter form the basis of a manuscript currently in preparation for submission to a peer-reviewed journal. [169] They also provide the conceptual framework for Chapter 4, where related hybrid excitonic mechanisms are shown to influence photochemical pathways in photoswitch–quantum dot nanohybrids.

This chapter proceeds from fragment-specific properties to hybrid excitonic behavior. Section 3.2 summarizes the system-specific numerical parameters and computational setup used to implement the HyCI framework. Section 3.3 analyzes the excitation spectra of the isolated H_2P and GaNQD and identifies the resonance conditions relevant for hybridization. Section 3.4 presents the formation of hybrid excitonic states and the emergence of avoided crossings as a function of quantum-dot size. Section 3.5 examines the angular and distance scaling laws governing excitonic coupling at resonance. Numerical convergence and truncation effects are then discussed in Section 3.6. Finally, Section 3.7 summarizes the main findings and outlines perspectives for subsequent applications.

3.2 Parameters and computational details

The physical and material parameters employed for the GaN quantum dot (GaNQD) and for the porphine–GaNQD hybrid system are summarized in Table 3.1. Unless explicitly stated otherwise, these parameters are fixed throughout this chapter.

Table 3.1: Parameters used for GaNQD and H_2P–GaNQD calculations.

Parameter	Symbol / Units	Value / Source
GaN effective electron mass	m_e^* [m_0]	0.220 (Ref. 170)
GaN effective heavy-hole mass	m_h^* [m_0]	1.010 (Ref. 170)
GaN optical dielectric constant	$\varepsilon_{\mathrm{QD}}$ [ε_0]	5.20 (Ref. 170)
Environment dielectric constant	ε_{out} [ε_0]	1 (vacuum)
GaN bulk band gap	$E_{\mathrm{gap}}^{\mathrm{bulk}}$ [eV]	3.44 (Ref. 170)
GaN bulk transition momentum	P [a.u.]	1.18 (Ref. 171)
Porphine characteristic radius	$R_{\mathrm{H_2P}}$ [nm]	0.533 (Ref. 172)
H van der Waals radius	$R_{\mathrm{VdW}}^{\mathrm{H}}$ [nm]	0.167 (Ref. 173)

Electronic-structure calculations for the porphine (H_2P) molecule were carried out in vacuum for its ground and first 100 excited states. A single optimized ground-state geometry was employed throughout this chapter. Geometry optimization was performed using the CAM-B3LYP range-separated hybrid exchange-correlation functional in combination with the def2+TZVPPD basis set. Excited-state energies and transition properties were subsequently computed at the same level of theory to ensure internal consistency between ground- and excited-state descriptions. No symmetry constraints were imposed during geometry optimization.

All ground- and excited-state computations in H_2P were carried out with very high numerical accuracy: a dense integration grid (*Ultrafine*) and stringent convergence thresholds (*VeryTight*) were employed for self-consistent-field (SCF) calculations and geometry optimizations, as implemented in *Gaussian 16*. Additionally, quadratic convergence (*QC*) was enabled to enhance SCF stability, and a threshold of 10^{-6} a.u. was applied for Davidson diagonalization in the LR-TDDFT calculations.

On the nanoparticle side, GaNQDs with radii $R_{\mathrm{QD}} = 2$–5 nm were considered, ensuring the applicability of the envelope-function approximation described in Section 2.1.2.1. While solving for the single-particle (SP) electron and hole states, a grid of 8192 points was used for the envelope functions, ensuring convergence of SP energies within approximately 0.1 meV. The surrounding environment of the QD was taken as vacuum, matching the H_2P gas-phase calculations.

Excitonic states of the GaNQD were constructed from a basis comprising the 17 lowest-energy electron states and the 57 lowest-energy hole states. This choice ensures that electron and hole manifolds span comparable energy windows, accounting for the difference in their effective masses (see Table 3.1).

Hybrid excitonic calculations were performed by coupling the molecular and nanoparticle excitations within the HyCI framework. The minimum QD radius considered for the hybrid system, $R_{\mathrm{QD}} = 2.2$ nm, ensures that the size ratio between the nanoparticle and the porphine molecule remains sufficiently large. Together with the molecule–QD separation, this justifies the use of the dipole–field approximation for the molecule–nanoparticle interaction (see Section 2.1.3.2).

Molecular orientation angles between 0° and 90° with respect to the QD spin-up z axis were explored to probe the angular dependence of excitonic coupling. In addition, center-to-center distances $|\mathbf{R}|$ between porphine and the GaNQD were varied by fixing the QD radius and systematically changing the separation between the H_2P center of mass and the QD surface.

The HyCI basis was constructed using the complete set of multiparticle (MP) states of the nanoparticle and the 37 molecular excited states lying within the relevant resonance window. Numerical convergence of hybrid excitonic energies was explicitly assessed at resonance. Basis-set convergence was analyzed by disallowing all coupling matrix elements (both diagonal and off-diagonal) involving states with energies above a specified cutoff. Independently, multipole convergence was examined by suppressing all contributions to intraband and interband electric fields beyond a given maximum multipole order, while preserving the same spherical selection rules.

3.3 Isolated-fragment excitations

With the computational framework and numerical parameters specified, we now address the electronic-structure properties of the isolated fragments. We first analyze the excitation spectrum of porphine, identifying the optically active states relevant for hybridization, and then examine the excitonic structure of the GaN quantum dot, which together define the energetic conditions required for the formation of hybrid excitonic states.

3.3.1 Porphine: spectrum and optically active states

Figure 3.1 shows molecular-state energies E^M of H_2P as a function of the electronic state index α, together with their oscillator strengths $I_\alpha = \frac{2}{3}(E^M_\alpha - E^M_0)|d^M_{0\alpha}|^2$ relative to the maximum transition. Only the ground and first 20 excited states are shown for clarity. The spectrum exhibits the characteristic features of free-base porphyrins, with a set of low-lying states in the visible region followed by a group of intense ultraviolet transitions.

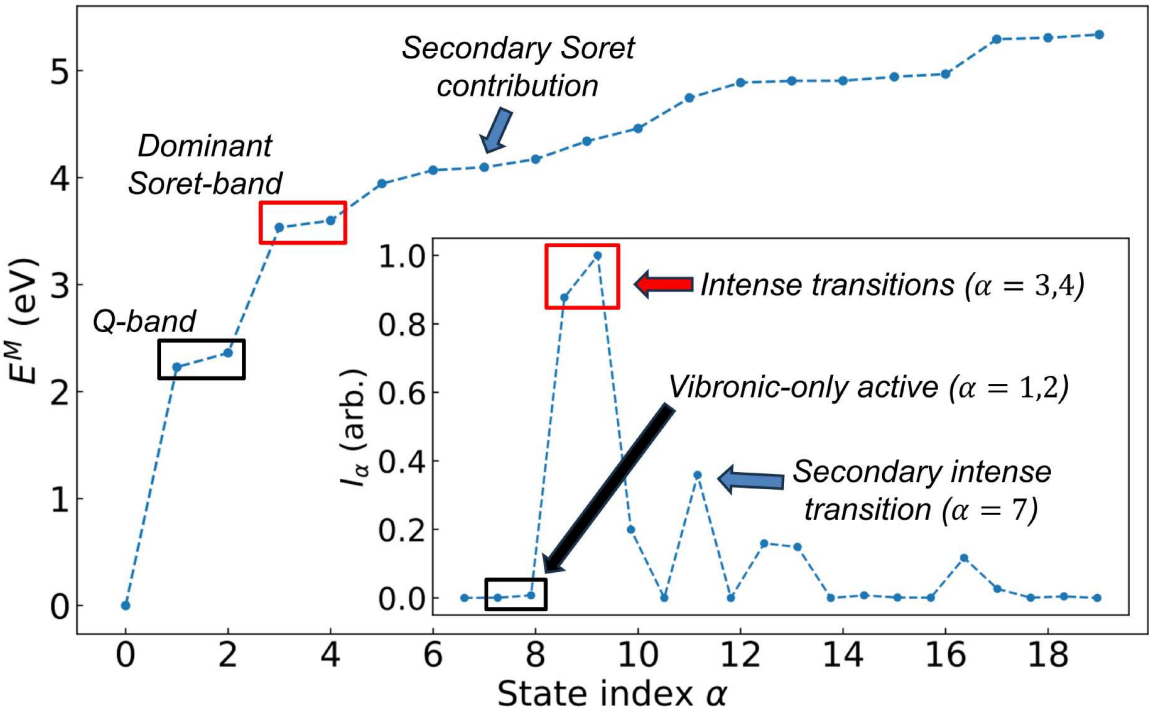

Figure 3.1: Energies and relative oscillator strengths of isolated H_2P as a function of the electronic state index α. The lowest states form the weakly allowed Q-band in the visible, while higher-energy UV states correspond to the dominant Soret band. The inset shows the associated transition intensities, highlighting strongly allowed transitions ($\alpha = 3, 4$), vibronically active Q-band states ($\alpha = 1, 2$), and secondary weaker contributions at higher energies.

The two lowest excited states ($\alpha = 1, 2$) correspond to the Q-band and are almost dark, owing to symmetry-induced cancellation of transition dipoles. Their weak experimental intensity arises predominantly from vibronic coupling, which cannot be explicitly captured within the present purely electronic description. For this reason, these states are not the primary target for resonance in the hybrid system. Instead, we focus on the strongly optically active Soret-band states ($\alpha = 3, 4$), which carry the dominant oscillator strength and therefore provide the most effective channel for excitonic hybridization with quantum-dot excitons.

The overall excitation spectrum of H_2P obtained here is in good agreement with previous theoretical studies based on TDDFT and other electronic-structure methods, [174] reproducing the characteristic separation between Q and Soret bands and the dominance of the latter in terms of oscillator strength. As commonly reported in vacuum calculations, the computed excitation energies exhibit a systematic blue shift with respect to experimental absorption spectra. This shift can be attributed to the absence of environmental screening and vibronic

effects. Since the present study is concerned with relative energy alignment and resonance conditions rather than absolute excitation energies, this systematic offset does not affect the physical interpretation of hybrid excitonic coupling.

The two intense ultraviolet transitions that dominate the Soret band correspond to the third and fourth excited electronic states of H_2P, hereafter denoted as M_3 and M_4, with excitation energies of approximately 3.53 eV and 3.60 eV, respectively. These states provide the primary molecular channels for resonant excitonic coupling with QD excitons. In the following, we consistently refer to these Soret-band states using the labels M_3 and M_4.

3.3.2 GaN quantum dot: excitonic energies and transition fields

Figure 3.2 reports the excitonic energies E^{NP} of the GaN quantum dot as a function of the dot radius R_{QD}. Only the low-lying states in the range of 2.2 nm to 3.0 nm are shown for clarity. As the QD size decreases, all low-energy excitonic states undergo a systematic blueshift relative to the bulk gap, reflecting enhanced quantum confinement in the nanoparticle. This pronounced size dependence provides a direct means of tuning the nanoparticle excitonic spectrum into resonance with selected molecular excitations.

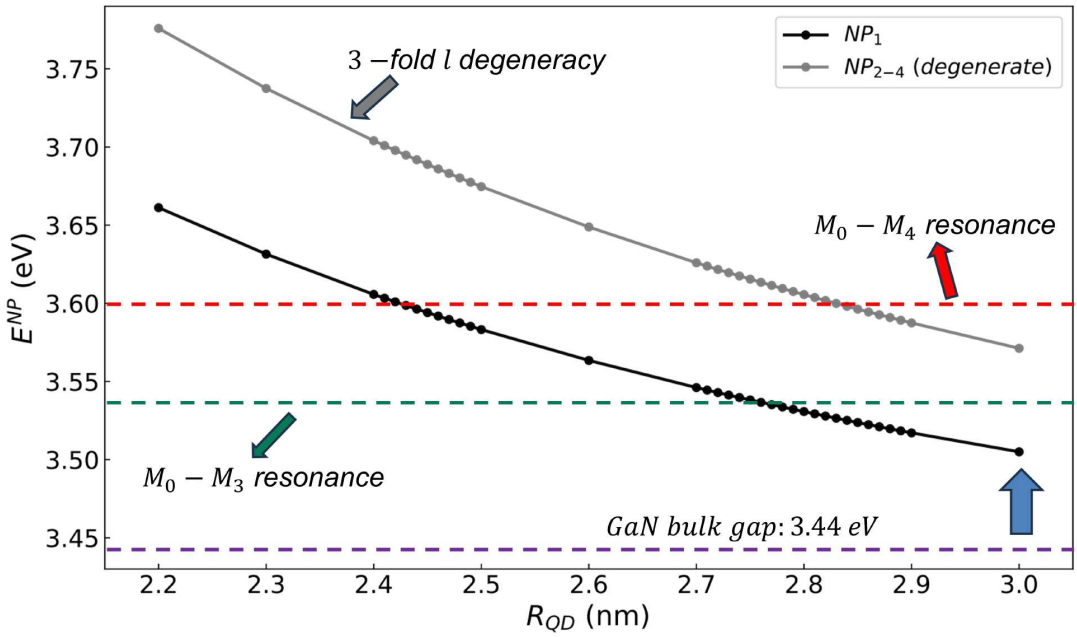

Figure 3.2: Lowest excitonic energies of GaNQD as a function of the dot radius R_{QD}. The lowest nondegenerate state (NP_1) and the threefold degenerate manifold (NP_{2-4}) show a systematic blueshift from the bulk gap (violet line) with decreasing size due to quantum confinement (blue arrow). Horizontal green and red dashed lines indicate reference molecular excitation energies and the GaN bulk band gap, highlighting size-dependent resonance conditions between molecular and quantum-dot states. The spin degeneracy of each state is not shown for clarity.

Two main groups of nanoparticle excitations can be identified in this window. The lowest exciton, labeled NP_1, is nondegenerate and optically bright, with an *interband* excitonic dipole of 10.9 a.u. This state is dominated by contributions from the ground SP electron and hole levels. It also defines the effective optical gap of the GaNQD at a given radius R_{QD}, thereby

setting the lower bound of the excitonic spectrum that can actively participate in resonant coupling with molecular excitations.

At slightly higher energies, a threefold-degenerate manifold of optically-dark states (NP_{2-4}) appears. This grouping reflects the underlying SP shell structure of the QD and the associated angular-momentum multiplicities, corresponding primarily to configurations involving the lowest electron state and the three $\ell = 1$ heavy-hole states. In addition, all NP_{1-4} states are intrinsically twofold degenerate due to spin (see subsection 2.1.2.2), although this degeneracy is not shown explicitly in Fig. 3.2 for clarity.

Green and red dashed lines in Fig. 3.2 indicate the energies of the H_2P states M_3 and M_4, located at approximately 3.53 eV and 3.60 eV, respectively. The radii at which NP_1 or the NP_{2-4} manifold approach these molecular energies define the resonance window most relevant for strong excitonic hybridization. In particular, resonances occur at $R_{QD} \approx 2.43$ nm for the M_4–NP_1 alignment, $R_{QD} \approx 2.77$ nm for the M_3–NP_1 resonance, and $R_{QD} \approx 2.84$ nm when the M_4 state aligns with the NP_{2-4} manifold.

Energetic tuning defines the resonance condition between molecular and nanoparticle excitations, but the resulting coupling strength is additionally governed by the magnitude of the excitonic electric field. This quantity also varies systematically with QD size, as represented in Fig. 3.3. On a log–log scale, this figure reports the magnitude of the *interband* electric field $|\mathbf{E}^{NP}_{0\nu}|$ associated with the spin-up excitonic states of the nanoparticle NP^{+}_{1-4} (identified by the upper index +, as defined in subsection 2.1.2.2). The field is evaluated near the QD spin-up zenith, with the observation point defined as $\mathbf{R} = (0, 0, R_{QD} + 0.70)$ nm. In this construction, varying the QD radius effectively varies the field evaluation coordinate while preserving a constant reference distance from the QD surface.

It is worth noting that, while the NP_{2-4} manifold is optically dark, these excitations still generate a finite and relevant transition field in the vicinity of the QD due to higher multipole contributions. Moreover, the extracted power-law behavior for all fields deviates from the $|\mathbf{R}|^{-n}$ scaling characteristic of a dipole ($n = 3$) or quadrupole ($n = 4$). An analogous behavior is also obtained for the corresponding spin-down channel, which is not shown explicitly for clarity.

Importantly, this deviation reflects the quantum-confined and Coulomb-correlated nature of the excitonic polarization in the QD. As the radius is varied, confinement and Coulomb interaction modifies both the spatial extent of the electron–hole pairs and its internal charge redistribution, resulting in a net near field whose distance dependence differs from that of a dipolar or quadrupolar source.

Because the molecule–nanoparticle interaction in Eq. (2.28) depends linearly on the electric field, the non-trivial field behavior highlighted in Fig. 3.3 provides an additional and independent handle to control the coupling strength beyond simple energetic resonance conditions.

3.4 Porphine + GaN quantum dot: avoided crossings and hybridization

Before analyzing the excitonic coupling itself, we examined the relative orientation of the molecular transition dipoles and the QD interband electric fields. The $M_0 \to M_4$ transition dipole is orthogonal to the $M_0 \to M_3$ dipole. In the QD, the spin-up interband fields are parallel to their spin-down counterparts for all transitions except NP_1, for which the two spin channels are

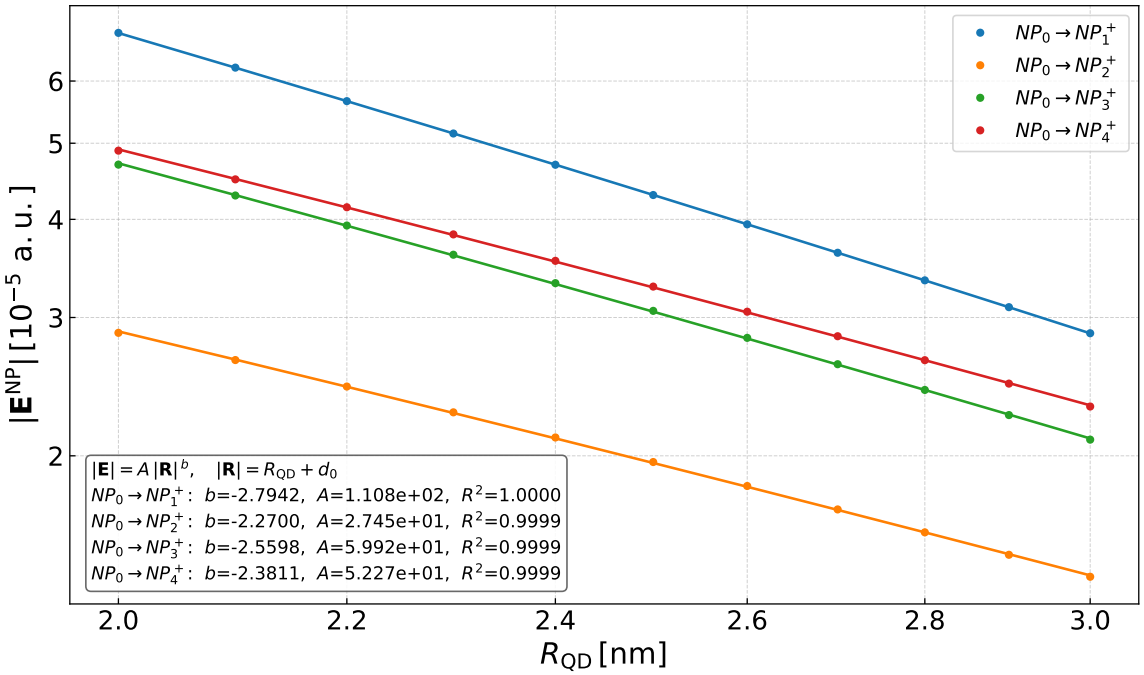

Figure 3.3: Log–log scaling of the magnitude of the *interband* electric field $|\mathbf{E}^{\mathrm{NP}}_{0\nu}|$ associated with the lowest spin-up transitions in GaNQD as a function of the dot radius R_{QD}. The field is evaluated at the QD spin-up zenith, with the observation point defined as $\mathbf{R} = (0, 0, R_{\mathrm{QD}} + d_0)$, such that varying R_{QD} effectively varies the field evaluation coordinate while preserving a fixed surface separation $d_0 = 0.70$ nm. Solid lines correspond to power-law fits highlighting a systematic deviation from the $|\mathbf{R}|^{-3}$ behavior expected for the near field of a point dipole. This deviation reflects the intrinsically non-trivial character of the excitonic near field arising from the interplay between quantum confinement and Coulomb interaction within the QD.

mutually orthogonal. Moreover, the $NP_0 \to NP_4$ transitions (for both spin channels) are orthogonal to those associated with NP_2 and NP_3, while being parallel to the spin-up component of NP_1.

Exploiting this rigid relative orientation, and unless otherwise stated, the molecular reference frame was chosen such that the $M_0 \to M_4$ transition dipole aligns with the laboratory z axis. This direction coincides with the spin-up interband field of the $NP_0 \to NP_1$ transition and, consequently, also with both spin channels of the $NP_0 \to NP_4$ transition, while remaining orthogonal to all other QD interband fields considered here. The same rotation was applied consistently to all molecular dipoles. As a result, the $M_0 \to M_3$ molecular dipole is orthogonal to the QD spin-up field of NP_1 and to both spin channels of NP_4, while being neither parallel nor orthogonal to the remaining interband transition fields, including the spin-down component of NP_1.

In this work, we restrict the analysis to the NP_1 and NP_4 interband transitions, since their resonances with M_3 and M_4 fall within the selected QD radius range of 2.2-3.0 nm. The resulting fixed geometry and the relative orientation of the molecular transition dipoles and QD interband electric fields are summarized schematically in Fig. 3.4.

Within the dipole–field approximation, the coupling matrix elements scale linearly with

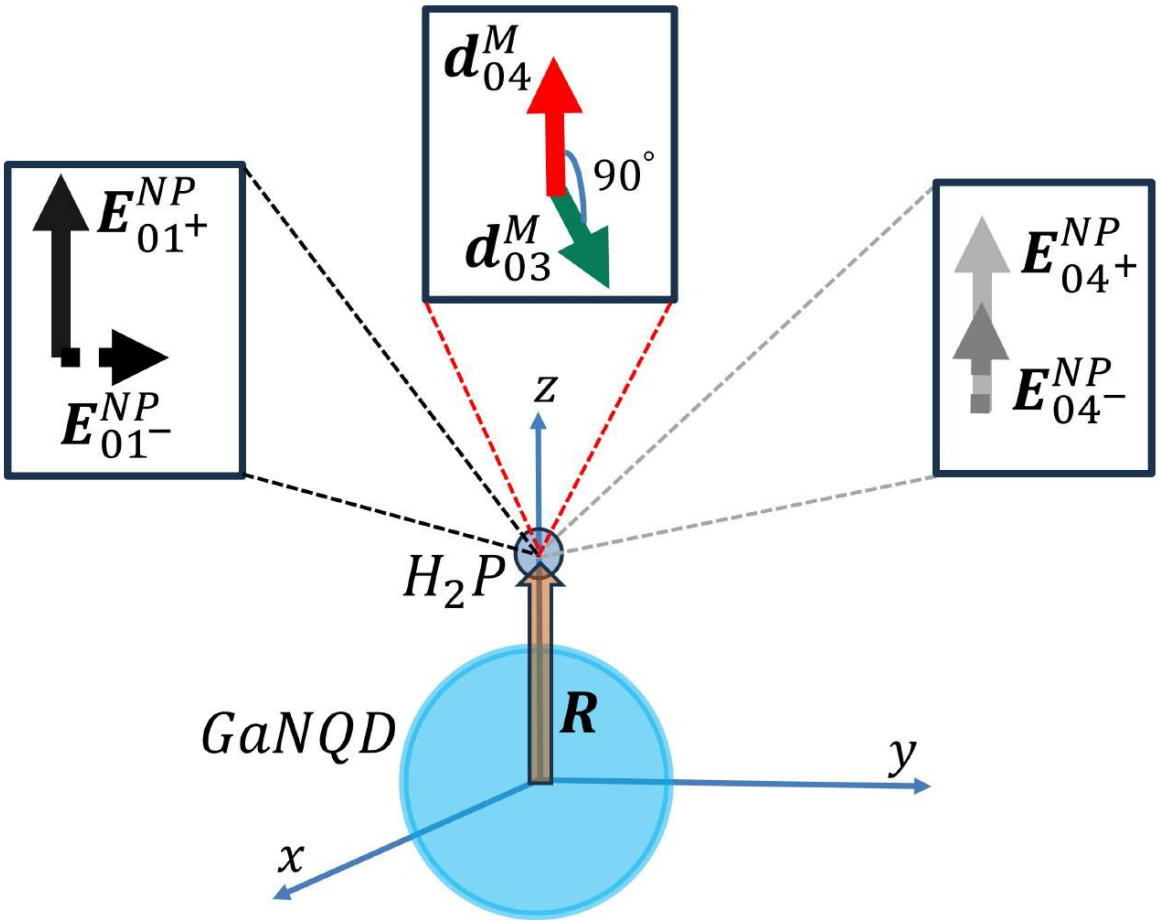

Figure 3.4: Schematic representation of the fixed H_2P–GaNQD geometry and the relative orientation of the molecular transition dipoles and QD interband electric fields. The molecule is placed on the QD zenith axis at $\mathbf{R} = (0, 0, R_{\mathrm{QD}} + d_0)$, with $d_0 = 0.70$ nm. The top inset shows the molecular transition dipoles $\mathbf{d}_{04}^{M}$ (red) and $\mathbf{d}_{03}^{M}$ (green). The left inset displays the interband electric fields associated with the NP_1 transition, $\mathbf{E}_{01+}^{\mathrm{NP}}$ and $\mathbf{E}_{01-}^{\mathrm{NP}}$ (black), while the right inset shows the NP_4 transition, $\mathbf{E}_{04+}^{\mathrm{NP}}$ and $\mathbf{E}_{04-}^{\mathrm{NP}}$ (gray). The magnitudes of the electric fields and molecular dipoles are each drawn to scale, but not relative to one another.

the magnitude of the QD electric field evaluated at the molecular position, such that their dependence on R_{QD} follows the same power-law behavior previously identified for the excitonic near field in Section 3.3.2. This size-dependent trend is simply multiplied by a constant prefactor set by the molecular dipole modulus $|\mathbf{d}_{\alpha\beta}^{M}|$ and by the geometric factor $\cos\phi$, where ϕ denotes the angle between the molecular dipole and the local QD field.

As a result, once the molecular orientation is fixed, variations in the coupling strength across the explored QD size range are governed almost entirely by the intrinsic scaling of the QD excitonic field, while the molecular properties enter only as a rigid, state-specific amplitude modulation. In particular, for the molecular geometry defined above, all dipole-field couplings between ground-to-excited transitions of H_2P and QD interband transitions vanish identically, with the exception of the following four cases:

- $M_0 \to M_4$ coupled to $NP_0 \to NP_1^{+}$ (spin-up): 4.10 meV at $R_{\mathrm{QD}} = 2.43$ nm;

- $M_0 \to M_3$ coupled to $NP_0 \to NP_1^-$ (spin-down): 0.998 meV at $R_{\mathrm{QD}} = 2.77$ nm.
- $M_0 \to M_4$ coupled to $NP_0 \to NP_4^+$ (spin-up): 2.31 meV at $R_{\mathrm{QD}} = 2.84$ nm;
- $M_0 \to M_4$ coupled to $NP_0 \to NP_4^-$ (spin-down): 0.910 meV at $R_{\mathrm{QD}} = 2.84$ nm;

To visualize the effect of the excitonic coupling on the hybrid spectrum, we represent the energies of selected hybrid states as a function of the QD radius in the form of a pseudo potential energy surface (PES), shown in Fig. 3.5. The term "pseudo" emphasizes that R_{QD} is not a true dynamical degree of freedom, but an external structural parameter that tunes the QD excitonic spectrum and the molecule–QD resonance conditions. This representation nevertheless provides a transparent way to track the evolution of hybrid energies and compositions as excitonic levels are brought into and out of resonance.

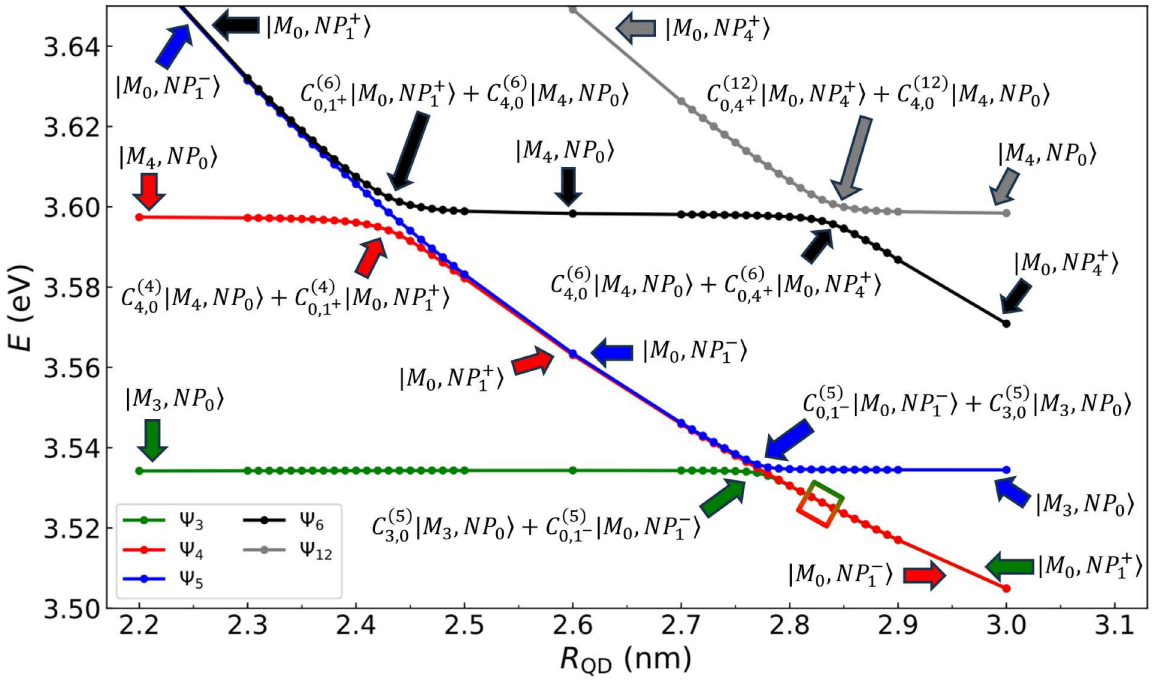

Figure 3.5: Pseudo PESs of selected hybrid excitonic states as a function of the quantum dot radius R_{QD}. The curves illustrate avoided crossings arising from the coupling between molecular excitations of H_2P and size-tunable GaN quantum-dot states. The dominant molecular or nanoparticle character of each hybrid state is indicated, showing how resonance leads to strong state mixing and energy-level repulsion. The highlighted square indicates a lower-scale avoided crossing between states Ψ_3 and Ψ_4 (see Fig. 3.6), associated with a secondary exchange of molecular and nanoparticle character.

For clarity, only the hybrid states Ψ_3, Ψ_4, Ψ_5, Ψ_6, and Ψ_{12} are shown, as these are directly involved in the hybridization near the relevant resonant radii. Away from resonance, the overall energy layout closely resembles that of the isolated QD excitonic spectrum (see subsection 3.3.2), with the molecular states appearing as nearly flat lines. In this regime, the hybrid energies experience only shifts arising from the cumulative effect of many diagonal and off-diagonal coupling terms that are out of resonance.

As R_{QD} approaches a resonance condition, pairs of states with comparable energies undergo avoided crossings, signaling the onset of excitonic hybridization. In these regions, the hybrid eigenstates are well described as coherent superpositions of molecular and nanoparticle product states, with the corresponding coefficients C_{ip}^{ν} evolving rapidly as a function of the QD radius. The magnitude of the level repulsion at each avoided crossing reflects the strength of the underlying dipole–field coupling identified earlier.

Specifically, the hybrid states Ψ_4 and Ψ_6 exhibit a pronounced avoided crossing near $R_{\mathrm{QD}} \simeq 2.43$ nm, associated with the resonance between the M_4 molecular excitation and the NP_1^+ interband transition. Across this region, the character of the two states is exchanged: the predominantly molecular state acquires increasing nanoparticle weight, while the initially nanoparticle-like state becomes molecular in nature. An analysis of the HyCI eigenvectors reveals that, in the vicinity of the avoided crossing, the hybrid states Ψ_4 and Ψ_6 are almost entirely composed of the two product configurations associated with the molecular and QD resonant excitations. This demonstrates that the avoided crossing corresponds to an exceptionally clean two-level hybridization. Importantly, such a reduction could not be established *a priori* in a dense nanohybrid spectrum, but is revealed only through access to the full HyCI eigenvectors.

A similar behavior occurs near $R_{\mathrm{QD}} \simeq 2.77$ nm, where the resonance between the M_3 molecular excitation and the NP_1^- interband transition produces a comparatively small avoided crossing between the hybrid states Ψ_3 and Ψ_5. The reduced level repulsion reflects the weaker dipole-field coupling strength and is nonetheless accompanied by a clear exchange of molecular and nanoparticle character.

At larger radii, around $R_{\mathrm{QD}} \simeq 2.84$ nm, the interaction between the molecular excitation $M_0 \rightarrow M_4$ and the NP_4^+ and NP_4^- interband transitions gives rise to an additional avoided crossing involving the hybrid states Ψ_6 and Ψ_{12}. This crossing originates from the coupling within an effective threefold near-degeneracy between the molecular state and the two QD spin channels. Because the coupling to the spin-up channel is approximately 2.5 times stronger than that to the spin-down channel, the nanoparticle component of the resulting hybrid states is dominated by spin-up character. The spin-down contribution at the resonance radius, while non-negligible, accounts only for 6.7% and 6.4% of the Ψ_6 and Ψ_{12} character, respectively, and therefore is not shown explicitly in Fig. 3.5 for clarity.

Overall, this sequence of avoided crossings and accompanying exchanges of molecular and nanoparticle character highlights how the hybrid spectrum is governed by the interplay between size-tunable energetic resonance and dipole–field–mediated coupling.

To further elucidate the nature of the avoided crossings discussed above, Fig. 3.6 reports the evolution of the transition dipole strengths associated with the same set of hybrid states as a function of the QD radius. This figure provides a complementary perspective to the pseudo-PES by directly tracking how the molecular and nanoparticle contributions to each hybrid state evolve across the resonant regions. In particular, the pronounced redistribution of dipole strength observed near the avoided crossings offers a direct signature of the exchange of character between molecular- and QD-dominated states.

In the vicinity of the resonances involving NP_1^+ and NP_1^-, at 2.43 nm and 2.77 nm respectively, the molecular and nanoparticle dipole strengths exhibit a clear anti-correlated behavior: as one hybrid state loses molecular dipole intensity, the other gains it, and vice versa. This behavior mirrors the level repulsion observed in Fig. 3.5 and reflects the coherent mixing of molecular and nanoparticle product states. Away from resonance, the dipole strengths remain

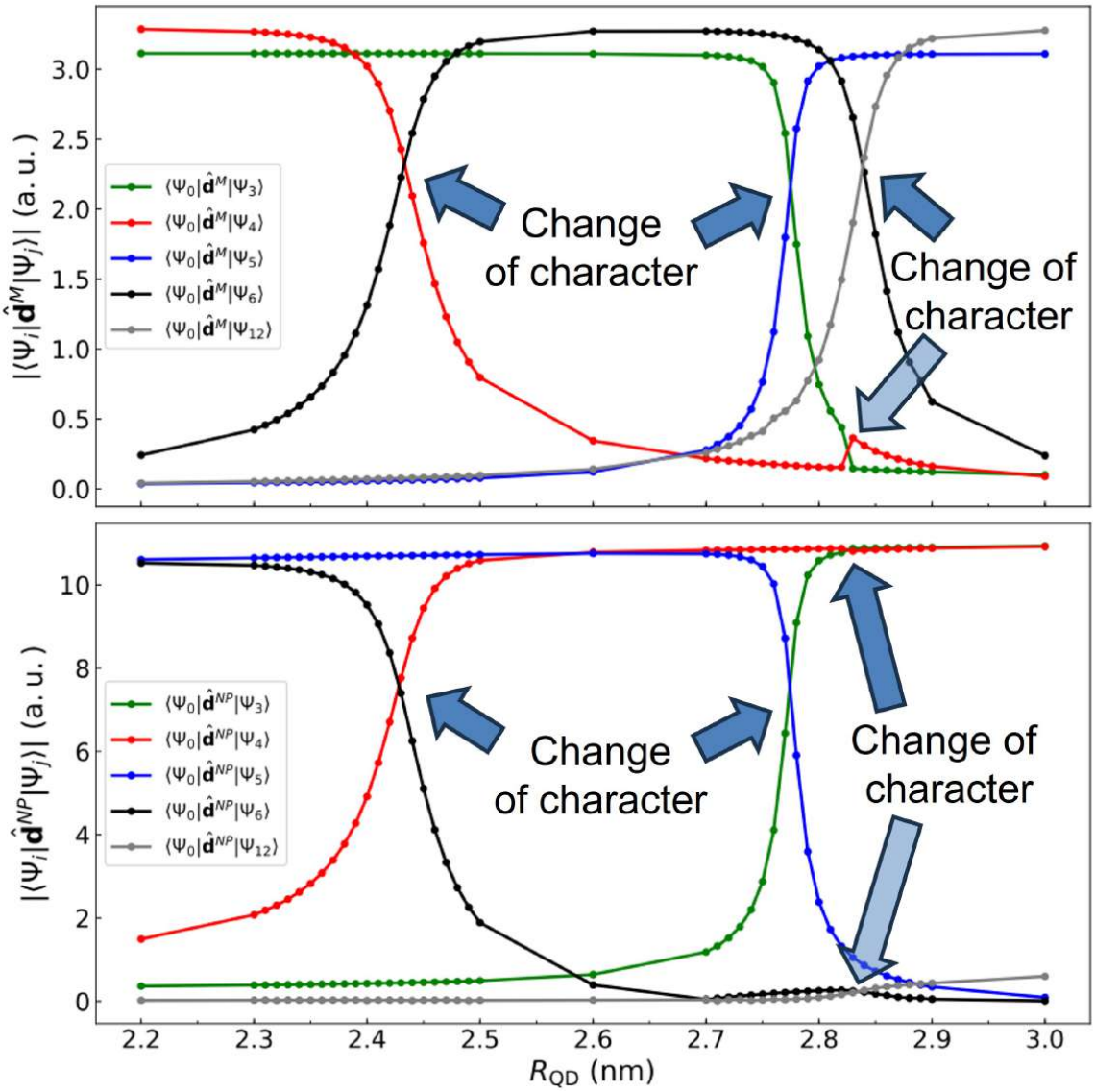

Figure 3.6: Strength of ground-transition dipole moments of selected hybrid excitonic states as a function of the quantum dot radius R_{QD}. The upper panel shows dipole contributions associated with molecular excitations, while the lower panel corresponds to nanoparticle-related transitions. The sharp variations near resonance indicate a pronounced change of character, reflecting the exchange of molecular and quantum-dot contributions across avoided crossings.

nearly constant, consistent with the weak-hybridization regime in which the states retain a predominantly molecular or QD character.

At $R_{\mathrm{QD}} = 2.84$ nm, the avoided crossing involving NP_4^+, NP_4^-, and M_4 manifests itself more weakly in the nanoparticle dipole analysis. The lower-scale avoided crossing observed between the green and red curves corresponds to their very small mutual coupling. By contrast, the avoided crossing between the black and gray curves in the nanoparticle sector is contrasted by a comparatively modest redistribution of dipole strength in the molecular case. This behavior reflects the fact that the NP states primarily involved in this resonance are optically dark within the dipole approximation, resulting in a reduced effective contribution (see Eq. (2.44))

and, consequently, a weaker hybridization signature in the dipole strength.

From a methodological perspective, these results illustrate a key strength of the HyCI approach for nanohybrids. The avoided crossings, state mixing, and redistribution of dipole strength emerge from a single Hamiltonian in which molecular and nanoparticle excitations, including different spin channels and optically dark states, are treated on equal footing. Importantly, no a *priori* restriction to a small set of resonant states is imposed: both dominant and subdominant interaction channels are included consistently, allowing their relative importance to be assessed from the full hybrid spectrum.

3.5 Scaling laws at resonance

Having established how energetic tuning and dipole–field coupling govern the occurrence of avoided crossings and hybridization, we now turn to a complementary aspect of the problem: the scaling of the hybrid coupling strength at resonance. We analyze how the magnitude of the hybrid-state splitting depends on geometric parameters at fixed resonance, focusing in particular on the roles of molecular orientation and molecular distance from the QD surface.

3.5.1 Orientation angle

Figure 3.7 illustrates the angular dependence of the hybrid-state energy gap $\Delta_{\text{gap}} = \left|E_{\Psi_6} - E_{\Psi_4}\right|$ at the resonance radius $R_{\text{QD}} = 2.43$ nm. The gap is evaluated as a function of the relative orientation angle ϕ between the molecular $M_0 \to M_4$ transition dipole and the resonant $NP_0 \to NP_1^+$ interband QD field. This dependence is probed by rigidly rotating all molecular dipoles by an angle ϕ with respect to the QD zenith axis, from an initial alignment with the $NP_0 \to NP_1^+$ field to a final alignment with the $NP_0 \to NP_1^-$ interband QD field along the y axis, while keeping all other parameters fixed.

The numerical data are fitted using the exact eigenvalue splitting of a reduced three-level Hamiltonian comprising the molecular excitation and the two degenerate QD interband spin channels. In the basis $\{\,|M_4\rangle, |NP_1^+\rangle, |NP_1^-\rangle\,\}$, the effective Hamiltonian can be written as $H_{\text{eff}} = \begin{pmatrix} \Delta_0 & V_+\cos\phi & V_-\sin\phi \\ V_+\cos\phi & 0 & 0 \\ V_-\sin\phi & 0 & 0 \end{pmatrix}$, where V_+ and V_- denote the effective couplings between the molecular transition and the spin-up and spin-down components of the resonant QD excitation, respectively, while Δ_0 represents an effective detuning that incorporates both diagonal couplings and smooth renormalizations arising from off-resonant interactions. The resulting eigenvalue splitting yields $\Delta_{\text{gap}}(\phi) = \sqrt{\Delta_0^2 + 4\left(V_+^2\cos^2\phi + V_-^2\sin^2\phi\right)}$. For the present geometry, the fit yields $V_+ = 3.72$ meV and $V_- = 0.324$ meV, together with an effective detuning $\Delta_0 = 3.45$ meV.

The fitted curve reproduces the numerical results essentially exactly, and reveals a clear and symmetric angular dependence of the gap. The splitting is maximal when the molecular transition dipole is aligned with the dominant QD field component and decreases continuously as the dipole is rotated, reaching its minimum when the dipole becomes orthogonal to that field. This behavior reflects the combined angular projections of the molecular dipole onto the two orthogonal QD spin-field components.

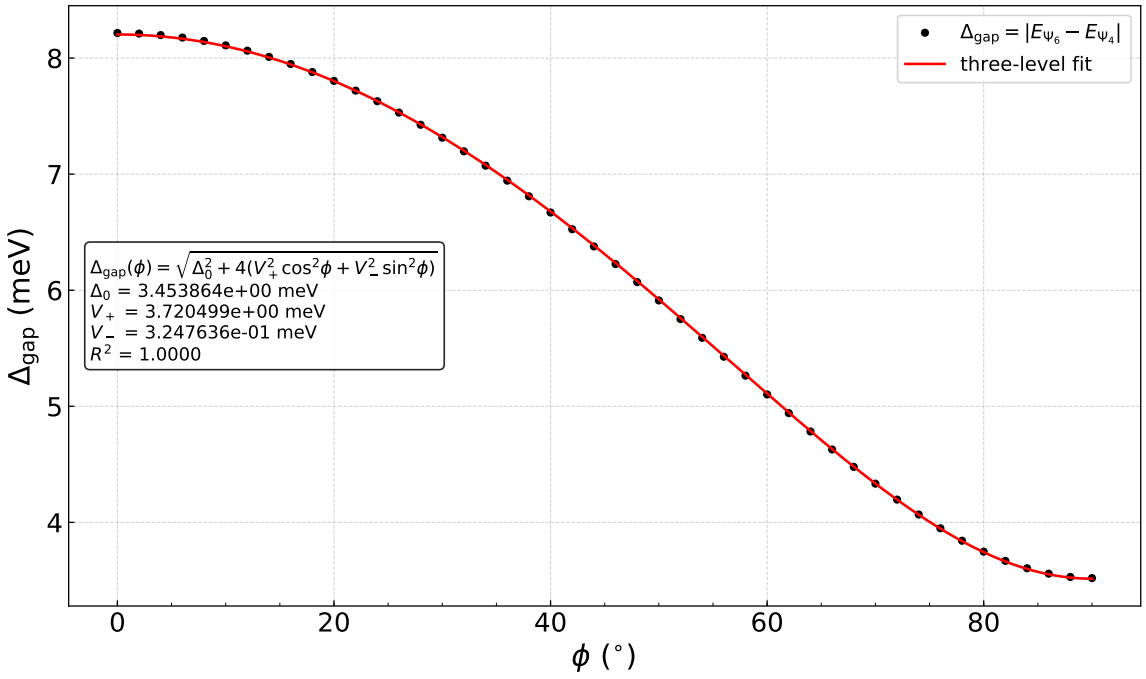

Figure 3.7: Angular dependence of the hybrid-state energy gap $\Delta_{\mathrm{gap}} = \left|E_{\Psi_6} - E_{\Psi_4}\right|$ at the resonance radius $R_{\mathrm{QD}} = 2.43$ nm, shown as a function of the relative orientation angle ϕ between the molecular $M_0 \to M_4$ transition dipole and the resonant $NP_0 \to NP_1^+$ interband QD field. Symbols denote HyCI results, while the solid line corresponds to a fit using the exact analytical expression for a reduced three-level Hamiltonian with degenerate QD spin channels, $\Delta_{\mathrm{gap}}(\phi) = \sqrt{\Delta_0^2 + 4\left(V_+^2 \cos^2\phi + V_-^2 \sin^2\phi\right)}$. The excellent agreement demonstrates that the angular modulation of the avoided crossing is governed by a small set of resonant excitonic couplings, while the influence of the remaining dense nanohybrid spectrum enters through smooth renormalization of effective parameters captured by the HyCI treatment.

Although the HyCI eigenstates involved in the avoided crossing are almost entirely composed of the resonant product configurations, their energies are not determined solely by the corresponding bare dipole-field matrix elements. Instead, the fitted parameters V_+ and V_- represent effective couplings emerging from the full HyCI Hamiltonian. In particular, both couplings are reduced with respect to their maximum bare values, 4.10 meV for the spin-up channel and 0.60 meV for the spin-down channel, reflecting renormalization effects induced by off-resonant molecular and nanoparticle configurations explicitly included in the HyCI basis.

The excellent agreement between the HyCI results and the three-level analytical expression confirms that, at resonance, the angular modulation of the avoided crossing is governed by the set of resonant excitonic couplings, while the influence of the remaining nanohybrid spectrum enters through smooth renormalization of the effective parameters. This conclusion could not be established *a priori* in such a dense hybrid spectrum and relies on access to the full HyCI eigenstates.

Overall, the orientation angle ϕ provides a purely geometric means of controlling the strength of excitonic hybridization at fixed resonance conditions. By rotating the molecular transition dipole with respect to the anisotropic QD excitonic field, the effective coupling strength —and

hence the magnitude of the avoided crossing— can be continuously tuned without altering the molecular identity, QD size, or energetic alignment.

3.5.2 M-NP distance

Figure 3.8 shows the dependence of the hybrid-state energy splitting $\Delta_{\mathrm{gap}} = \left|E_{\Psi_6} - E_{\Psi_4}\right|$ on the molecular separation from the QD surface d for the hybrid-state pair Ψ_4 and Ψ_6 at the resonance radius $R_{\mathrm{QD}} = 2.43$ nm. The molecular orientation is fixed to the configuration used to define the avoided crossing discussed in Section 3.4, with the $M_0 \rightarrow M_4$ transition dipole aligned along the QD zenith axis. The corresponding center-to-center separation is given by $|R| = R_{\mathrm{QD}} + d$.

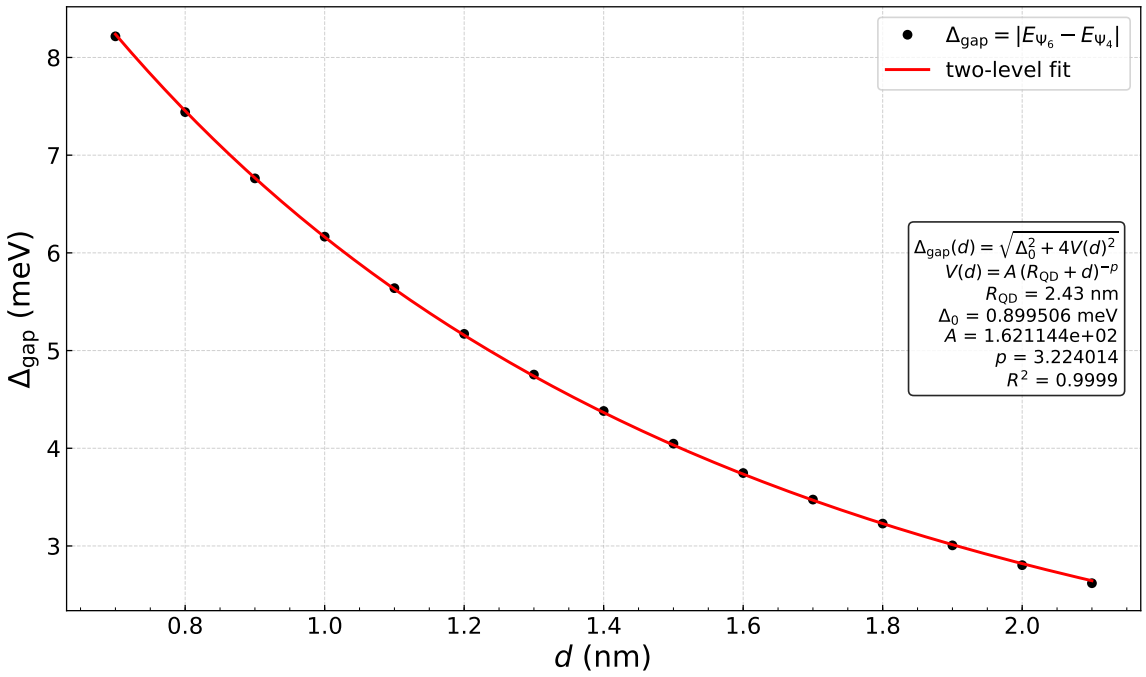

Figure 3.8: Dependence of the hybrid-state energy splitting $\Delta_{\mathrm{gap}} = \left|E_{\Psi_6} - E_{\Psi_4}\right|$ on the M–NP surface separation d for the resonant hybrid-state pair Ψ_4 and Ψ_6 at $R_{\mathrm{QD}} = 2.43$ nm and fixed molecular orientation. Symbols denote HyCI results, while the solid line is a fit to a two-level expression, $\Delta_{\mathrm{gap}}(d) = \sqrt{\Delta_0^2 + 4V(d)^2}$, with a distance-dependent coupling $V(d) = A\,(R_{\mathrm{QD}} + d)^{-p}$. The monotonic decay of the splitting and the extracted power-law exponent indicate that, at fixed QD size and resonant condition, the distance dependence of the hybrid gap is governed primarily by the spatial decay of a dipolar near field.

The numerical data are fitted using the exact eigenvalue splitting of a reduced two-level Hamiltonian involving the molecular excitation $|M_4\rangle$ and the bright QD excitonic state $|NP_1^+\rangle$. For this geometry, the $M_0 \rightarrow M_4$ transition dipole is orthogonal to the electric field associated with the NP_1^- interband transition, so that the corresponding spin channel does not participate in the hybridization. As a result, the effective Hamiltonian reduces to $H_{\mathrm{eff}} = \begin{pmatrix} \Delta_0 & V(d) \\ V(d) & 0 \end{pmatrix}$, where Δ_0 is an effective detuning incorporating diagonal and off-resonant renormalization ef-

fects. The effective coupling $V(d)$ is described by a power-law form $V(d) = A\,(R_{\mathrm{QD}} + d)^{-p}$. The corresponding eigenvalue splitting is therefore given by $\Delta_{\mathrm{gap}}(d) = \sqrt{\Delta_0^2 + 4V(d)^2}$.

As the molecule is progressively displaced away from the QD, the hybrid energy splitting decreases monotonically and follows a clear power-law behavior. To gain insight into this trend, we compare it with the spatial decay of the electric field associated with the resonant interband transition to the NP_1^+ state. As expected from its bright nature, this field exhibits a power-law scaling close to $d^{-3.09}$ (not shown for clarity). The close agreement between this exponent and $p \simeq 3.22$ indicates that the distance dependence of the hybrid splitting is largely governed by the spatial decay of the resonant NP_1^+ near field, while contributions from off-resonant couplings remain subleading and enter only as smooth renormalization corrections to the effective decay exponent.

In contrast to the size-scaling analysis discussed in Section 3.3.2, where varying the QD radius simultaneously modified the excitonic wave functions and their multipolar composition, the present analysis isolates the effect of distance by keeping the QD size fixed at its resonant value. In this sense, the M–NP separation d constitutes an independent geometric control parameter for the hybridization strength. At fixed QD size, molecular orientation, and resonance condition, varying the distance directly modulates the magnitude of the excitonic coupling through the spatial decay of the QD near field, thereby controlling the hybrid-state splitting. The distance dependence thus provides a tuning mechanism for excitonic hybridization that is complementary to the angular control discussed in subsection 3.5.1.

3.6 Energy convergence at resonance

To assess the residual error associated with basis truncation in the HyCI treatment at resonance, we analyze the convergence of selected hybrid energies with respect to two complementary criteria: (i) the truncation in angular momentum of the nanoparticle (NP) single-particle basis, which controls the multipolar content of the excitonic electric field entering the coupling and is characterized by the maximum multipole order $L_{\max}$, and (ii) the truncation of the coupled molecular-nanoparticle many-body Hilbert space, implemented through an energy cutoff E_{cut} in the HyCI basis.

In the calculations reported throughout this work, the NP single-particle space includes electron and hole states up to angular momentum $l = 3$. The analyses below provide an *a posteriori* validation that this choice, together with the adopted HyCI basis size, is sufficient to accurately describe excitonic hybridization at resonance.

3.6.1 HyCI basis set

The size of the HyCI many-body basis is controlled by an energy cutoff E_{cut}: a coupling channel is included only if *both* participating configurations lie below E_{cut}. Convergence is monitored through the coupling-induced energy shift $\Delta E_i(E_{\mathrm{cut}}) = E_i^{\mathrm{HyCI}}(E_{\mathrm{cut}}) - E_i^{\mathrm{NoCoupling}}$, where $E_i^{\mathrm{NoCoupling}}$ is obtained by switching off the interaction entirely. This definition isolates the contribution due to excitonic coupling and allows a direct estimate of the truncation error from the difference between the extrapolated limit and the value obtained at the largest cutoff.

Figure 3.9 shows the convergence of ΔE as a function of E_{cut} for representative hybrid states at three resonance radii. The energy shifts vary smoothly and approach a well-defined

asymptotic limit in all cases, indicating that the dominant coupling contributions are captured once a sufficiently large subset of the coupled M-NP Hilbert space is included. In particular, the complete set of MP states of the NP and the corresponding resonant M states used in previous calculations relate to the case $E_{\mathrm{cut}} = 6.40$ eV.

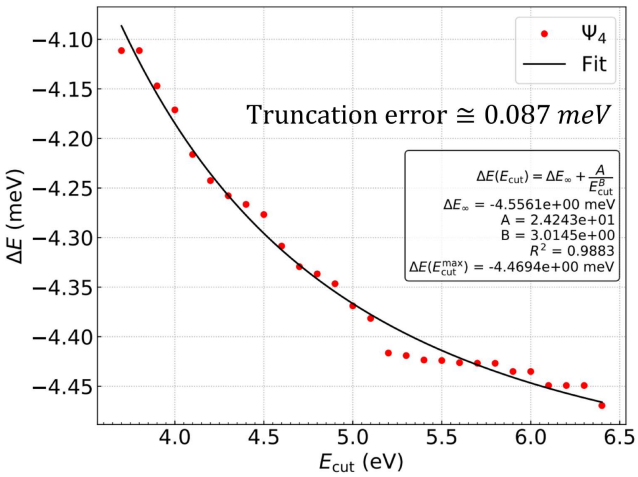

(a) $R_{\mathrm{QD}} = 2.43$ nm, Ψ_4.

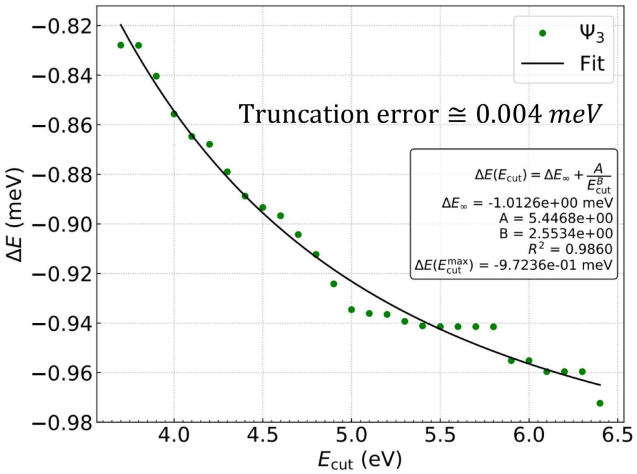

(b) $R_{\mathrm{QD}} = 2.77$ nm, Ψ_3.

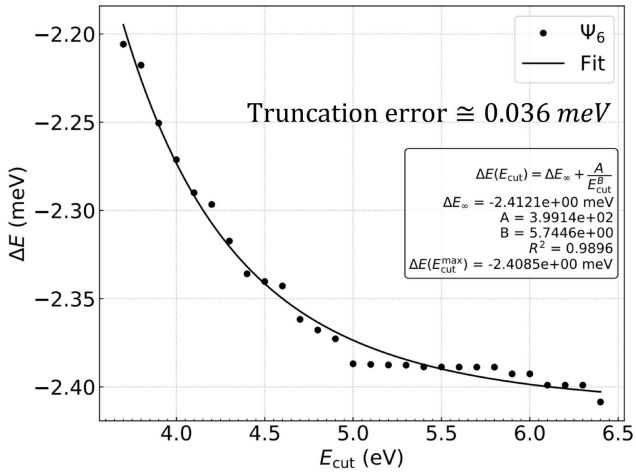

(c) $R_{\mathrm{QD}} = 2.84$ nm, Ψ_6.

Figure 3.9: Convergence of the coupling-induced energy shift ΔE with the basis-set cutoff E_{cut} at representative resonance radii. Symbols are computed values and solid lines are fits used to extrapolate to $E_{\mathrm{cut}} \to \infty$. The highlighted truncation error is estimated as $|\Delta E_\infty - \Delta E(E_{cut}^{max})|$. For each avoided crossing, only one branch is displayed because both hybridized partners show the same E_{cut} dependence and yield comparable errors.

The solid lines correspond to power-law fits, which provide a deliberately conservative description of the convergence behavior and avoid assuming an artificially rapid saturation. This choice allows for a robust extrapolation to the $E_{\mathrm{cut}} \to \infty$ limit and yields residual truncation errors typically below 0.1 meV, i.e., at least an order of magnitude smaller than the corresponding energy shifts. Only one branch of each avoided crossing is displayed, since both hybridized partners exhibit the same dependence on E_{cut} and yield comparable extrapolated errors.

These results demonstrate that the numerical uncertainty associated with truncation of the HyCI basis is well controlled and remains negligible compared to the energy scales of the avoided crossings discussed in this work.

3.6.2 Electric field multipoles

Figure 3.10 shows the dependence of the coupling-induced energy shift ΔE on the maximum multipole order $L_{\max}$ retained in the interaction, directly probing the angular-momentum content of the NP excitonic field required to converge the hybrid energies. Each panel corresponds to a different avoided crossing occurring at a distinct resonant QD radius, namely $R_{\mathrm{QD}} = 2.43$, 2.77, and 2.84 nm. In addition to the main panels, the insets report the incremental contribution of each individual multipole order to the total energy shift, providing a detailed view of the relative weight of the different angular-momentum channels.

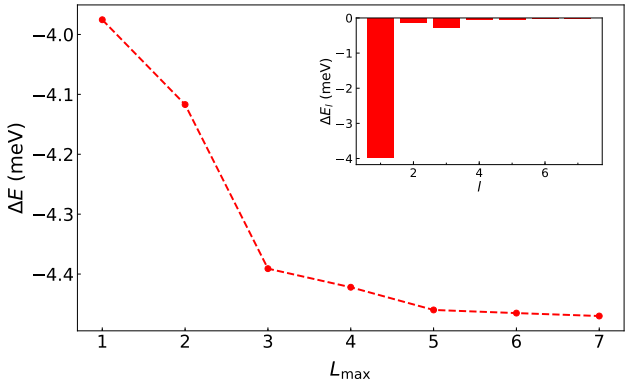

(a) $R_{\mathrm{QD}} = 2.43$ nm, Ψ_4.

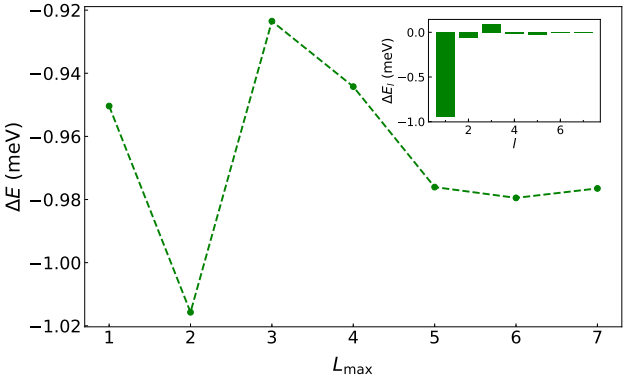

(b) $R_{\mathrm{QD}} = 2.77$ nm, Ψ_3.

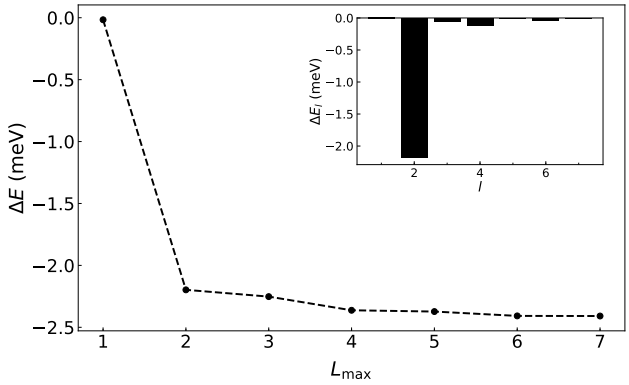

(c) $R_{\mathrm{QD}} = 2.84$ nm, Ψ_6.

Figure 3.10: Dependence of the shift ΔE on the maximum multipole order $L_{\max}$ included in the interaction. The curves quantify the multipolar content required to converge the coupling at resonance. Only one branch per avoided crossing is shown, since both partners exhibit the same $L_{\max}$ trend and comparable truncation errors. At $R_{\mathrm{QD}} = 2.84$ nm the higher-L contribution is enhanced because the mixing involves the spin-up NP_4 level, which is dipole-forbidden (dark), suppressing the dipolar channel.

The maximum multipole order retained in the calculations is $L_{\max} = 7$. This choice follows

directly from angular-momentum selection rules, according to which the highest allowed multipolar contribution scales as $l_e + l_h + 1$, together with the fact that the SP angular momenta of both electrons and holes are restricted to $l_e, l_h \leq 3$.

For the avoided crossing at $R_{\mathrm{QD}} = 2.43$ nm (Fig.3.10a), convergence is rapid and dominated by the lowest multipole orders. As shown by the insets, the dipolar ($l = 1$) contribution accounts for the largest fraction of the coupling-induced shift, while higher-order multipoles provide only minor corrections. This behavior reflects the predominantly dipolar character of the resonant NP excitonic field mediating the hybridization and confirms that truncation of the NP single-particle basis at $l = 3$ is sufficient in this case.

At $R_{\mathrm{QD}} = 2.77$ nm (Fig.3.10b), the overall convergence remains controlled but exhibits small oscillations as L_{max} is increased. These oscillations arise from partial cancellations between multipolar contributions of different order, as also reflected in the insets, and lead to a less smooth but still well-behaved convergence toward the asymptotic value.

At $R_{\mathrm{QD}} = 2.84$ nm (Fig.3.10c), the avoided crossing involves the spin-up NP_4 excitation, which is dipole-forbidden. As a result, the insets show a strongly suppressed dipolar contribution and a dominant quadrupolar component, while higher-order multipoles contribute only weakly. The apparent slower convergence with respect to L_{max} therefore reflects the change in the leading coupling channel rather than a proliferation of significant higher-order contributions. Once the dominant quadrupolar term is included, the cumulative energy shift converges systematically and the residual truncation error remains small.

Overall, the multipole analysis shows that excitonic hybridization at resonance is governed by a small number of low-order angular-momentum components of the NP excitonic field. While the dominant multipole order depends on the symmetry of the resonant excitation, higher-order multipoles beyond those allowed by selection rules contribute only weakly and enter as controlled corrections. Therefore, the results obtained with $L_{\mathrm{max}} = 7$ are considered numerically converged for this study.

3.7 Conclusions

In this chapter, the HyCI framework was applied to CPh-QD nanohybrids to achieve a detailed and controlled description of excitonic hybridization between localized molecular excitations and size-tunable nanoparticle excitons. Using $\mathrm{H_2P}$ coupled to a GaNQD as a prototypical system, we systematically analyzed how energetic resonance, geometrical parameters, and multipole structure cooperate to produce hybrid excitonic states.

Starting from the isolated fragments, we identified the optically active excitations of $\mathrm{H_2P}$ and the low-lying excitonic spectrum of GaNQDs as the key ingredients governing hybridization. The strong size dependence of the QD excitonic energies enables precise tuning into resonance with selected molecular transitions, providing a robust and experimentally relevant handle to induce excitonic coupling. Importantly, the associated nanoparticle excitonic electric fields were shown to deviate from simple classical near-field scaling, reflecting the quantum-confined and Coulomb-correlated nature of the excitonic polarization.

By explicitly coupling molecular and nanoparticle excitations within the HyCI Hamiltonian, we demonstrated the emergence of avoided crossings in the hybrid spectrum as a function of QD size. These avoided crossings correspond to genuine excitonic hybridization, characterized by coherent superpositions of molecular and nanoparticle product states and by a pronounced

exchange of state character across resonance. Analysis of the HyCI eigenvectors revealed that, despite the dense nanohybrid spectrum, several avoided crossings reduce effectively to clean two- or three-level hybridization problems dominated by a small number of resonant configurations. This reduction, however, is not imposed *a priori* but emerges naturally from the full many-body treatment.

The redistribution of transition dipole strength across the avoided crossings provided a complementary and physically transparent signature of hybridization. In particular, the anti-correlated evolution of molecular and nanoparticle dipole contributions directly tracks the exchange of character between hybrid states, while also highlighting the distinct behavior of optically bright and dark nanoparticle excitations. These results illustrate the importance of treating all excitations, including spin channels and dipole-forbidden states, on equal footing within the HyCI framework.

At fixed resonance, we further established that excitonic hybridization can be continuously tuned through purely geometric parameters. Rotation of the molecular transition dipole with respect to the anisotropic QD excitonic field modulates the hybrid-state splitting in a manner accurately captured by a reduced three-level model with effective couplings renormalized by off-resonant interactions. Similarly, variation of the M-NP separation provides a radial control mechanism governed by the spatial decay of the excitonic near field. Together, orientation and distance constitute independent and complementary geometric handles to regulate the strength of hybridization without altering the molecular identity or the nanoparticle size.

A dedicated convergence analysis demonstrated that the numerical results are robust with respect to both the size of the HyCI basis and the multipolar truncation of the nanoparticle electric field. Conservative power-law extrapolations of the basis-set cutoff yielded residual uncertainties well below the energy scales of the avoided crossings. The multipole analysis showed that hybridization at resonance is governed by a small number of low-order angular-momentum components of the excitonic field, with the dominant multipole determined by symmetry selection rules. Higher-order contributions enter only as controlled corrections, even in cases where the leading dipolar channel is suppressed.

Overall, this chapter establishes a coherent picture of excitonic hybridization in CPh-QD nanohybrids. The HyCI framework emerges as a powerful and flexible tool capable of capturing resonance effects, state mixing, and geometric control mechanisms within a single, non-perturbative Hamiltonian. Beyond providing quantitative insight into a specific H_2P–GaNQD system, the concepts developed here —energetic tuning, field-mediated coupling, and geometric control— form a general foundation for understanding and engineering excitonic hybrid states in more complex nanohybrid architectures.

These results set the stage for Chapter 4, where similar hybrid excitonic mechanisms are shown to influence photochemical pathways in PhS–QD systems.

Chapter 4

Exciton-driven photoisomerization in photoswitch-quantum dot nanohybrids

4.1 Introduction and scope

In this chapter, the multiscale Hybrid Configuration Interaction (HyCI) framework introduced in Section 2.1 is applied to a photoswitch–quantum dot (PhS–QD) nanohybrid composed of azobenzene (AZB) and a CdSe quantum dot (CdSeQD). The goal is to explore how intrinsic excitonic coupling between molecular and nanoparticle excitations can reshape the photoisomerization pathway of AZB along its CNNC dihedral angle, without relying on optical cavities or externally imposed strong light–matter coupling.

The HyCI approach provides a natural theoretical setting for this problem: molecular and nanoparticle excitations are first characterized independently, and their interaction is then treated explicitly at the excitonic level. This enables a non-perturbative description of hybrid excited states, capturing resonance conditions, avoided crossings, and redistribution of oscillator strength that emerge from genuine molecule–nanoparticle coupling.

The results presented in this chapter correspond to a manuscript submitted to *Nanoscale* and currently under peer review. [175] Apart from minor adaptations in notation and formatting to fit the structure of this thesis, the scientific content follows that work.

This chapter proceeds from fragment-specific properties to hybrid excitonic behavior. First, Section 4.2 summarizes the system-specific numerical parameters and computational setup used to implement the HyCI framework for the AZB–CdSeQD nanohybrid. Building on this foundation, Section 4.3 analyzes the potential energy surfaces and key electronic transitions of isolated AZB along the photoisomerization coordinate. Section 4.4 then discusses the excitonic spectrum of CdSe quantum dots and identifies the resonance window relevant for coupling to AZB excitations. Section 4.5 presents the core results of this chapter: the formation of hybrid excitonic states, avoided crossings along the reaction coordinate, and the associated redistribution of oscillator strength that signals coherent molecule–QD hybridization. Finally, Section 4.6 summarizes the main findings and outlines possible directions for future work.

4.2 Parameters and computational details

The physical and material parameters used for CdSeQD and for the AZB-CdSeQD geometry are summarized in Table 4.1. These parameters are fixed throughout this chapter unless otherwise stated.

Table 4.1: Parameters used for CdSeQD and AZB–CdSeQD calculations.

Parameter	Symbol / Units	Value / Source
CdSe effective electron mass	m_e^* [m_0]	0.112 (Ref. 170)
CdSe effective heavy-hole mass	m_h^* [m_0]	0.450 (Ref. 170)
CdSe optical dielectric constant	$\varepsilon_{\mathrm{QD}}$ [ε_0]	6.20 (Ref. 170)
Environment dielectric constant	ε_{out} [ε_0]	1 (vacuum)
CdSe bulk band gap	$E_{\mathrm{gap}}^{\mathrm{bulk}}$ [eV]	1.74 (Ref. 170)
CdSe bulk transition momentum	P [a.u.]	1.21 (Ref. 176)
AZB characteristic radius	R_{AZB} [nm]	0.563 (Ref. 75)
H van der Waals radius	$R_{\mathrm{VdW}}^{\mathrm{H}}$ [nm]	0.167 (Ref. 173)

Unlike the porphine molecule discussed in Chapter 3, AZB is not rigid: while its overall orientation can be fixed, the CNNC dihedral angle remains an active nuclear degree of freedom during photoisomerization between *trans* and *cis* configurations (see Fig. 1.3). Accordingly, potential energy surfaces (PESs) along the CNNC degree of freedom of AZB were constructed through a sequence of constrained geometry optimizations at fixed dihedral angles, while allowing all remaining internal coordinates to relax. Adaptive angular step sizes were employed, with finer resolution in regions of near-degeneracy, to ensure numerical stability of the PESs. No symmetry constraints were imposed during the geometry optimizations.

The ground state (M_0) and the first 30 singlet excited states (M_1–M_{30}) in vacuum of AZB were computed, which cover the main absorption peaks in the visible and near-UV spectral regions as reported in Ref. 80. Ground-state geometries were optimized using the B3LYP hybrid exchange-correlation functional and the aug-cc-pVDZ basis set. Excited-state energies and transition properties were evaluated at the same level of theory to ensure consistency between ground- and excited-state treatments.

All AZB calculations were performed with stringent numerical accuracy. The tight self-consistent-field convergence thresholds, dense integration grids, and diagonalization settings described in Section 3.2 for H_2P were also employed here, ensuring a consistent numerical treatment in all studied cases.

On the nanoparticle side, CdSeQDs with radii $R_{\mathrm{QD}} = 2$–5 nm were treated using the same numerical discretization and single-particle (SP) convergence settings described in Section 3.2 for GaNQDs, ensuring a consistent level of numerical accuracy. The surrounding environment of the QD was taken as vacuum, in line with the AZB calculations.

The excitonic states of the CdSeQDs were computed based on the 20 lowest-energy electron states and 57 lowest-energy hole states, with angular quantum numbers $0 \leq \ell \leq 3$ and magnetic quantum number $-\ell \leq m \leq \ell$. This choice ensures that electron and hole SP states span comparable energy windows, accounting for the larger effective mass of heavy holes (see Table 4.1).

Hybrid-state calculations were performed for a CdSeQD radius of $R_{\mathrm{QD}} = 2.2$ nm, chosen to yield near-resonance between the AZB $M_0 \rightarrow M_1$ excitation and the lowest bright QD exciton.

The QD center of mass is fixed at the origin, while the AZB center of mass (CoM) is always placed at $\mathbf{R} = (0, 0, 2.94)$ nm along the QD spin-up zenith direction. Given both the molecule-QD separation and the ratio $R_{\mathrm{QD}}/R_{\mathrm{AZB}} \approx 3.9$ (see Table 4.1), the dipole–field approximation for the M-NP interaction is well justified (see Section 2.1.3.2).

With the computational framework and numerical parameters now specified, we address the electronic-structure results that form the building blocks of the hybrid system. We begin by analyzing the isolated molecular fragment, focusing on the potential-energy surfaces and low-lying excited states of AZB along its photoisomerization coordinate. These molecular features define the energetic and dipolar landscape against which coupling to CdSeQD excitons can occur.

4.3 Azobenzene: PES and Key Transitions

The Potential Energy Surfaces (PESs) of AZB along the CNNC dihedral angle ϕ are shown in Fig. 4.1. Together with the CNC inversion angle, this internal coordinate is widely recognized as the principal molecular degree of freedom governing the photoisomerization process. [76] The angle ϕ span 10°–180°, corresponding to the *cis* and *trans* configurations, respectively. Only the ground state M_0 and the first five excited states (M_1–M_5) are shown in Fig. 4.1 for clarity.

The ground-state PES (M_0) along the CNNC dihedral angle was computed using constrained geometry optimizations (see Section 4.2). This procedure was particularly challenging in the range $\phi = 80°$–$100°$, where the PESs of M_0 and M_1 approach near-degeneracy across multiple nuclear degrees of freedom, giving rise to a conical intersection. In the vicinity of the conical intersection (91°–99°), numerical instabilities required an inverse scan direction to ensure convergence of the PES.

The PESs exhibit an asymmetric energy landscape. Across all states, the energy profile near the *trans* region ($\phi = 180°$) lies lower than in the *cis* region ($\phi = 10°$), producing steeper slopes (stronger forces) during photoisomerization as the system approaches the *trans* geometry compared to the *cis* geometry. The *trans* configuration defines the ground state (zero-energy reference), consistent with the experimentally observed thermodynamic stability. [81] In contrast, the *cis* configuration is 0.654 eV higher in energy and metastable, allowing slow, ∼1 day thermal relaxation back to the *trans* form. [79] The lowest excited state, M_1, originates from an $n \rightarrow \pi^*$ transition, in which an electron is promoted from a nonbonding orbital on the nitrogen atoms into the antibonding π^* orbital. This state is dark, with weak oscillator strength, and lies energetically below the bright $\pi \rightarrow \pi^*$ transition that defines M_2. [78]

In the region of the conical intersection, the M_1 surface shows sharp changes as it approaches M_0 at $\phi = 82°$ and $\phi = 98°$, whereas M_0 evolves smoothly without any avoided crossing. Near $\phi = 90°$, both states exhibit a peak, and several higher excited states display discontinuities in their profiles. These anomalies are not numerical artifacts but signatures of a rapidly changing electronic wavefunction. At the conical intersection, nuclear and electronic motions become strongly coupled. Consequently, the system can undergo nonadiabatic transitions from M_1 to M_0 with high probability, providing an efficient internal conversion pathway. [78] This ultrafast relaxation channel is therefore the primary contributor to the high quantum yield of AZB photoisomerization and the main target for potential control strategies.

A relevant gap of 0.433 eV is observed between M_1 and M_2, ensuring that transitions from M_0 to M_1 remain well separated from higher excited states. The computed $\mathrm{M}_0 \rightarrow \mathrm{M}_1$ excitation

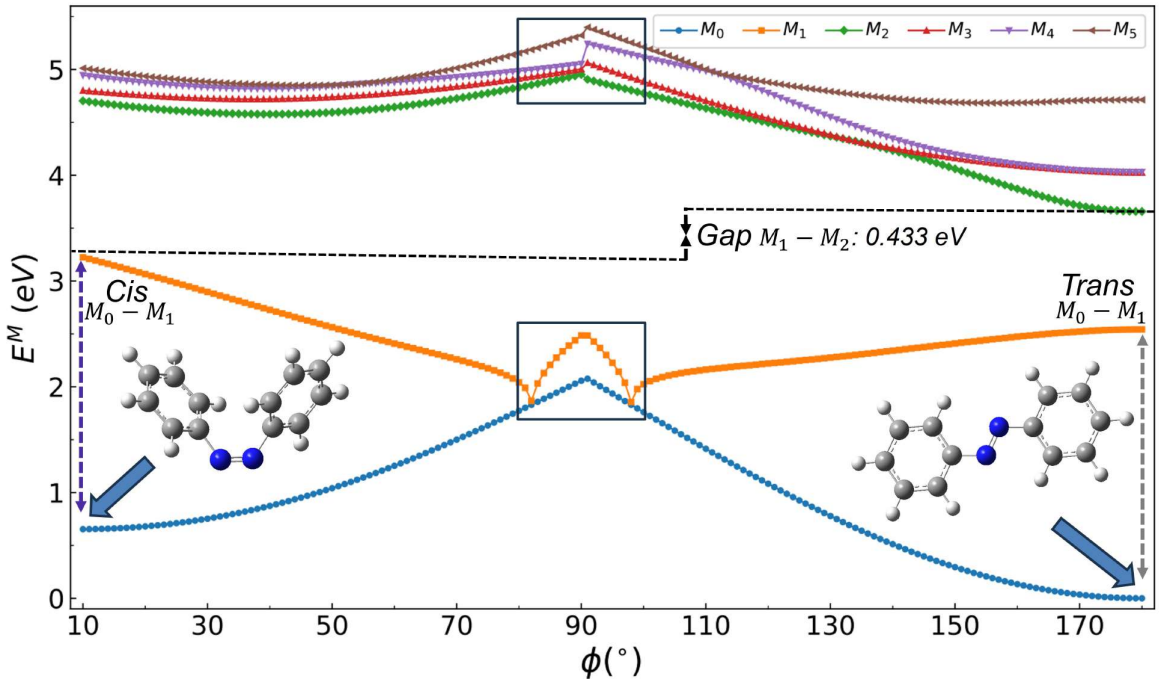

Figure 4.1: PESs of AZB as a function of the CNNC dihedral angle ϕ for the ground state (M_0) and the lowest five excited states (M_1–M_5). The *cis* ($\phi = 10°$) and *trans* ($\phi = 180°$) configurations are shown. Solid blue arrows mark their ground-state energies, with zero reference for *trans* and 0.654 eV for *cis*. Gray and violet dashed arrows indicate the $M_0 \rightarrow M_1$ transition energies, with values of 2.54 eV for *trans* and 2.57 eV for *cis*, respectively. Black dashed lines and arrows indicate the M_1–M_2 gap that isolates the $M_0 \rightarrow M_1$ transitions. A conical intersection between $\phi = 80°$ and $\phi = 100°$ (squares) leads to strong nonadiabatic coupling that drives efficient relaxation between M_0 and M_1. These features highlight M_0 and M_1 as the key states for photo-control in AZB–QD nanohybrids.

energies along the CNNC dihedral angle yield $\Delta E^{(\mathrm{cis})}_{M_0,M_1} = 2.57$ eV and $\Delta E^{(\mathrm{trans})}_{M_0,M_1} = 2.54$ eV. The *cis* value thus represents the maximum along the key photoisomerization pathway and sets the upper threshold for resonance with QD excitons in the nanohybrid system.

4.4 CdSe Quantum Dot: Excitonic Spectrum and Resonance

Figure 4.2 shows the total excitonic energies E^{NP} of the first 20 multiparticle states (NP_1–NP_{20}) for an exciton in spherical CdSe QDs in vacuum. The ground state (NP_0) corresponds to the Γ-point of the valence band and defines the zero-energy reference, representing the configuration without any electron–hole excitation.

In analogy with other spherical quantum dots (see subsection 3.3.2), the plateaus observed in the spectra arise from degeneracies imposed by spherical symmetry, corresponding to linear combinations of electron and hole states with the same orbital quantum number ℓ. In addition, each exciton state is intrinsically two-fold degenerate (not shown for clarity), due to the spin degeneration of heavy-hole band states (see Sec. 2.1.2.2).

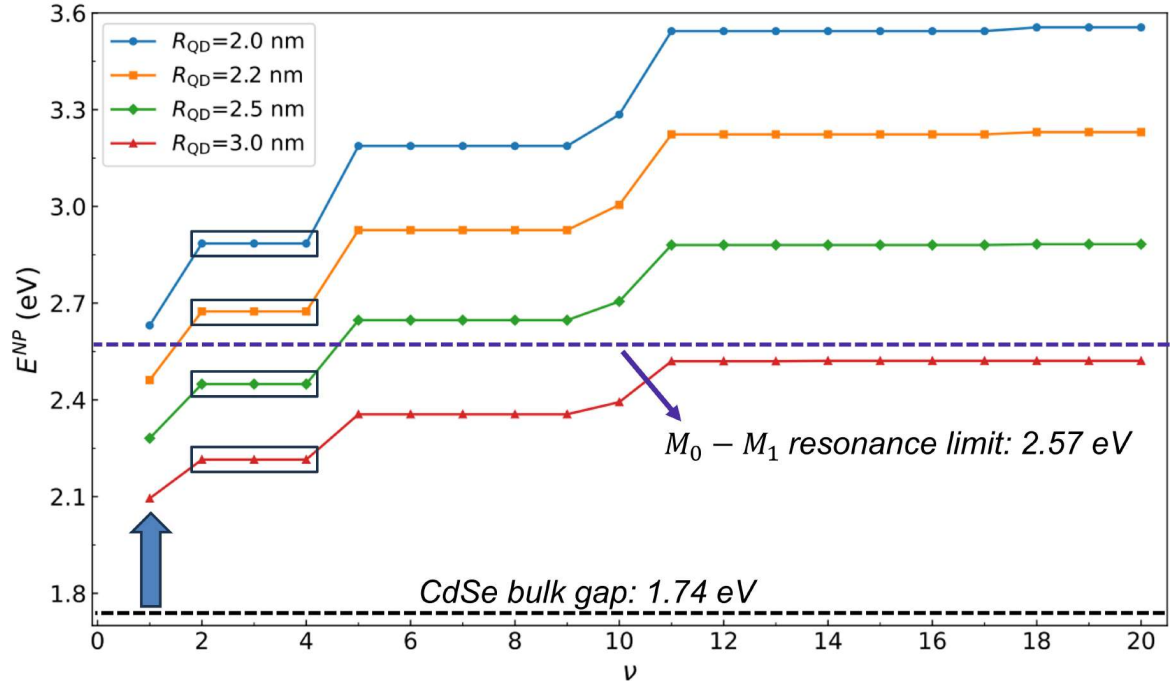

Figure 4.2: Total excitonic energies E^{NP} of CdSe QDs in eV as a function of the multiparticle state index ν. The ground state (NP_0), with no electron–hole excitation, defines the zero-energy reference. Each curve corresponds to a different radius between 2 and 3.0 nm. Spherical symmetry leads to degeneracy of the ℓ-states (illustrated with squares at $\ell = 1$). The solid blue arrow highlights the widening of the optical gap: as the radius decreases and quantum confinement strengthens, the NP_1 energy shifts upward relative to the bulk gap (black dashed line). The violet dashed line and solid arrow indicate the energy threshold for QD excitons that can resonate with the $M_0 \rightarrow M_1$ excitation in AZB during photoisomerization.

Quantum confinement effects increasingly shift the excitonic energies from the bulk bandgap at 1.74 eV for smaller QDs, widening the effective optical bandgap E_{gap}—defined by the NP_1 energy at each radius R_{QD}.

The optical gap therefore sets the lower threshold, while the molecular excitation $\Delta E^{(\text{cis})}_{M_0,M_1}$ of AZB defines the upper threshold (see Sec. 4.3). Only QD excitons within the window $[E_{\text{gap}}, \Delta E^{(\text{cis})}_{M_0,M_1}]$ can resonate with the $M_0 \rightarrow M_1$ transition and actively participate in the nanohybrid photodynamics. By changing R_{QD} (and possibly the QD material or dielectric environment) the resonance window can be tuned to match the molecular transition in a specific device architecture. For example, the CdSe QD with radius 2.2 nm (see Fig. 4.2) resonates only with the lowest excitonic state, whereas QDs with radius 2.0 nm lie above the molecular transition and cannot contribute to the resonance. In larger dots, the number of resonant states increases significantly: a 2.5 nm QD supports 4 excitonic states within the window, while a 3.0 nm QD provides 20 states in resonance.

In addition to energy tuning, the QD transition electric field also varies systematically with size. The magnitude of the matrix element $\langle \text{NP}_0 | \hat{\mathbf{E}}^{\text{NP}}(\mathbf{R}) | \text{NP}_1 \rangle$ (Sec. 2.1.3.4), evaluated near the QD spin-up zenith $\mathbf{R} = (0, 0, R_{\text{QD}})$, increases as R_{QD} decreases (not shown). Indeed, accounting for charge redistribution within the QD due to variations in quantum confinement,

the overall distance dependence of the transition electric field follows a $\sim |\mathbf{R}|^{-2.05}$ scaling, as revealed by a fit to the data for QDs with radii of 2–3 nm. Because the molecule–nanoparticle interaction in Eq. (2.28) depends linearly on this field, this scaling provides a straightforward handle to modulate the coupling strength independently of resonance conditions.

4.5 Azobenzene + CdSe Quantum Dot: Excitonic Couplings and Hybridization

We next analyze the nanohybrid of AZB coupled to CdSeQD with radius $R_{\mathrm{QD}} = 2.2$ nm. Only the NP_1 excitonic state lies within the key resonance window for photoisomerization of AZB (see Section 4.4), with the corresponding resonant energy being 2.46 eV. Accordingly, the hybrid analysis in this section is restricted to product states involving the ground and first excited states of AZB ($|M_0\rangle$, $|M_1\rangle$) and the $|NP_0\rangle$ and $|NP_1\rangle$ states of CdSeQD, using the nanohybrid geometry defined in Section 4.2.

Before analyzing the excitonic coupling, we examined the orientation of the molecular dipoles along the photoisomerization pathway. The $M_0 \rightarrow M_1$ transition dipole maintains an approximately constant direction along the CNNC angle ϕ, while the M_0 and M_1 static dipoles remain orthogonal to it and nearly parallel to each other (not shown). Exploiting this rigidity, the molecular reference frame was chosen such that the $M_0 \rightarrow M_1$ transition dipole at $\phi = 16.3°$ (identified *a posteriori* as a resonant geometry) aligns with the laboratory z axis, which coincides with the QD electric-field direction of the spin-up channel (see Section 2.1.3.4). The same rotation was applied consistently to all molecular dipoles. As a consequence, the QD field associated with the spin-down channel remains nearly orthogonal to the AZB dipoles throughout the photoisomerization pathway (not shown) and is therefore omitted from further consideration in this section.

Figure 4.3 plots the magnitude of the coupling matrix element $\langle M_0, \mathrm{NP}_1 | \hat{V}^{\mathrm{M\text{–}NP}} | M_1, \mathrm{NP}_0 \rangle$ as a function of the CNNC dihedral angle ϕ. All other couplings vanish or are negligible, as the associated QD field is zero or nearly orthogonal to the relevant molecular dipoles.

As expected for cavity-free hybrid states, these intrinsic couplings remain in the meV range, with a maximum of about 3.1 meV. They are therefore much weaker than the couplings reported for AZB under strong light–matter interaction, which reach values of about 150 meV in polaritonic states. [76] Nevertheless, their cumulative contribution over the picosecond's lifetime of photoisomerization renders them relevant for the nanohybrid dynamics. The figure also highlights pronounced features near $\phi = 82°$ and $\phi = 98°$, which correspond to the conical intersection region of AZB (see Sec. 4.3).

The coupling is nearly zero close to the *trans* configuration, where the $M_0 \rightarrow M_1$ transition dipole moment of AZB vanishes due to molecular symmetry. In contrast, the *cis* configuration exhibits a relatively stronger coupling, reflecting the larger oscillator strength associated with its symmetry-broken geometry.

Away from the *cis* and *trans* regions, the coupling initially increases, reaching local maxima around $\phi = 60°$ and $\phi = 130°$. As ϕ approaches the conical intersection, the coupling decreases again and becomes very small at the actual crossing points of M_1 and M_0 (see Sec. 4.3). However, sharp peaks emerge nearby, particularly around $\phi = 90°$, where the coupling rises abruptly. These discontinuities originate from sudden changes in the molecular dipole caused

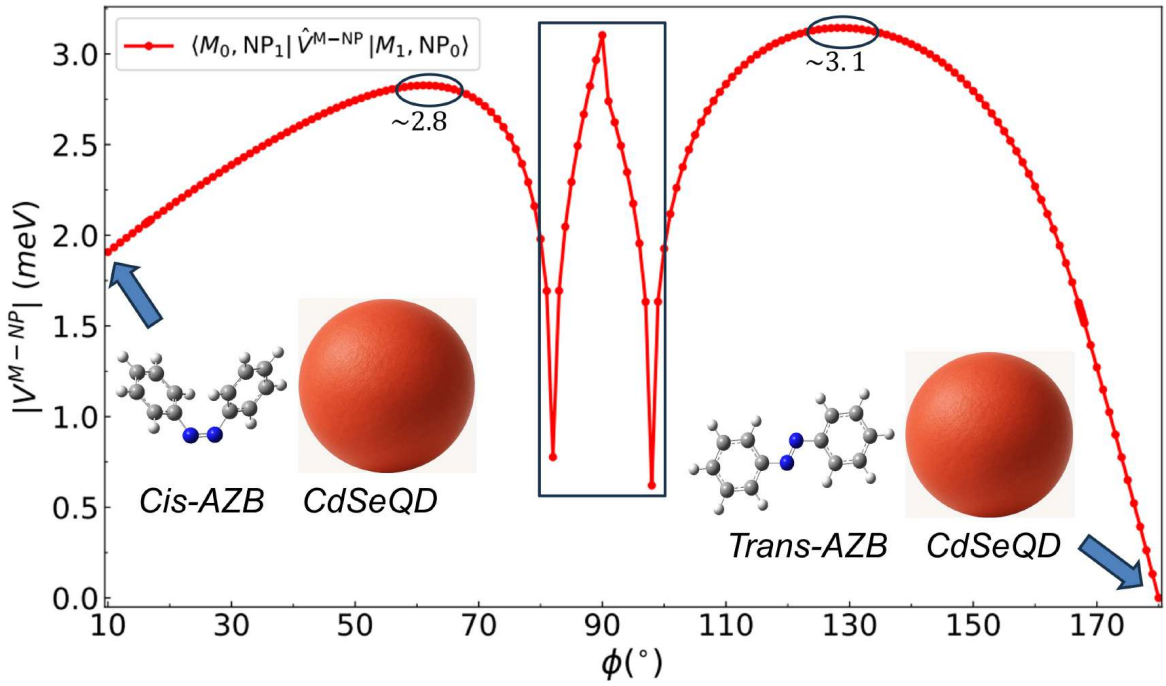

Figure 4.3: Magnitude of the HyCI coupling matrix element $\langle M_0, \mathrm{NP}_1|\hat{V}^{\mathrm{M-NP}}|M_1, \mathrm{NP}_0\rangle$ along the CNNC dihedral angle ϕ in AZB-CdSeQD system ($R_{\mathrm{QD}} = 2.2$ nm, $\mathbf{R} = (0, 0, 2.94)$ nm). Arrows indicate the *trans* and *cis* nanohybrid configurations (not to scale). A square marks the conical intersection region, while circles highlight local maxima (∼2.8–3.1 meV) away from this region. Within the conical intersection, sharp peaks appear near $\phi = 82°$ and $\phi = 98°$, correlating with M_1–M_0 near-degeneracy, and an additional maximum occurs at $\phi = 90°$. Discontinuities around the latter arise from nonadiabatic effects (see Sec. 4.3).

by nuclear rearrangements through the conical intersection, a hallmark of nonadiabatic effects. [177]

Figure 4.4 presents the hybrid PESs of the AZB-CdSeQD system ($R_{\mathrm{QD}} = 2.2$ nm, $\mathbf{R} = (0, 0, 2.94)$ nm). As in the isolated molecule case (Sec. 4.3), the PESs are plotted as a function of the CNNC dihedral angle ϕ. The zero-energy reference in Eq. (2.24) is set at the ground state energy of the QD, and all absolute energies of AZB states —across *cis*, *trans*, and intermediate configurations— were shifted accordingly.

The energies of the hybrid ground state Ψ_0 and the excited state Ψ_3 track those of isolated AZB along the entire photoisomerization pathway (Sec. 4.3), apart from an overall shift induced by the QD. Being off resonance, they remain essentially unmixed—dominated by $|M_0, \mathrm{NP}_0\rangle$ and $|M_1, \mathrm{NP}_1\rangle$ contributions, respectively.

By contrast, the hybrid excited states Ψ_1 and Ψ_2 behave differently. Two avoided crossings appear near $\phi = 16.3°$ and $\phi = 167.7°$, where the AZB $M_0 \to M_1$ transition (~ 2.46 eV) is nearly resonant with the lowest bright QD exciton (NP_1). Under these near-resonant conditions, the molecule–QD interaction reshapes the CNNC PES and drives coherent hybridization: both states acquire mixed $|M_0, \mathrm{NP}_1\rangle$ (QD-like) and $|M_1, \mathrm{NP}_0\rangle$ (AZB-like) character, becoming delocalized within these angular windows. Away from the avoided crossings, they show predominantly AZB-like or QD-like character.

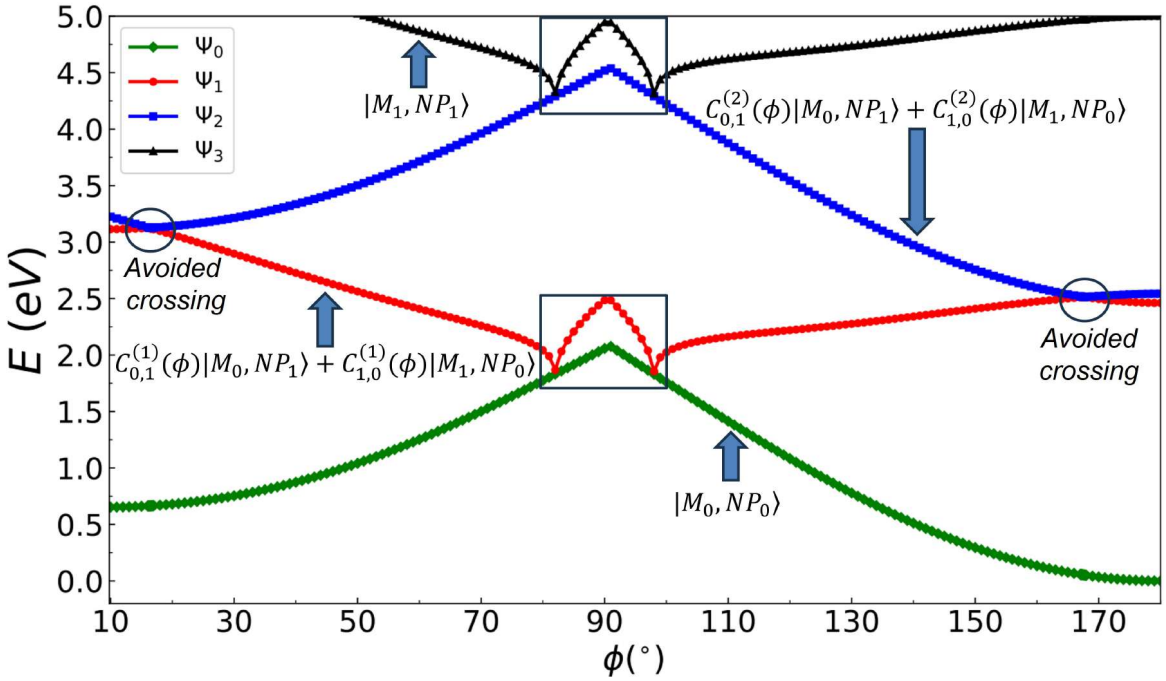

Figure 4.4: Ground (Ψ_0) and excited (Ψ_1–Ψ_3) hybrid PESs of the coupled AZB–CdSeQD system ($R_{\mathrm{QD}} = 2.2$ nm, $\mathbf{R} = (0, 0, 2.94)$ nm) as a function of the CNNC dihedral angle ϕ. Squares mark the AZB conical intersection (see Sec. 4.3). Arrows indicate the dominant contributions to each hybrid state along the photoisomerization pathway. Circles highlight avoided crossings near $\phi = 16.3°$ and $\phi = 167.7°$, where the $M_0 \rightarrow M_1$ excitation of AZB becomes resonant with the lowest bright QD exciton (NP_1). This near-degeneracy enables coherent hybridization between molecular and QD excitations. Tuning the QD radius shifts the location of the avoided crossings.

To quantify the dynamical significance of these avoided crossings, we estimated the adiabatic transition probabilities P_{adiab} associated with a single passage through each crossing using a two-state Landau-Zener model. [178] As expected for the weak excitonic coupling in this cavity-free nanohybrid, the probability of remaining on the same hybrid (adiabatic) state is small, with values amounting to $P_{\mathrm{adiab}} \approx 2.69\%$ for the avoided crossing at $\phi \approx 16.3°$ and $P_{\mathrm{adiab}} \approx 4.26\%$ for the avoided crossing at $\phi \approx 167.7°$. Despite their small magnitude, these values are not negligible. Over the picosecond photoisomerization dynamics of AZB, such probabilities can contribute cumulatively to population redistribution between hybrid states. Full details of the Landau-Zener analysis and its computational procedure are provided in Appendix B.

Notably, the position of the avoided crossings along the photoisomerization pathway are tunable. As discussed in Sec. 4.4, adjusting the QD radius, core material or dielectric environment shifts its excitonic spectrum through quantum confinement, thereby controlling the energy at which the NP_1 exciton resonates with the AZB excitation.

Figure 4.5 presents an enlarged view of the avoided crossing near $\phi \approx 16.3°$ on a relative meV scale, using a constant plotting offset $E_{\mathrm{off}} = 3120$ meV for visualization only. Coupled surfaces ($V^{\mathrm{M–NP}} \neq 0$) are shown alongside their uncoupled counterparts ($V^{\mathrm{M–NP}} = 0$), making the level repulsion $\Delta E(\phi) = E_{V\neq 0}(\phi) - E_{V=0}(\phi)$ apparent. State contributions are also indicated, highlighting the contrast between the delocalized character of the coupled states and the pure-

state nature of the uncoupled ones.

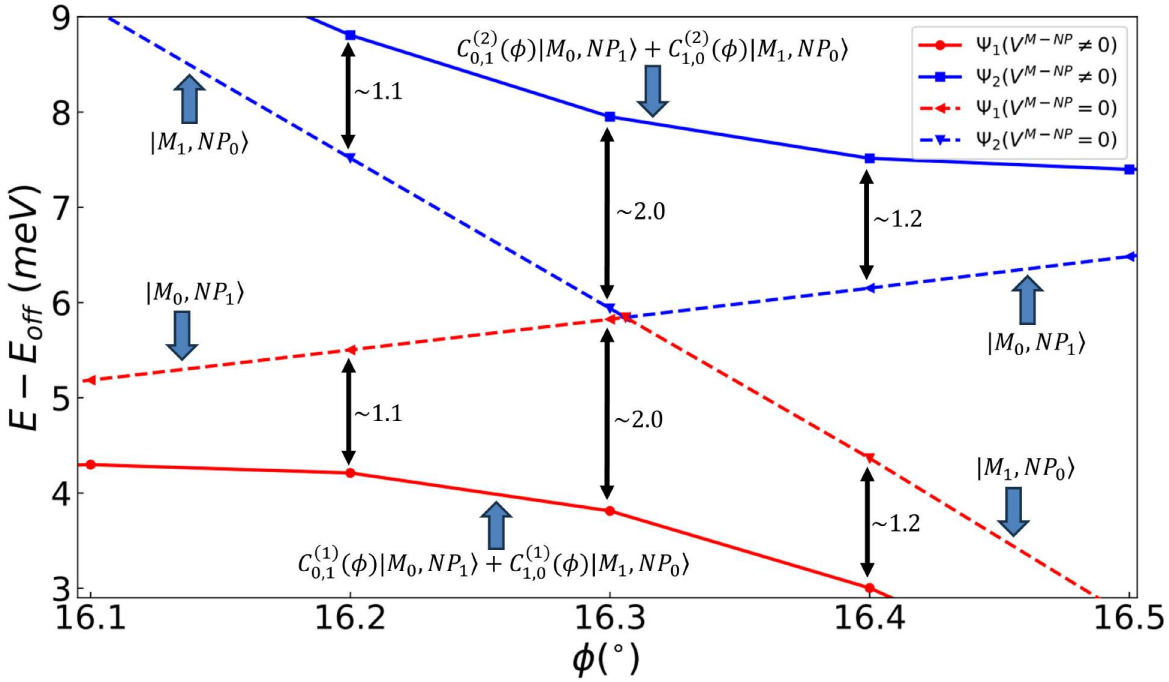

Figure 4.5: Zoomed view of the hybrid PESs of the AZB–CdSe QD system ($R_{\mathrm{QD}} = 2.2$ nm, $\mathbf{R} = (0, 0, 2.94)$ nm) around $\phi \approx 16.3°$. Energies are plotted as $E - E_{\mathrm{off}}$ (meV) with a constant offset $E_{\mathrm{off}} = 3120$ meV applied for visualization only. Solid and dashed curves denote the coupling and no-coupling cases, respectively. Blue arrows highlight the dominant state contributions along the photoisomerization pathway, while black arrows indicate the level repulsion $\Delta E(\phi) = E_{V\neq 0}(\phi) - E_{V=0}(\phi)$. The total splitting $E_{split} = |\Delta E_{\Psi_1}(\phi)| + |\Delta E_{\Psi_2}(\phi)$—, with a maximum value of ~ 4.0 meV at $\phi = 16.3°$, is a measure of the mixing strength between the AZB $M_0 \rightarrow M_1$ transition and the QD's lowest bright exciton (NP_1).

The total splitting, defined as $E_{\mathrm{split}} = |\Delta E_{\Psi_1}(\phi)| + |\Delta E_{\Psi_2}(\phi)|$ quantifies the mixing strength between the AZB $M_0 \rightarrow M_1$ transition and the QD's lowest bright exciton (NP_1), with a maximum value of ~ 4.0 meV at $\phi = 16.3°$. The analogous avoided crossing near $\phi \approx 167.7°$ exhibits a maximum total splitting of ~ 3 meV (not shown). Taken together, these total splittings corroborate that the observed avoided crossings arise from genuine hybridization.

The splitting at the avoided crossings are tunable by changing the excitonic coupling. Variations in the QD radius, core material and dielectric environment influence the coefficients of excitonic states, changing the magnitude of electric field matrix elements. The accessible range of $|\mathbf{R}|$ is also relevant: smaller dots enable the molecule to approach closer to the QD surface, thereby enhancing the electric field strength. In addition, modifying the relative orientation of the AZB molecule or its position $\mathbf{R}$ in space with respect to the QD alters the dipolar alignment with the electric field, thus modulating the excitonic coupling and reshaping the hybridization strength.

Lastly, Figs 4.6 illustrate the evolution of the dipole moment magnitudes of the transitions $\Psi_0 \rightarrow \Psi_1$ and $\Psi_0 \rightarrow \Psi_2$ at the AZB and QD segments as functions of the CNNC dihedral angle ϕ. A pronounced redistribution of oscillator strength is observed near the avoided crossings (cf. Fig. 4.4), where AZB and QD excitations become resonant. In these regions, the molecular

dipole moment decreases while the QD contribution increases or viceversa, resulting in a rapid transition of dipole character between the two fragments. This continuous interpolation is a hallmark of excitonic hybridization, where the excitation is no longer confined to a single component but delocalized across the nanohybrid.

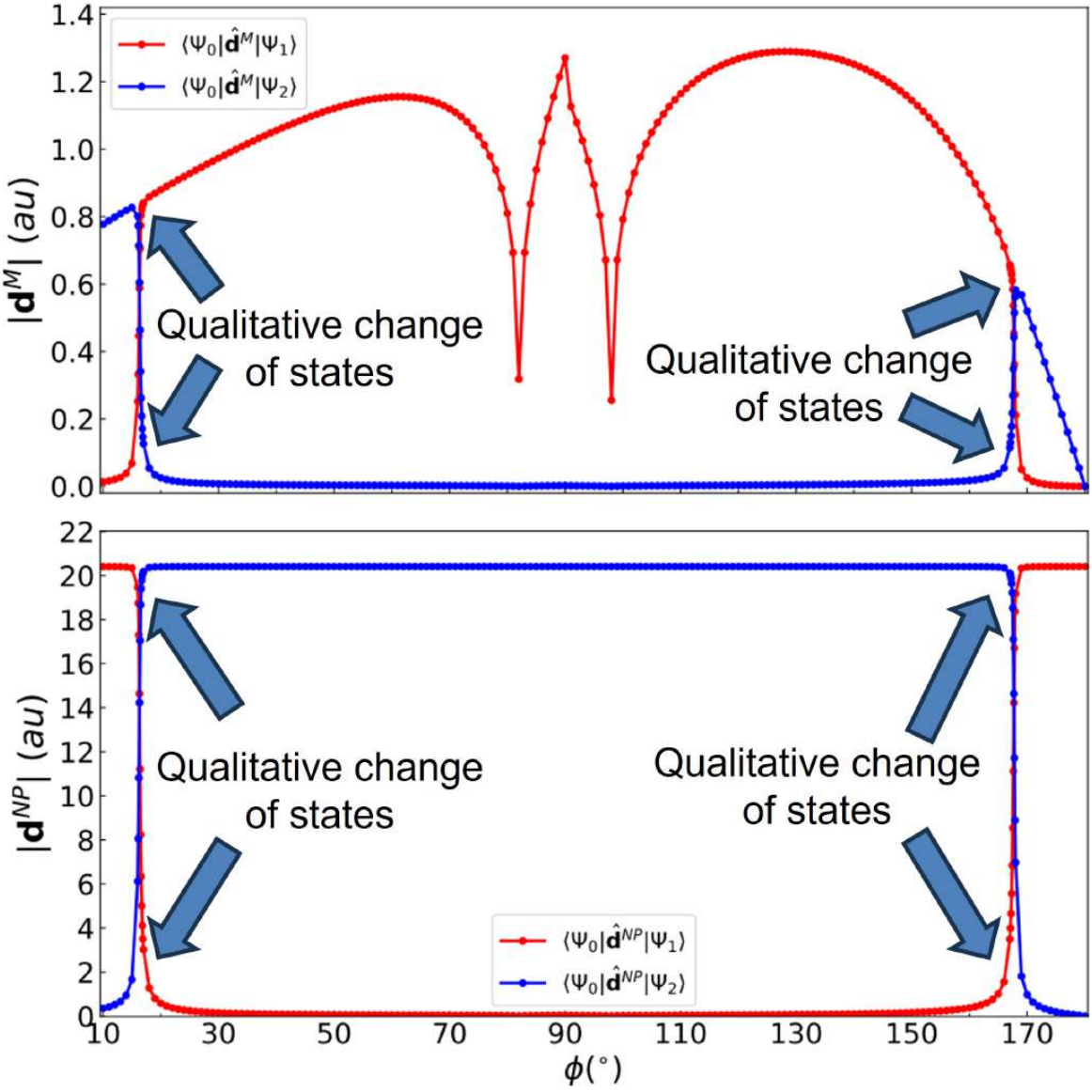

Figure 4.6: Evolution of transition dipole-moment magnitudes of hybrid states as functions of the CNNC dihedral angle ϕ, resolved into contributions from (top) the molecular AZB fragment and (bottom) the CdSe QD fragment. Sharp variations appear near the avoided-crossing regions (indicated by arrows), reflecting redistribution of oscillator strength as molecular and QD excitations become resonant and exchange character. Outside these regions, the molecular dipole evolution follows a profile similar to that of the excitonic coupling (cf. Fig. 4.3), while the QD dipole remains nearly constant at ~ 20.4 a.u., maintaining a strong bright character.

Outside the resonance regions, the non-zero evolution of the molecular dipoles closely mirrors the excitonic coupling profile shown in Figure 4.6, with peaks corresponding to stronger

interaction. In contrast, the non-zero evolution of the QD dipole remains robustly high, centered around 20.4 a.u., and shows only negligible fluctuations. This stability indicates that the QD state maintains a strong bright nature throughout the photoisomerization, with only modulations induced by coupling with AZB at resonance. Together, the two figures reinforce that light–matter interaction in this nanohybrid system is not statically localized but instead dynamically redistributed along the reaction coordinate, enabling modulation of photo-response properties through molecular motion.

It is worth noting that for larger QDs, where multiple excitonic states fall within the resonance window defined by the AZB $M_0 \rightarrow M_1$ transition, the hybridization scenario would become correspondingly more complex. In such cases, several QD excitons could simultaneously couple to the molecular excitation, giving rise to a manifold of interacting hybrid states and to multiple avoided crossings along the photoisomerization pathway, accompanied by a corresponding exchange of dipole character. While these multi-state resonance effects are naturally captured within the HyCI framework (see Section 3.4), the present analysis has focused on the minimal case in which a single bright QD exciton is resonant, in order to isolate and interpret the fundamental mechanisms of exciton-driven photoisomerization.

4.6 Conclusions

In this chapter, we applied the Hybrid Configuration Interaction (HyCI) framework to investigate the electronic structure and excitonic properties of a model PhS–QD nanohybrid composed of AZB and a CdSe QD.

We identified two clear avoided crossings near $\phi \approx 16.3°$ and $\phi \approx 167.7°$, occurring where the AZB $\mathrm{M}_0 \rightarrow \mathrm{M}_1$ excitation becomes nearly resonant with the lowest bright exciton (NP_1) of the QD with $R_{QD} = 2.2$ nm. The excitonic coupling opens a maximum energy splitting of ~ 4.0 meV, as a signature of coherent hybridization between fragment excitations. The *location* of these splittings is governed primarily by *resonance* (energetic alignment), whereas the *magnitude* (intensity) is set by the coupling strength—emphasizing QD size and spectral tuning, as key design handles.

Importantly, these hybridization effects arise without optical cavities or external fields: cavity-free nanohybrids can still exhibit meaningful excitonic reshaping of molecular reactivity. Moreover, the relevant excitons live on nanosecond timescales, better matched to the picosecond-photoisomerization dynamics of AZB. HyCI enables these insights by capturing correlation across molecular and nanoscale subsystems with accuracy.

Analysis of hybrid transition dipoles reveals a dynamic redistribution of oscillator strength between the AZB and QD components near the avoided crossings. In these regions, the molecular dipole moment decreases while the QD contribution increases (or vice versa), producing a rapid transition of dipole character between the two fragments. This continuous interpolation underscores the delocalized nature of the excitation and indicates that the optical response can be steered through geometric or environmental control.

Overall, PhS–QD nanohybrids provide a cavity-free platform for exciton-mediated photomodulation. By tuning the QD size, material composition, or molecular attachment geometry, one can engineer the hybridization landscape to influence reaction yields or energy-transfer pathways—offering routes toward tailored, light-driven nanodevices.

Looking ahead, a natural extension of this work would be to employ surface-hopping

molecular-dynamics simulations to model full photoisomerization trajectories, making use of the computed hybrid PESs and coefficients along the principal coordinate. [142, 143, 144] Such an approach could quantify nonadiabatic population transfer near avoided crossings and at the conical intersection. These beyond-adiabatic simulations remain computationally demanding, and are therefore left for future investigations.

In summary, PhS–QD systems offer a robust, tunable, and scalable strategy for light-driven control in molecular systems—pointing to a class of excitonic photochemistry beyond the cavity paradigm.

Chapter 5

Correlated transport of indirect excitons driven by surface acoustic waves in the presence of impurities

5.1 Introduction and Scope

In this chapter, the two-particle description for the transport of SAW-driven SIXs, introduced in Section 2.2, is applied to a CQW of GaAs/AlGaAs in the presence of localized electrostatic impurities. We focus on a single-impurity configuration, which provides a controlled and physically transparent setting to analyze how scattering centers affects exciton transport under SAW driving in a prototypical and experimentally well-established CQW platform.

Within this framework, the full electron-hole wave function is propagated in real time in the frame co-moving with the SAW. This enables an easier investigation of how the impurity position along the growth and transverse directions determine the transport outcome.

A central aspect of this study is the explicit treatment of the coupling between internal electron–hole dynamics and center-of-mass motion, which becomes particularly relevant in the presence of localized impurities. The correlated two-particle description naturally captures this interplay and enables correlation-induced effects to be identified and quantified beyond simplified descriptions.

The results presented in this chapter extend the scope of the thesis from static excitonic hybridization in molecule-nanoparticle nanohybrids, discussed in Chapters 3 and 4, to the correlated transport of excitons in a solid-state device with impurities. They also constitute the basis of a manuscript currently in preparation for submission to a peer-reviewed journal. [179]

The chapter is organized as follows. Section 5.2 outlines the parameters and computational details of the numerical propagation scheme. Section 5.3 analyzes the impurity-induced potential landscape and its coupling to the exciton degrees of freedom. The resulting wave-packet dynamics of the SIX are discussed in Section 5.4, followed in Section 5.5 by a quantitative analysis of transmission probabilities as a function of impurity position and a comparison with a mean-field description. The main conclusions and implications are summarized in Section 5.6.

5.2 Parameters and computational details

The physical and material parameters employed for the GaAs/AlGaAs system and for the SAW are summarized in Table 5.1. Unless explicitly stated otherwise, these parameters are fixed throughout this chapter.

Table 5.1: Parameters used for GaAs/AlGaAs calculations.

Parameter	Symbol / Units	Value / Source
Electron effective mass	m_e [m_0]	0.067 (Ref. 132)
Heavy-hole effective mass	m_h [m_0]	0.111 (Ref. 132)
Dielectric constant	ε_r [ε_0]	12.9 (Ref. 132)
Inter-well separation	d [nm]	20.0 (Ref. 132)
SAW wavelength	λ_{SAW} [nm]	800 (Ref. 133)
SAW group velocity	v_{SAW} [m/s]	2 900 (Ref. 133)
Electron SAW potential amplitude	$U_{e,0}$ [meV]	2.00 (Ref. 132)
Hole SAW potential amplitude	$U_{h,0}$ [meV]	2.00 (Ref. 132)
Temperature	T_K [K]	4.00 (Ref. 133)
Free-carrier density	n [μm^{-3}]	1 300 (Ref. 164)

The relative and center-of-mass (CoM) coordinates are discretized on finite spatial domains of size $L_x = 600$ nm and $L_X = 12$ μm, respectively. The relative-coordinate domain is chosen sufficiently large to ensure convergence of the bound initial excitonic states and to suppress boundary effects during internal dynamics (see subsection 2.2.1), while the CoM domain spans several SAW wavelengths, allowing scattered wave packets to evolve without reaching the numerical boundaries within the simulated time window. [131]

The spatial grids consist of 256 points in the relative coordinate and 2048 points in the CoM coordinate, corresponding to uniform grid spacings of $\Delta x \approx 2.3$ nm and $\Delta X \approx 5.9$ nm, respectively. This spatial resolution guarantees convergence of the bound-state spectrum of the relative-coordinate Hamiltonian, yielding ground-state energies accurate to better than 0.1 meV, as well as converged CoM marginal probabilities. [131]

In all simulations, the excitonic wave packet is initialized with its CoM localized at $X_0 = -1400$ nm, corresponding to a minimum of the SAW potential. The initial position of the impurity along the transport axis is fixed at $x^0_{\mathrm{imp}} = -2400$ nm, i.e., more than one SAW wavelength away from the initial exciton position (see Fig.1.5).

Unless otherwise stated, we always consider a positively charged impurity in the calculations. The transverse- and growth-impurity positions (y_{imp} and z_{imp}) are varied parametrically to explore different scattering regimes (see subsection 2.2.1). In particular, the impurity coordinates are scanned in steps of 5 nm over the ranges $y_{\mathrm{imp}} \in [5, 35]$ nm and $z_{\mathrm{imp}} \in [-30, 30]$ nm. These ranges are chosen to avoid singularities in the scattering potential while still allowing access to near-impurity regimes relevant for exciton-impurity interactions.

A fixed time step of $\Delta t = 10$ fs is used in all simulations, ensuring numerical stability of the Fourier split-step (FSS) propagation (see Sec. 2.2.2). The total propagation time is set to $t_f = 1.25$ ns, which is sufficient for impurity-induced scattering to be fully completed before evaluating transport observables.

5.3 Impurity potential landscape

Having defined the relevant system parameters, we now analyze the effective action of a localized impurity potential on the excitonic degrees of freedom. Figure 5.1 shows representative profiles (centered at X_{cm}) of the impurity-induced potential $U_{\mathrm{imp}}(X_{\mathrm{cm}}, x_r, t)$, plotted as a function of the center-of-mass (CoM) coordinate X_{cm}. The transverse impurity coordinate is fixed at $y_{\mathrm{imp}} = 20$ nm, while the position along the growth direction z_{imp} is varied. For each impurity configuration, the potential is evaluated at different values of the relative coordinate x_r, which explicitly exposes the coupling between internal and CoM degrees of freedom.

When the impurity is located close to one of the quantum wells ($z_{\mathrm{imp}} = \pm 20$ nm), the effective potential exhibits a pronounced dependence on both X_{cm} and x_r. In these configurations, the impurity couples predominantly to a single constituent of the exciton. For the hole-layer case (Fig.5.1a), the hole–impurity interaction dominates, resulting in a net repulsive contribution to the CoM potential and giving rise to a *barrier-like* scattering landscape. Conversely, when the impurity is located near the electron layer (Fig.5.1b), the attractive electron–impurity interaction dominates, producing a predominantly *well-like* potential. In both cases, the imbalance between electron and hole contributions leads to strongly asymmetric and x_r-dependent scattering landscapes along the transport direction.

A qualitatively different behavior emerges when the impurity is placed at the mid-plane between the two layers (Fig. 5.1c). In this geometry, the impurity couples with comparable strength to the electron and the hole. As a consequence, the net potential is more symmetric for any x_r. In particular, at $x_r = 0$ the electron and hole share the same in-plane position along the transport direction and the exciton is locally charge neutral. In this configuration, the impurity-induced potentials acting on the two constituents nearly cancel, resulting in a vanishing or strongly suppressed CoM potential. When the electron and hole are separated along the transport direction ($x_r \neq 0$), the cancellation of electrostatic contributions is lifted. The impurity can then couple efficiently to this exciton, producing a finite X_{cm}-dependent scattering landscape.

The mid-plane configuration therefore realizes a *mixed barrier/well-like* regime, as clearly illustrated by the bottom panel of. In this geometry, the effective CoM potential results from the superposition of repulsive electron–impurity and attractive hole–impurity contributions of comparable magnitude. As a consequence, the sign and strength of the potential depend sensitively on the internal electron–hole separation x_r: for $x_r = 0$ the two contributions nearly cancel and the potential is strongly suppressed, while for $x_r \neq 0$ a finite potential emerges due to the induced internal dipole of the exciton. Compared to the asymmetric configurations, where either a barrier-like or well-like landscape dominates, the mid-plane potential is therefore substantially weakened and smoother. In this case, internal excitations are less efficiently activated, and the resulting dynamics are, in principle, expected to approach those predicted by reduced mean-field descriptions.

Overall, Fig. 5.1 demonstrates how the impurity position along the growth direction controls not only the strength but also the qualitative character of the scattering potential, as well as its coupling to internal excitonic degrees of freedom. These features anticipate the emergence of distinct transport regimes during SAW-driven propagation, which will be analyzed in the following sections.

In the following, these impurity-induced landscapes will be referred to as barrier-like when

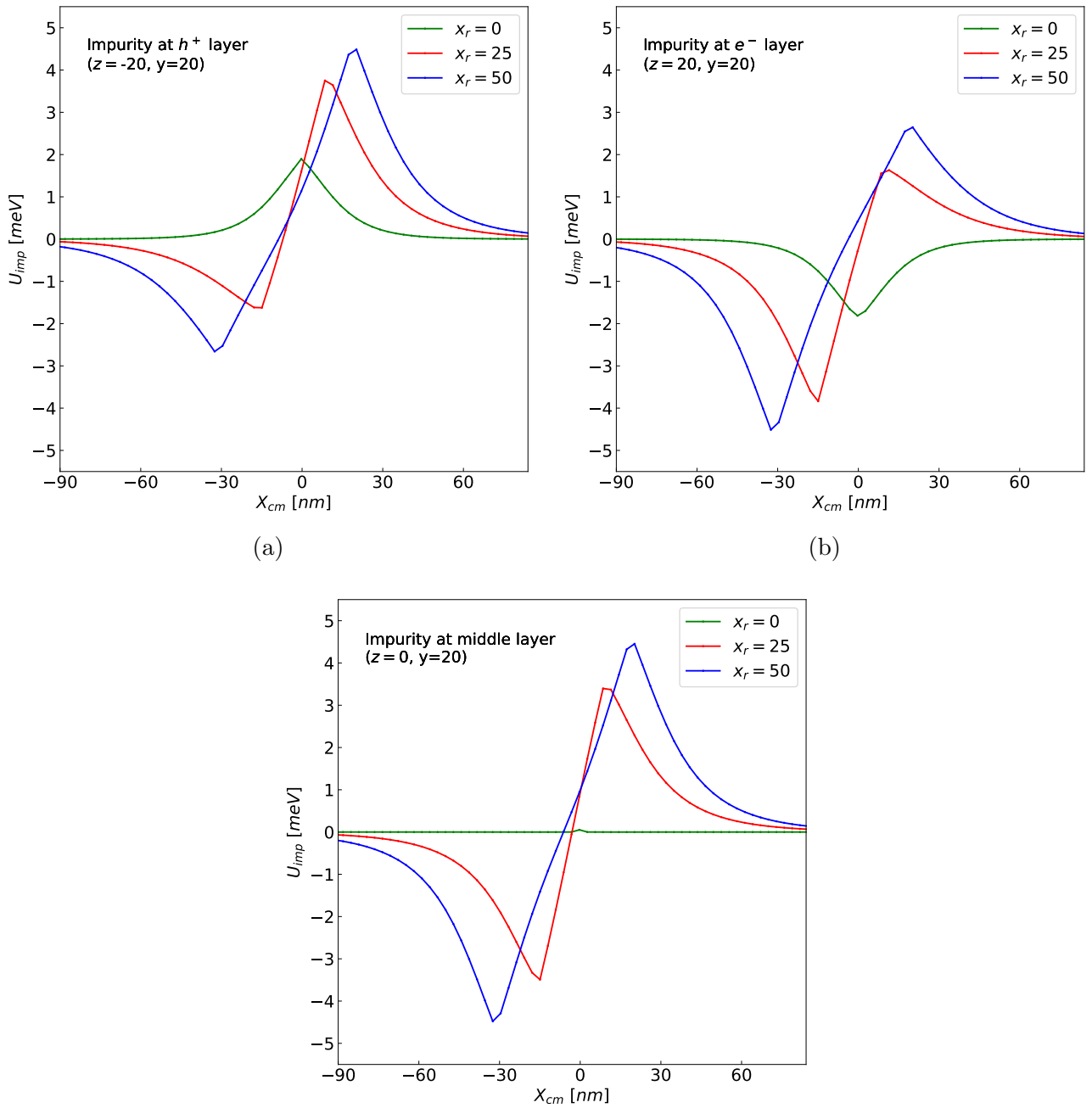

Figure 5.1: Impurity-induced potential $U_{\mathrm{imp}}(X_{\mathrm{cm}}, x_r, t)$ at $t = 10$ fs for a positive impurity placed at different positions along the growth direction. Curves correspond to different values of the relative coordinate x_r. Top panels: (a) impurity near the hole layer ($z_{\mathrm{imp}} = -20$ nm, left) and (b) near the electron layer ($z_{\mathrm{imp}} = 20$ nm, right), give rise to predominantly barrier-like and well-like scattering landscapes. Bottom panel: impurity located at the mid-plane ($z_{\mathrm{imp}} = 0$ nm), where attractive and repulsive contributions partially compensate, leading to a mixed barrier/well-like potential.

the effective CoM potential is predominantly repulsive, well-like when it is predominantly attractive, and mixed barrier/well-like in cases where the potential experienced by the exciton depends strongly on its internal configuration.

5.4 Wave packet dynamics

We now analyze the real-time dynamics of a SAW-driven SIX interacting with a localized positive impurity by examining the spatiotemporal evolution of the wave packet alongside the corresponding CoM marginal density ρ_{cm}. Each impurity configuration is presented through a two-panel figure, showing the wave-packet evolution (left) and the associated ρ_{cm} profile (right). In all cases, the transverse impurity coordinate is fixed at $y_{\mathrm{imp}} = 20$ nm.

For an impurity located near the hole layer (Fig. 5.2), the wave-packet evolution shown in panel (a) reveals that the exciton remains strongly confined within the initial SAW valley throughout the propagation. The green color scale represents the CoM marginal density $\rho_{\mathrm{cm}}(X_{\mathrm{cm}}, t)$, while the underlying red–blue background encodes the total potential in the SAW co-moving frame, with red (blue) corresponding to higher (lower) potential energy. The black rectangle highlights a spatial region where the impurity induces a strong positive distortion of the SAW potential.

As discussed in the previous section, when the wave packet traverses this region it encounters a predominantly barrier-like impurity potential. Despite this repulsive landscape, the exciton remains confined within the moving SAW minimum, and crosses the impurity region without significant loss of coherence. In the reference frame co-moving with the SAW, this behavior is evidenced by the persistence of a narrow, high-density stripe that remains continuously aligned with the initial SAW valley throughout the interaction (as highlighted by the violet rectangles in the figure). In the laboratory frame, this corresponds to a tunneling process in which the CoM motion remains phase-coherent and locked to the SAW potential. Any weak probability density spreading into neighboring valleys is strongly suppressed, remains transient, and does not lead to irreversible leakage or fragmentation of the wave packet.

The corresponding $\rho_{\mathrm{cm}}(X_{\mathrm{cm}})$ profile in panel (b), evaluated at $t = 330$ ps, when the impurity potential is at the SAW valley of the exciton in the comoving frame of the SAW, provides a quantitative confirmation of this behavior. The green curve shows two pronounced peaks within the initial SAW valley, confirming strong transmission. The vertical pink dashed line marks the impurity position, while the blue and red curves represent the total potential evaluated at two representative values of the relative coordinate, $x_r = 0$ and $x_r = 25$ nm, respectively, rescaled for comparison. Arrows indicate the alignment between the density maximum and predominantly barrier-like potential features.

Notable oscillations of the transmitted density peak are visible in the time-dependent wave-packet evolution of $\rho_{\mathrm{cm}}(X_{\mathrm{cm}})$. These oscillations reflect a coherent dynamical modulation of the CoM motion induced by the impurity. No substantial density accumulates outside the SAW valley, and exciton dissociation remains negligible in this regime. This regime is therefore identified as tunneling-dominated.

When the impurity is placed near the electron layer (Fig. 5.3), the wave-packet evolution in panel (a) exhibits a qualitatively different behavior. The spatial region marked by the black rectangle now correspond to a potential with strong impurity-induced negative distortion. As discussed in the previous section, when the wave packet traverses this region it encounters a

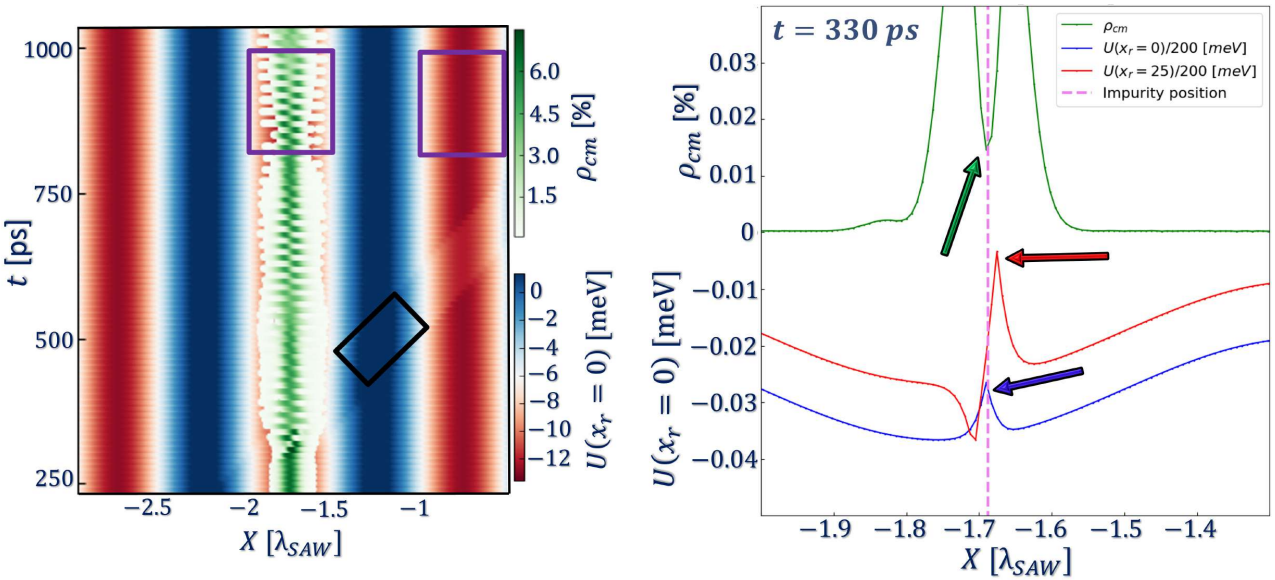

(a) Wave-packet evolution

(b) ρ_{cm} profile

Figure 5.2: Wave-packet dynamics and external potential for a SAW-driven SIX interacting with a localized positive impurity in the hole layer. Panel (a) shows the spatiotemporal evolution of the CoM marginal density $\rho_{\mathrm{cm}}(X_{\mathrm{cm}}, t)$ (green color map), overlaid on the total external potential in the SAW co-moving frame (red–blue background, with red indicating higher and blue lower potential energy). The black rectangle highlights a spatial region where the impurity induces a strong positive distortion of the SAW potential. The violet rectangles highlight that the exciton remains at the initial SAW valley over extended times. Panel (b) shows the corresponding CoM marginal density at $t = 330$ ps. The green curve represents the transmitted ρ_{cm} profile, while the blue and red curves show the total potential evaluated at representative values of the relative coordinate (e.g. $x_r = 0$ and $x_r = 25$ nm), rescaled for comparison. The vertical dashed line marks the impurity position. Arrows indicate the correspondence between local maxima of the exciton density and barrier-like features due to the impurity potential.

predominantly well-like impurity potential.

In contrast to the hole-layer configuration, the wave packet entering the long-time region progressively loses its valley-guided structure. In the co-moving frame of the SAW, the high-density stripe characteristic of coherent SAW-driven transport becomes strongly attenuated within the initial SAW valley, while a substantial fraction of the probability density accumulates in the neighboring valley toward the impurity (as indicated by the violet rectangles in the figure). In the laboratory frame, the former process is a signature of reduced transmission, whereas the latter indicates trapping induced by the impurity.

Oscillatory features in the time-dependent wave packet are strongly suppressed, reflecting the loss of coherent center-of-mass motion. While some population is still in the initial SAW valley, the dominant effect is temporary confinement near the impurity. This regime is therefore identified as trapping-dominated.

This behavior is confirmed quantitatively by the $\rho_{\mathrm{cm}}(X_{\mathrm{cm}})$ profile shown in panel (b). The green curve displays a strongly reduced peak. In this configuration, the attractive interaction between the impurity and the electron generates a deep potential feature that confines the

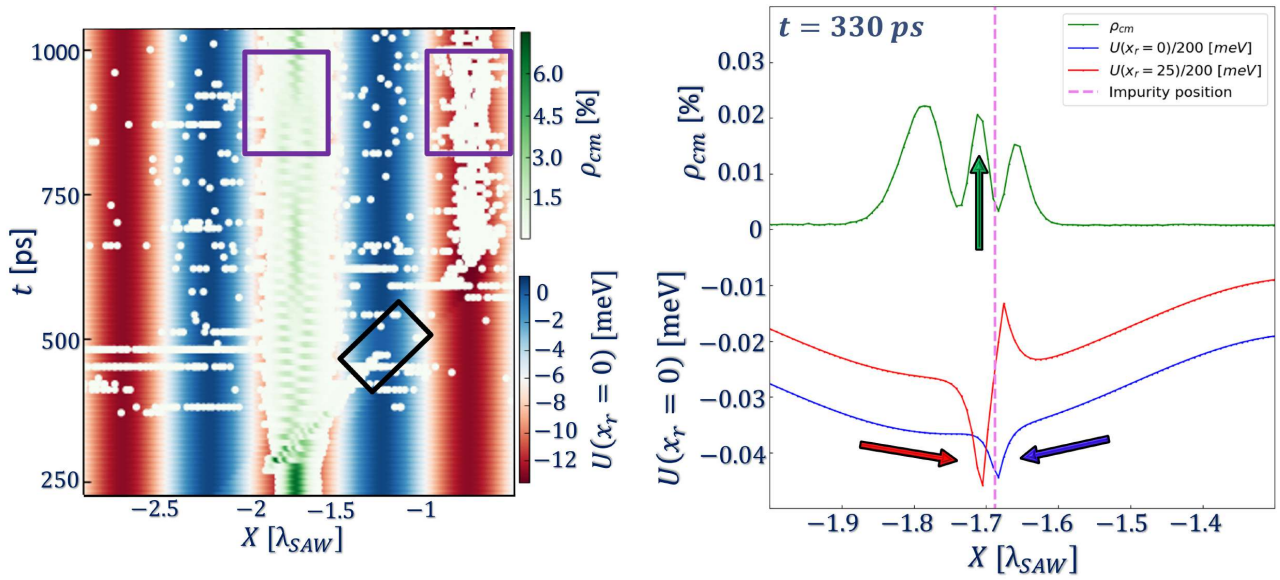

(a) Wave-packet evolution

(b) ρ_{cm} profile

Figure 5.3: Wave-packet dynamics and external potential for a SAW-driven SIX interacting with a localized impurity near the electron layer ($z_{\mathrm{imp}} = 20$ nm, $y_{\mathrm{imp}} = 20$ nm). Panel (a) shows the spatiotemporal evolution of the CoM marginal density $\rho_{\mathrm{cm}}(X_{\mathrm{cm}}, t)$ (green color map), overlaid on the total external potential in the SAW co-moving frame (red–blue background, with red indicating lower and blue higher potential energy). The black rectangle highlights a spatial region where the impurity induces a strong negative distortion of the SAW potential. The violet rectangles at extended times highlight that the exciton is trapped in a SAW valley different from the initial one. Panel (b) shows the corresponding CoM marginal density at $t = 330$ ps. The green curve represents the transmitted ρ_{cm} profile, while the blue and red curves show the total potential evaluated at representative values of the relative coordinate (e.g. $x_r = 0$ and $x_r = 25$ nm), rescaled for comparison. The vertical dashed line marks the impurity position. Arrows indicate the correspondence between local maxima of the exciton density and well-like features of the potential due to the impurity.

exciton CoM near the impurity for extended times. The arrows highlight the spatial match between the trapped density and the potential minimum.

A distinct regime emerges when the impurity is located at the mid-plane between the electron and hole layers (Fig. 5.4). The spatial region marked by the black rectangle now correspond to a potential with small impurity-induced distortion. As discussed in the previous section, when the wave packet traverses this region it encounters a mixed barrier/well-like impurity potential.

Unlike the hole-layer case, the wave packet does not traverse the impurity region coherently in the initial SAW valley. At the same time, in contrast to the electron-layer configuration, the dynamics are not dominated by confinement in another SAW valley. Instead, the density rapidly loses its valley-guided structure and spreads over multiple SAW valleys (as highlighted by the violet rectangle), signaling the activation of dissociation processes that progressively disrupt the bound electron-hole pair.

The dissociation-dominated nature of the dynamics is clearly reflected in the corresponding

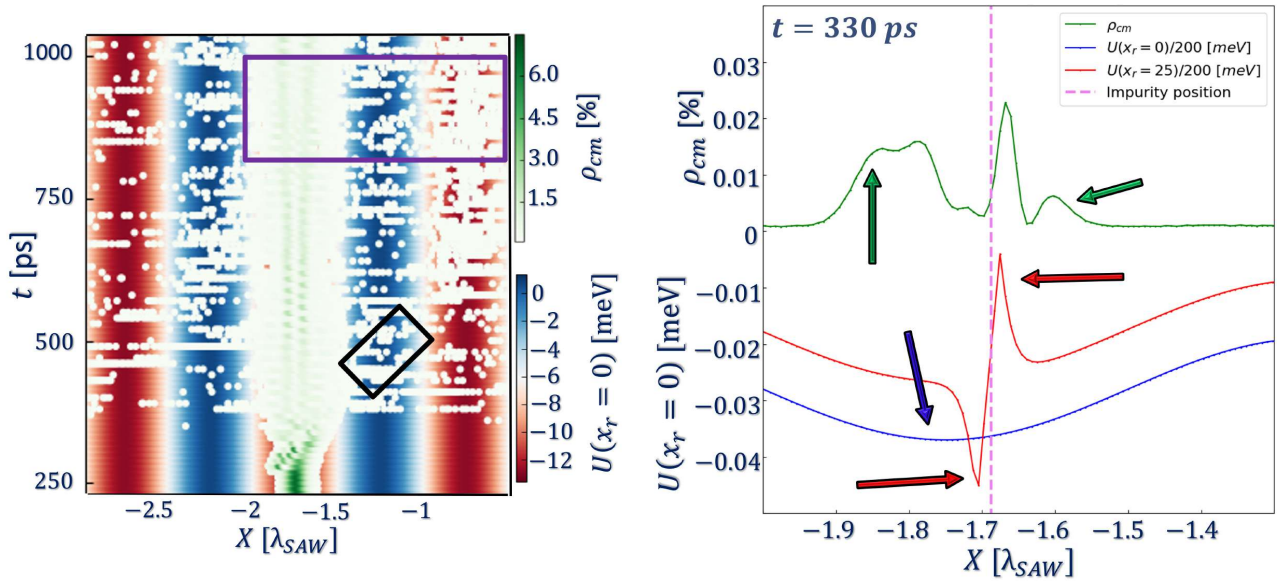

(a) Wave-packet evolution

(b) ρ_{cm} profile

Figure 5.4: Wave-packet dynamics and corresponding CoM marginal density for a SAW-driven SIX interacting with a localized impurity located at the mid-plane between the electron and hole layers ($z_{\mathrm{imp}} = 0$, $y_{\mathrm{imp}} = 20$ nm). Panel (a) shows the spatiotemporal evolution of the CoM marginal density $\rho_{\mathrm{cm}}(X_{\mathrm{cm}}, t)$ (green color scale), overlaid on the total potential in the SAW co-moving frame (red–blue background, with red indicating lower and blue higher potential energy). A black rectangle highlights a region weakly disturbed by the impurity potential. The violet rectangle highlights that the exciton is dissociated over the SAW landscape at extended times. Panel (b) shows the corresponding CoM marginal density at $t = 330$ ps. The green curve represents the transmitted ρ_{cm} profile, while the blue and red curves show the total potential evaluated at representative values of the relative coordinate (e.g. $x_r = 0$ and $x_r = 25$ nm), rescaled for comparison. The vertical dashed line marks the impurity position. Arrows indicate the correspondence between local maxima of the exciton density and mixed barrie/well-like features of the potential due to the impurity.

$\rho_{\mathrm{cm}}(X_{\mathrm{cm}})$ profile shown in panel (b). The green curve exhibits a strongly reduced peak together with a pronounced redistribution of density. Although the potential nearly vanishes for $x_r \simeq 0$, the arrows indicate that the density probes configurations with finite relative separation, where the impurity interaction becomes appreciable.

This behavior for a mid-plane impurity is particularly non-trivial. Within the mean-field rigid-exciton (RIX) model (see Subsec. 2.2.2), one instead obtain a very coherent density, with high long-time probabilities in the initial SAW valley (not shown for clarity), since the impurity-induced potential is minimal near $x_r = 0$, where the internal ground-state wave function $\phi_0(x_r)$ is maximal. The stark contrast with the suppressed transmission observed in the fully correlated model, together with the pronounced redistribution of probability density, therefore provides direct evidence of correlation-driven dissociation.

Taken together, these results demonstrate that barrier-like impurity features favor tunneling-dominated transport, well-like features promote trapping, and mixed barrier/well landscapes activate correlation-driven dissociation.

5.5 Transmission coefficient

To quantify the transport regimes identified from the wave-packet dynamics, we now analyze the transmission coefficient T as a function of the impurity position. In the frame co-moving with the SAW, it is defined as the long-time probability for the exciton center of mass to remain within the SAW valley associated with the initial wave packet (see Eq. (2.64)). This quantity provides a compact, global measure of the impact of impurity-induced scattering on SAW-driven exciton transport.

Figure 5.5 summarizes the dependence of exciton transmission on the impurity geometry and provides a quantitative counterpart to the dynamical regimes discussed in Section 5.4.

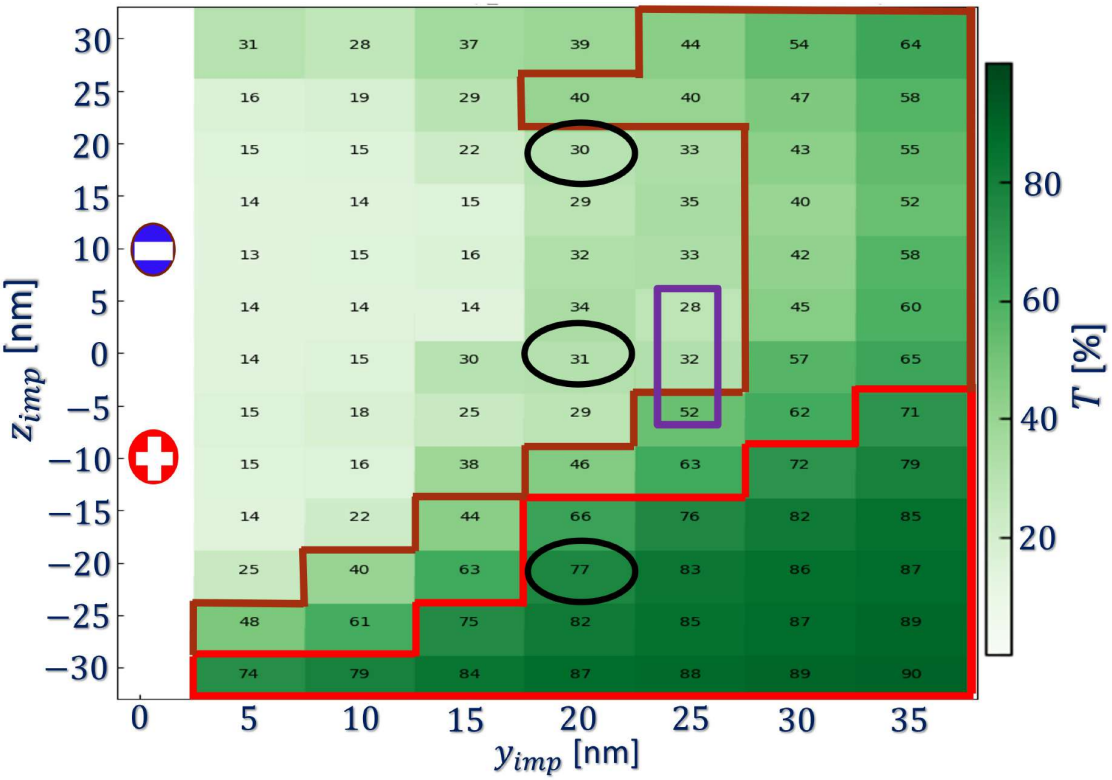

Figure 5.5: Transmission coefficient T (in percent) of a SAW-driven SIX as a function of the transverse position y_{imp} and the growth-direction coordinate z_{imp} of a positive impurity. The color scale encodes the transmission probability, while the numerical values indicate the corresponding percentage at each impurity position. A pronounced asymmetry with respect to z_{imp} is observed even at the same transverse position (black circles and violet square). High transmission occurs for impurities located closer to the hole layer (red region), whereas strong suppression is found for mid-plane and electron-layer configurations (brown and uncolored regions). This asymmetry arises from correlation-driven coupling between internal and center-of-mass degrees of freedom. The map is almost perfectly inverted upon inversion of the impurity charge.

A pronounced asymmetry with respect to the impurity position along the growth direction z_{imp} is observed, even at fixed transverse position y_{imp}. Importantly, this asymmetry cannot be attributed to trivial single-particle effects. In particular, it does not originate from the

small difference between the electron and hole effective masses, $\Delta m^* = m_h - m_e$, nor from the kinetic contribution K in the Hamiltonian, which was explicitly verified to have only a minor quantitative influence on the transmission (not shown for clarity).

Instead, the emergence of distinct regimes of transmission or dissociation is governed by the correlated internal dynamics of the electron–hole pair and by their coupling to the center-of-mass motion induced by the impurity. This is demonstrated by comparison with a rigid-exciton (RIX) model, in which the internal electron–hole dynamics are frozen and the impurity-induced potential yields transmission probabilities that remain close to $T \simeq 100\%$ over the entire explored parameter space of y_{imp} and z_{imp} (not shown for clarity).

By contrast, the fully correlated two-body treatment reveals a much richer and strongly asymmetric behavior. Regions of high transmission are associated with tunneling-dominated wave-packet dynamics (red regions in Fig. 5.5), whereas intermediate and low transmission occurs in regimes characterized by trapping or strong dissociation (brown and uncolored regions in Fig. 5.5). In particular, the pronounced suppression of transmission observed for mid-plane and electron-layer impurity configurations differs by factors ranging from three to eight compared to the RIX prediction, providing direct evidence that electron–hole correlations are essential for capturing the observed transport behavior.

A further key insight provided by Fig. 5.5 is that the asymmetry of the transmission with respect to z_{imp} is also intimately linked to the spatial distribution of charge within the exciton. The impurity couples with different strength to the electron and the hole depending on its position along the growth direction. Consistently, upon inversion of the impurity charge, the transmission map is found to be almost perfectly inverted with respect to z_{imp} (not shown for clarity). This demonstrates that while electron–hole correlations enable the asymmetry to emerge, the relative location of high- and low-transmission regions is ultimately controlled by the charge distribution within the coupled quantum wells.

5.6 Conclusions

In this chapter, we have presented a fully correlated theoretical study of surface-acoustic-wave-driven transport of a spatially indirect exciton in coupled quantum wells in the presence of localized electrostatic impurities. By propagating the full two-particle electron–hole wave function in the frame co-moving with the SAW, we have explicitly resolved the interplay between internal excitonic dynamics and CoM motion, which becomes essential whenever translational symmetry is broken.

Our analysis shows that the relative position of an impurity with respect to the electron and hole layers provides a useful theoretical parameter for disentangling the mechanisms that govern exciton transport. Depending on whether the impurity couples preferentially to the hole layer, to the electron layer, or approximately symmetrically to both carriers, qualitatively distinct dynamical regimes emerge. When the impurity is located near the hole layer, transport proceeds via a tunneling-dominated mechanism characterized by strong transmission, coherent oscillatory motion within the SAW valley, and negligible exciton dissociation. In contrast, impurities close to the electron layer give rise to trapping-dominated dynamics, where the exciton is temporarily confined near the impurity, transmission is strongly reduced, and coherent transport is largely suppressed. The most non-trivial behavior is observed for mid-plane impurity configurations, where dissociation-dominated dynamics emerge despite the near-vanishing impurity potential

for configurations close to the internal ground state. This regime is marked by a strong spread of probability density, minimal transmission, and efficient activation of internal excitations.

By comparing the exact two-body dynamics with the predictions of a rigid-exciton approximation, we have shown that simplified descriptions fail precisely in the regimes where transport is most strongly influenced by realistic scattering centers. While the rigid model predicts nearly perfect transmission across the entire parameter space, the full correlated treatment reveals sharp transitions between tunneling, trapping, and dissociation regimes. This discrepancy provides direct evidence that electron–hole correlations, rather than single-particle effects such as the electron–hole mass difference or kinetic contributions, dominate the transport outcome.

The transmission maps further highlight the central role of charge distribution in governing exciton–impurity interactions. The pronounced asymmetry of the transmission coefficient with respect to the impurity position along the growth direction cannot be explained by mass asymmetry alone, but instead reflects the correlated response of the composite exciton to localized electrostatic fields. The inversion of the transmission pattern upon inversion of the impurity charge underscores that transport is controlled by how the impurity couples to the internal charge configuration of the exciton.

Overall, this chapter establishes that SAW-driven indirect excitons provide a sensitive probe of correlation-driven transport phenomena in semiconductor nanostructures subject to scattering with impurities. Although the microscopic properties of individual scattering centers are generally not tunable in experiments, the present results clarify how different impurity configurations translate into distinct transport outcomes. Beyond its relevance for CQW-based excitonic platforms, the theoretical framework developed here provides a general paradigm for interpreting correlated transport of composite quantum particles in dynamically driven and disordered environments.

Chapter 6

General conclusions and future work

This thesis has investigated the role of excitonic couplings in shaping optical, reactive, and transport phenomena across hybrid and semiconductor nanostructures. By focusing on three representative platforms -chromophore–quantum dot nanohybrids, photoswitch–quantum dot nanohybrids, and coupled quantum wells with surface acoustic waves— this work has developed a unified excitonic perspective that bridges such distinct physical systems.

A central conclusion emerging from this study is that correlated excitonic descriptions are essential for capturing both static hybridization and dynamical transport effects in nanoscale systems. Across all investigated platforms, these correlation-driven couplings provide the mechanism through which geometry, material parameters, and external fields translate into functional control. In contrast, mean-field or perturbative approaches tend to neglect such couplings and are therefore likely to become inadequate in regimes dominated by resonance conditions or strong Coulomb interactions.

The Hybrid Configuration Interaction (HyCI) framework was applied at its full theoretical scope for the first time through explicit construction and diagonalization of the complete hybrid Hamiltonian. In the prototypical H_2P–GaN quantum dot nanohybrid, correlated hybrid excitons emerge naturally under near-resonant conditions, producing avoided crossings in the excitation spectrum with an exchange of molecular and nanoparticle character that provides a clear physical signature of excitonic mixing. The hybridization strength is highly tunable with quantum dot size, molecular orientation, and inter-fragment separation, with energy splittings largely governed by dipolar near-field interactions and deviations arising from higher-order multipolar contributions and optically dark quantum-dot states. A systematic convergence analysis establishes the HyCI approach as numerically robust and accurate with respect to basis-set and multipolar truncation.

By leveraging the HyCI framework, a cavity-free, exciton-driven mechanism for controlling photoisomerization in nanohybrids composed of a photoswitch and a quantum dot was introduced for the first time. In the azobenzene-CdSe system, intrinsic excitonic coupling between the lowest molecular excitation and the first bright quantum-dot exciton induces avoided crossings on the excited-state potential energy surfaces along the photoisomerization coordinate, generating energy splittings on the order of a few meV and a redistribution of oscillator strength between molecular and quantum-dot contributions. The hybridization was shown to be tunable with QD size, molecular orientation, and inter-fragment separation, and to operate on nanosecond electronic timescales compatible with photoisomerization, thereby establishing

intrinsic excitonic coupling as a viable and conceptually distinct route for modulating photochemical pathways in hybrid nanostructures.

In the presence of screened electrostatic impurities and within a fully correlated two-body description, a unified treatment of the transport of spatially indirect excitons driven by surface acoustic waves in coupled quantum wells was provided. The results in GaAs/AlGaAs reveal distinct transport regimes and pronounced asymmetries in the transmission of indirect excitons, where the impurity can either weakly perturb or strongly suppress SAW-driven transport, depending on its position relative to the electron and hole layers. A comparison with a reduced mean-field description demonstrates that correlation-driven coupling between internal and center-of-mass degrees of freedom is essential to this behavior in semiconductor nanostructures.

Taken together, the results of this thesis demonstrate that correlated excitons constitute the unifying physical principle governing hybridization, photochemical control, and transport in a broad class of nanostructures. By combining multiscale electronic-structure methods with explicit correlation and time-dependent propagation, this work advances the theoretical foundations required to understand and design excitonic functionality beyond simplified or mean-field descriptions.

The theoretical predictions presented in this work are, in principle, accessible to experimental verification in several classes of hybrid and semiconductor nanostructures. In nanohybrids, absorption and photoluminescence spectroscopy (particularly photoluminescence-excitation measurements) [180, 181, 182] together with size-tunable quantum dots, controlled molecular geometries, and well-defined inter-fragment distance provide realistic routes to probe the hybrid splittings and the redistribution of oscillator strength described here. In coupled-quantum-well platforms, surface-acoustic-wave-driven transport combined with time-resolved photoluminescence and electrostatically defined potential landscapes [134, 183] enables direct comparison with the correlation-driven transport regimes identified in this thesis.

Several directions for future work naturally follow from these findings. On the methodological side, incorporating nuclear dynamics and nonadiabatic couplings into the HyCI framework would enable direct simulations of photoisomerization dynamics and a more complete treatment of regions near conical intersections, while extensions to multi-exciton regimes could clarify how strong optical excitation modifies hybridization. On the materials side, the approach could be generalized to hybrid architectures involving plasmonic nanoparticles, including non-spherical nanostructures, as well as to aggregates of quantum dots, molecular dyes, or mixed assemblies, where collective excitations and long-range Coulomb interactions are expected to play a central role. In this context, systematically going beyond the dipolar approximation for the molecular degrees of freedom would allow the role of higher-order molecular multipoles and symmetry effects to be assessed. Finally, extending the correlated exciton framework to more complex transport settings —including broader impurity landscapes and two-dimensional materials— would open the way to modeling increasingly functional nanoscale devices.

In conclusion, this thesis has shown that a correlation-aware, exciton-based theoretical framework provides both a coherent conceptual picture and a quantitatively reliable tool for investigating hybrid and semiconductor nanostructures. By elucidating how excitonic correlations can be harnessed for control across different physical platforms, the work lays the groundwork for future theoretical and experimental advances in excitonic nanoscience.

Appendices

Appendix A

Matrix elements involving spherical envelope functions

A.1 Two-particle Coulomb integrals with polarization effects

This appendix summarizes the evaluation of the two-particle matrix elements of the renormalized electron-hole interaction entering into the single-exciton Full-CI Hamiltonian [see Eq. (2.20)]. Starting from Eq. (2.21), we employ the spherical-harmonics identity [184]

$$P_\ell(\cos\Theta) = \frac{4\pi}{2\ell+1}\sum_{m=-\ell}^{\ell} Y_{\ell m}(\Omega)\, Y^*_{\ell m}(\Omega'), \tag{A.1}$$

which leads to the following expression for the two-particle matrix elements:

$$\langle 12|\hat{V}_{\rm ren}|34\rangle = \frac{4\pi}{\varepsilon_{\rm QD}}\sum_{\ell=0}^{\infty}\frac{1}{2\ell+1}\sum_{m=-\ell}^{\ell}\left[\left\langle 12\left|\frac{r_<^\ell}{r_>^{\ell+1}}Y_{\ell m}(\Omega_e)\, Y^*_{\ell m}(\Omega_h)\right|34\right\rangle + \frac{\alpha_\ell}{R_{\rm QD}^{2\ell+1}}\left\langle 12\left|(r_e r_h)^\ell Y_{\ell m}(\Omega_e)\, Y^*_{\ell m}(\Omega_h)\right|34\right\rangle\right], \tag{A.2}$$

where $\alpha_\ell = \frac{(\ell+1)(\varepsilon-1)}{1+\ell(\varepsilon+1)}$. Applying the kernel decomposition

$$\frac{r_<^\ell}{r_>^{\ell+1}} = \Theta(r_e - r_h)\frac{r_h^\ell}{r_e^{\ell+1}} + \Theta(r_h - r_e)\frac{r_e^\ell}{r_h^{\ell+1}}, \tag{A.3}$$

with Θ the Heaviside function, and employing the dominant envelope-function approximation $\langle i|\, r^\ell Y_{\ell m}(\Omega)\,|j\rangle \approx \langle f_i|\, r^\ell Y_{\ell m}(\Omega)\,|f_j\rangle$, [12] we obtain

$$\langle 12|\hat{V}_{\rm ren}|34\rangle = \frac{4\pi}{\varepsilon_{\rm QD}}\sum_{\ell=0}^{\infty}\frac{\mathcal{R}_\ell^{\rm bare}(13;24) + \alpha_\ell\mathcal{R}_\ell^{\rm pol}(13;24)}{2\ell+1}\sum_{m=-\ell}^{\ell}\mathcal{A}_{13}^{(\ell m)}\,\mathcal{A}_{24}^{(\ell m)}. \tag{A.4}$$

Here, the bare radial integral reads

$$\begin{aligned}\mathcal{R}_\ell^{\text{bare}}(13;24) = &\int_0^{R_{\text{QD}}} dr\; R^*_{n_1 l_1}(r)\, R_{n_3 l_3}(r)\, r^{\,\ell+2} \int_r^{R_{\text{QD}}} dr'\; R^*_{n_2 l_2}(r')\, R_{n_4 l_4}(r')\, r'^{-\ell+1} \\ &+ \int_0^{R_{\text{QD}}} dr\; R^*_{n_2 l_2}(r)\, R_{n_4 l_4}(r)\, r^{\,\ell+2} \int_r^{R_{\text{QD}}} dr'\; R^*_{n_1 l_1}(r')\, R_{n_3 l_3}(r')\, r'^{-\ell+1},\end{aligned} \tag{A.5}$$

the polarization contribution takes the form

$$\mathcal{R}_\ell^{\text{pol}}(13;24) = \frac{1}{R_{\text{QD}}^{2\ell+1}} \left[\int_0^{R_{\text{QD}}} dr\; R^*_{n_1 l_1}(r)\, R_{n_3 l_3}(r)\, r^{\,\ell+2}\right] \left[\int_0^{R_{\text{QD}}} dr'\; R^*_{n_2 l_2}(r')\, R_{n_4 l_4}(r')\, r'^{\,\ell+2}\right], \tag{A.6}$$

and the angular integrals are given by

$$\mathcal{A}_{13}^{(\ell m)} = \int d\Omega\; Y^*_{l_1 m_1}(\Omega)\, Y_{l_3 m_3}(\Omega)\, Y_{\ell m}(\Omega), \qquad \mathcal{A}_{24}^{(\ell m)} = \int d\Omega'\; Y^*_{l_2 m_2}(\Omega')\, Y_{l_4 m_4}(\Omega')\, Y^*_{\ell m}(\Omega'). \tag{A.7}$$

Radial integrals are computed numerically using Simpson's rule. [165] The angular integrals, however, can be cast into analytical forms, as presented below.

A.1.1 Gaunt coefficients, Wigner $3j$ symbols and selection rules

The angular integrals in Eq. (A.7) are standard Gaunt coefficients and can be written analytically in terms of Wigner $3j$ symbols as [184]

$$\mathcal{A}_{13}^{(\ell m)} = (-1)^{m_1} \left(\frac{(2l_1+1)(2l_3+1)(2\ell+1)}{4\pi}\right)^{1/2} \begin{pmatrix} l_1 & l_3 & \ell \\ 0 & 0 & 0 \end{pmatrix} \begin{pmatrix} l_1 & l_3 & \ell \\ -m_1 & m_3 & m \end{pmatrix}, \tag{A.8}$$

$$\mathcal{A}_{24}^{(\ell m)} = (-1)^{m_2+m} \left(\frac{(2l_2+1)(2l_4+1)(2\ell+1)}{4\pi}\right)^{1/2} \begin{pmatrix} l_2 & l_4 & \ell \\ 0 & 0 & 0 \end{pmatrix} \begin{pmatrix} l_2 & l_4 & \ell \\ -m_2 & m_4 & -m \end{pmatrix}. \tag{A.9}$$

Here $\begin{pmatrix} j_1 & j_2 & j_3 \\ m_1 & m_2 & m_3 \end{pmatrix}$ denotes a Wigner $3j$ symbol. [184] These symbols are non-zero only if the following conditions are simultaneously satisfied:

$$\begin{cases} m_1 + m_2 + m_3 = 0, \\ j_1 + j_2 + j_3 \in \mathbb{Z}, \\ |m_i| \le j_i, \qquad \forall\, i, \\ |j_i - j_j| \le j_k \le j_i + j_j, \qquad \forall\, (i \neq j \neq k) \text{ and its cyclic permutations.} \end{cases} \tag{A.10}$$

Together, these relations define the selection rules associated with spherical symmetry. In particular, they ensure the exact truncation of the infinite ℓ-summation in Eq. (A.4), with the allowed values of ℓ restricted to $\max(|l_1 - l_3|, |l_2 - l_4|) \le \ell \le \min(l_1 + l_3, l_2 + l_4)$.

A.2 Integrals of the spherical-multipole function and its gradient

The spherical multipole moments in Eq.(2.38) are readily obtained from its definition,

$$\langle 1|r^{\,\ell}Y_{\ell m}(\Omega)|2\rangle = \int_0^{R_{\rm QD}} \mathrm{d}r\; R^*_{n_1 l_1}(r)\, R_{n_2 l_2}(r)\, r^{\,l+2} \int \mathrm{d}\Omega\, Y^*_{l_1 m_1}(\Omega)\, Y_{l_2 m_2}(\Omega)\, Y_{\ell m}(\Omega), \tag{A.11}$$

where the angular part of the integral is a Gaunt coefficient analogous to the one in (A.8).

The matrix elements of spherical-multipole gradient $\nabla\big(r^{\,\ell}Y_{\ell m}(\Omega)\big)$ can be computed in a similar way. In this thesis, we are only concerned with its z-component, $F^z_{\ell m} \equiv \mathbf{e}_z\cdot\nabla\big(r^{\,\ell}Y_{\ell m}(\Omega)\big)$. Following the derivation in Ref.12, one obtains:

$$\big\langle 1\big|F^z_{\ell m}\big|2\big\rangle = \int_0^{R_{\rm QD}} \mathrm{d}r\; R^*_{n_1 l_1}(r)\, R_{n_2 l_2}(r)\; r^{\,\ell+1}\; \times I_{\ell m}(1,2), \tag{A.12}$$

where the angular integral $I_{\ell m}(1,2)$ is given by:

$$\begin{aligned} I_{\ell m}(1,2) = (-1)^{m_1}&\left[\frac{(2l_1+1)(2l_2+1)}{4\pi}\right]^{1/2}(2\ell+1)^{1/2} \\ &\times \sum_{l'm'}(2l'+1)(-1)^{m'}\begin{pmatrix} l_1 & l_2 & l' \\ 0 & 0 & 0\end{pmatrix}\begin{pmatrix} l_1 & l_2 & l' \\ -m_1 & m_2 & -m'\end{pmatrix}\begin{pmatrix} 1 & \ell & l' \\ 0 & 0 & 0\end{pmatrix} \\ &\times\left\{(\ell-m)\begin{pmatrix} 1 & \ell & l' \\ 0 & m & -m'\end{pmatrix} - \sqrt{2(\ell+m+1)(\ell-m)}\begin{pmatrix} 1 & \ell & l' \\ -1 & m+1 & -m'\end{pmatrix}\right\}. \end{aligned}$$

Here, the Wigner $3j$ symbols impose selection rules (see Eq. (A.10)) on the angular momentum index ℓ and magnetic index m. In particular, the multipole expansion in Eq. (2.36) reduces to a finite sum, with the allowed values of ℓ restricted to $|l'-1| \le \ell \le l'+1$ with $|l_1-l_2| \le l' \le l_1+l_2$.

All radial integrals in this section are evaluated numerically by using Simpson's rule. [165]

A.3 Dipole moments and overlaps

Following the derivation in Ref.12, the dipole matrix element factorizes into radial and angular parts as

$$\langle 1|\mathbf{r}|2\rangle = \left(\frac{\pi}{3}\right)^{1/2}\left[\int_0^{R_{\rm QD}} dr R_{n_1 l_1}(r) R_{n_2 l_2}(r)\, r^3\right]\mathbf{I}, \tag{A.13}$$

where the angular integral $\mathbf{I}$ is given in closed form by

$$\begin{aligned} \mathbf{I} = \frac{\sqrt{2}}{2}(-1)^{m_1}&\begin{pmatrix} l_1 & l_2 & 1 \\ 0 & 0 & 0\end{pmatrix}\Bigg[(\mathbf{e}_x + i\mathbf{e}_y)\begin{pmatrix} l_1 & l_2 & 1 \\ -m_1 & m_2 & -1\end{pmatrix} \\ &+ (i\mathbf{e}_y - \mathbf{e}_x)\begin{pmatrix} l_1 & l_2 & 1 \\ -m_1 & m_2 & 1\end{pmatrix} \\ &+ \sqrt{2}\,\mathbf{e}_z\begin{pmatrix} l_1 & l_2 & 1 \\ -m_1 & m_2 & 0\end{pmatrix}\Bigg]. \end{aligned} \tag{A.14}$$

Here, the Wigner $3j$ symbols enforce the usual electric-dipole selection rules: opposite parity ($\Delta l = \pm 1$), $\Delta m = 0, \pm 1$, and the triangular conditions on the angular momenta.

The overlap integral between two one-particle states reads

$$\langle 1|2\rangle = \delta_{l_1 l_2}\, \delta_{m_1 m_2} \int_0^{R_{\mathrm{QD}}} dr\, R_{n_1 l_1}(r)\, R_{n_2 l_2}(r)\, r^2, \tag{A.15}$$

where the Kronecker deltas account for the orthonormality of the spherical harmonics.

All radial integrals appearing in this section are computed numerically using Simpson's rule. [165]

Appendix B

Adiabatic transition probability at avoided crossings

Adiabatic transitions at avoided crossings discussed in Section 4.5 are estimated using the standard two–state Landau–Zener (LZ) model. [178] In this framework, nuclear motion along a generalized coordinate drives the system through the vicinity of a diabatic crossing between two uncoupled electronic states, while a finite electronic coupling opens an avoided crossing and enables population transfer between the diabatic characters, which corresponds to an adiabatic transition between the resulting adiabatic states.

For a single passage through the crossing, the probability of following the adiabatic branch is given by

$$P_{\text{adiab}} = 1 - \exp(-2\pi\Gamma_{LZ}), \tag{B.1}$$

where the dimensionless Γ_{LZ} parameter is defined as

$$\Gamma_{LZ} = \frac{|V(\phi_\times)|^2}{v_\phi \, |\Delta F_\phi|}. \tag{B.2}$$

Here, ϕ denotes the nuclear reaction coordinate, $\phi_\times$ is the diabatic crossing point, $V(\phi_\times)$ is the electronic coupling evaluated at the crossing, v_ϕ is the nuclear speed along the reaction coordinate at the crossing, and ΔF_ϕ is the difference between the slopes of the two diabatic (uncoupled) PESs.

In the present AZB case, the reaction coordinate is chosen as the CNNC dihedral angle ϕ. All potential energy values $E(\phi)$ entering the LZ analysis correspond to HyCI diabatic PESs, i.e., energies obtained without excitonic coupling between the HyCI product states. The diabatic crossing point $(\phi_\times, E_\times)$ is obtained by locally approximating the two uncoupled PESs as linear functions of ϕ and computing their intersection,

$$E_1(\phi_\times) = E_2(\phi_\times) \equiv E_\times, \tag{B.3}$$

which represents the crossing that would occur in the absence of excitonic coupling.

The difference between the diabatic slopes entering Eq. (B.2) is defined as

$$\Delta F_\phi = \left| \left.\frac{dE_1}{d\phi}\right|_{\phi_\times} - \left.\frac{dE_2}{d\phi}\right|_{\phi_\times} \right|, \tag{B.4}$$

and is evaluated numerically by using the slopes of the locally linear functions that approximate the two uncoupled PES branches in the immediate vicinity of $\phi_\times$.

The nuclear speed v_ϕ along the dihedral reaction coordinate at the crossing is modeled as a rigid rotational motion around a fixed molecular axis passing through the N=N bond in AZB. The effective moment of inertia is constructed as

$$I_{\text{eff}} = \sum_A m_A r_{\perp,A}^2, \tag{B.5}$$

where m_A is the mass of atom A and $r_{\perp,A}$ is its perpendicular distance from the chosen rotation axis. Atomic positions are taken from ground-state geometry calculations of AZB at $\phi_\times$. The rotational kinetic energy available at the crossing is computed as

$$E_{\text{kin}} = E_{\text{init}} - E_\times, \tag{B.6}$$

where E_{init} is taken as the higher-energy branch of the two HyCI uncoupled PESs at the nearest *cis* or *trans* configuration. The nuclear speed along the reaction coordinate at crossing is finally obtained as

$$v_\phi = \sqrt{\frac{2E_{\text{kin}}}{I_{\text{eff}}}}. \tag{B.7}$$

The electronic coupling $V(\phi)$ between the two diabatic product states is obtained from the HyCI calculations at discrete dihedral angles. Its value at the diabatic crossing, $V(\phi_\times)$, is determined by shape-preserving cubic interpolation [165] of the computed coupling data.

Finally, the coupling $V(\phi_\times)$, the nuclear speed v_ϕ, and the diabatic slope difference ΔF_ϕ are inserted into Eq. (B.2), yielding the adiabatic transition probability through Eq. (B.1).

Bibliography

[1] N.-C. Godja and F.-D. Munteanu, "Hybrid nanomaterials: a brief overview of versatile solutions for sensor technology in healthcare and environmental applications," *Biosensors*, vol. 14, no. 2, p. 67, 2024.

[2] M. Harun-Ur-Rashid and I. Jahan, "Innovative hybrid nanostructures: pioneering advances in modern therapy," *Frontiers in Nanotechnology*, vol. 6, p. 1458894, 2024.

[3] Y.-F. Chou Chau, "Nanophotonic materials and devices: Recent advances and emerging applications," *Micromachines*, vol. 16, no. 8, p. 933, 2025.

[4] D. G. Baranov, M. Wersall, J. Cuadra, T. J. Antosiewicz, and T. Shegai, "Novel nanostructures and materials for strong light–matter interactions," *Acs Photonics*, vol. 5, no. 1, pp. 24–42, 2018.

[5] J. Guan, J.-E. Park, S. Deng, M. J. Tan, J. Hu, and T. W. Odom, "Light–matter interactions in hybrid material metasurfaces," *Chemical Reviews*, vol. 122, no. 19, pp. 15177–15203, 2022.

[6] M. Notomi, "Hybrid nanomaterial–nanophotonics platforms for future photonic integrations," *JSAP Review*, vol. 2023, p. 230208, 2023.

[7] A. Credi, "Quantum dot–molecule hybrids: a paradigm for light-responsive nanodevices," *New Journal of Chemistry*, vol. 36, no. 10, pp. 1925–1930, 2012.

[8] V. P. Ananikov, "Organic–inorganic hybrid nanomaterials," *Nanomaterials*, vol. 9, no. 9, p. 1197, 2019.

[9] A. Abdollahi, H. Roghani-Mamaqani, B. Razavi, and M. Salami-Kalajahi, "Photoluminescent and chromic nanomaterials for anticounterfeiting technologies: recent advances and future challenges," *ACS nano*, vol. 14, no. 11, pp. 14417–14492, 2020.

[10] M. W. Brett, C. K. Gordon, J. Hardy, and N. J. Davis, "The rise and future of discrete organic–inorganic hybrid nanomaterials," *ACS Physical Chemistry Au*, vol. 2, no. 5, pp. 364–387, 2022.

[11] M. Arya, S. Heera, P. Meenu, and K. Deepa, "Organic-inorganic hybrid materials and architectures in optoelectronic devices: Recent advancements," *ChemPhysMater*, vol. 3, no. 3, pp. 252–272, 2024.

[12] G. Gil, *Electronic excitations in hybrid nanosystems*. Ph.D. thesis, University of Modena and Reggio Emilia, https://morethesis.unimore.it/theses/available/etd-02022017-151409/, 2017.

[13] G. Gil, G. Goldoni, and S. Corni, "Enhanced light-harvesting of protein-pigment complexes assisted by a quantum dot antenna," in *Proceedings of the 2018 Nanotechnology for Instrumentation and Measurement (NANOfIM)*, (Mexico City, Mexico), pp. 1–5, IEEE, 2018.

[14] P. Vasa, "Exciton-surface plasmon polariton interactions," *Advances in Physics: X*, vol. 5, no. 1, p. 1749884, 2020.

[15] S. Padgaonkar, C. T. Eckdahl, J. K. Sowa, R. López-Arteaga, D. E. Westmoreland, E. F. Woods, S. Irgen-Gioro, B. Nagasing, T. Seideman, M. C. Hersam, *et al.*, "Light-triggered switching of quantum dot photoluminescence through excited-state electron transfer to surface-bound photochromic molecules," *Nano letters*, vol. 21, no. 1, pp. 854–860, 2021.

[16] L. Cascino, S. Corni, and S. D'Agostino, "Revealing the interplay between hybrid and charge-transfer states in polariton chemistry," *The Journal of Physical Chemistry C*, vol. 128, no. 7, pp. 2917–2927, 2024.

[17] D. Beljonne, C. Curutchet, G. D. Scholes, and R. J. Silbey, "Beyond forster resonance energy transfer in biological and nanoscale systems," *The journal of physical chemistry B*, vol. 113, no. 19, pp. 6583–6599, 2009.

[18] G. Gil, S. Corni, A. Delgado, A. Bertoni, and G. Goldoni, "Excitation energy-transfer in functionalized nanoparticles: Going beyond the förster approach," *The Journal of Chemical Physics*, vol. 144, no. 7, p. 074101, 2016. Erratum:*J. Chem. Phys.* 145, 8 (2016).

[19] G. Gil, S. Corni, A. Delgado, A. Bertoni, and G. Goldoni, "Predicting signatures of anisotropic resonance energy transfer in dye-functionalized nanoparticles," *RSC advances*, vol. 6, no. 106, pp. 104648–104656, 2016.

[20] J. Hu, F. Zhao, H. Ling, Y. Zhang, and Q. Liu, "Single-particle förster resonance energy transfer from upconversion nanoparticles to organic dyes," *Nanoscale Advances*, vol. 6, no. 11, pp. 2945–2953, 2024.

[21] L. G. Feld, S. C. Boehme, V. Morad, Y. Sahin, C. J. Kaul, D. N. Dirin, G. Rainò, and M. V. Kovalenko, "Quantifying forster resonance energy transfer from single perovskite quantum dots to organic dyes," *ACS nano*, vol. 18, no. 14, pp. 9997–10007, 2024.

[22] M. A. Zarbin, C. Montemagno, J. F. Leary, and R. Ritch, "Nanomedicine in ophthalmology: the new frontier," *American journal of ophthalmology*, vol. 150, no. 2, pp. 144–162, 2010.

[23] V. Pawar, P. Maske, A. Khan, A. Ghosh, R. Keshari, M. Bhatt, and R. Srivastava, "Responsive nanostructure for targeted drug delivery," *Journal of Nanotheranostics*, vol. 4, no. 1, pp. 55–85, 2023.

[24] S. Singh and H. Sharma, "Emerging applications of nanotechnology in drug delivery and medical imaging," *Current Radiopharmaceuticals*, vol. 16, no. 4, pp. 269–283, 2023.

[25] P. R. Stoddart, J. M. Begeng, W. Tong, M. R. Ibbotson, and T. Kameneva, "Nanoparticle-based optical interfaces for retinal neuromodulation: a review," *Frontiers in Cellular Neuroscience*, vol. 18, p. 1360870, 2024.

[26] L. Schmermund, V. Jurkas, F. F. Ozgen, G. D. Barone, H. C. Buchsenschutz, C. K. Winkler, S. Schmidt, R. Kourist, and W. Kroutil, "Photo-biocatalysis: biotransformations in the presence of light," *Acs Catalysis*, vol. 9, no. 5, pp. 4115–4144, 2019.

[27] S. Zhou, D. Li, C. Lee, and J. Xie, "Nanoparticle phototherapy in the era of cancer immunotherapy," *Trends in chemistry*, vol. 2, no. 12, pp. 1082–1095, 2020.

[28] Y.-Q. Liu, L.-Y. Qin, H.-J. Li, Y.-X. Wang, R. Zhang, J.-M. Shi, J.-H. Wu, G.-X. Dong, and P. Zhou, "Application of lanthanide-doped upconversion nanoparticles for cancer treatment: A review," *Nanomedicine*, vol. 16, no. 24, pp. 2207–2242, 2021.

[29] W. Zaheer, C. R. McGranahan, J. R. Ayala, K. Garcia-Pedraza, L. J. Carrillo, A. R. Rothfuss, U. Wijethunga, G. Agbeworvi, A. R. Giem, J. L. Andrews, *et al.*, "Photocatalytic hydrogen evolution mechanisms mediated by stereoactive lone pairs of sb2vo5 in quantum dot heterostructures," *Chem Catalysis*, vol. 4, no. 1, p. 100844, 2024.

[30] Q.-B. Zhu, B. Li, D.-D. Yang, C. Liu, S. Feng, M.-L. Chen, Y. Sun, Y.-N. Tian, X. Su, X.-M. Wang, *et al.*, "A flexible ultrasensitive optoelectronic sensor array for neuromorphic vision systems," *Nature communications*, vol. 12, no. 1, p. 1798, 2021.

[31] Z. Chen, G. Luo, J. Ren, Q. Wang, X. Zhao, L. Wei, Y. Wang, Y. Liu, Y. Deng, and S. Li, "Recent advances in and application of fluorescent microspheres for multiple nucleic acid detection," *Biosensors*, vol. 14, no. 6, p. 265, 2024.

[32] T. Mirkovic, E. E. Ostroumov, J. M. Anna, R. Van Grondelle, Govindjee, and G. D. Scholes, "Light absorption and energy transfer in the antenna complexes of photosynthetic organisms," *Chemical reviews*, vol. 117, no. 2, pp. 249–293, 2017.

[33] A. M. Steiner, F. Lissel, A. Fery, J. Lauth, and M. Scheele, "Prospects of coupled organic–inorganic nanostructures for charge and energy transfer applications," *Angewandte Chemie International Edition*, vol. 60, no. 3, pp. 1152–1175, 2021.

[34] O. Kulyk, L. Rocard, L. Maggini, and D. Bonifazi, "Synthetic strategies tailoring colours in multichromophoric organic nanostructures," *Chemical Society Reviews*, vol. 49, no. 23, pp. 8400–8424, 2020.

[35] D. Cappelletti, M. Barbieri, A. Aliprandi, M. Maggini, and L. orević, "Self-assembled π-conjugated chromophores: preparation of one-and two-dimensional nanostructures and their use in photocatalysis," *Nanoscale*, vol. 16, no. 19, pp. 9153–9168, 2024.

[36] A. S. Klymchenko, D. S. Biswas, and P. Didier, "Light-harvesting nanomaterials based on dyes for energy transfer and amplified biosensing," *Advanced Materials*, vol. 37, no. 45, p. e01237, 2025.

[37] G. A. Jones and D. S. Bradshaw, "Resonance energy transfer: from fundamental theory to recent applications," *Frontiers in Physics*, vol. 7, p. 100, 2019.

[38] X. Zhou, S. Lin, and H. Yan, "Interfacing dna nanotechnology and biomimetic photonic complexes: advances and prospects in energy and biomedicine," *Journal of Nanobiotechnology*, vol. 20, no. 1, p. 257, 2022.

[39] Q. Duan, Q. Zhang, J. Zhang, S. Lin, T. Xiao, and L. Wang, "Artificial light-harvesting systems based on supramolecular polymers," *Chinese Chemical Letters*, p. 111421, 2025.

[40] Y. Zhang, K. Ren, L. Wang, L. Wang, and Z. Fan, "Porphyrin-based heterogeneous photocatalysts for solar energy conversion," *Chinese Chemical Letters*, vol. 33, no. 1, pp. 33–60, 2022.

[41] K. Rybicka-Jasinska, T. Wdowik, K. Łuczak, A. J. Wierzba, O. Drapała, and D. Gryko, "Porphyrins as promising photocatalysts for red-light-induced functionalizations of biomolecules," *ACS Organic & Inorganic Au*, vol. 2, no. 5, pp. 422–426, 2022.

[42] S. Chen, J. Wei, X. Ren, K. Song, J. Sun, F. Bai, and S. Tian, "Recent progress in porphyrin/g-c3n4 composite photocatalysts for solar energy utilization and conversion," *Molecules*, vol. 28, no. 11, p. 4283, 2023.

[43] C. Tang, X. Li, Y. Hu, X. Du, S. Wang, B. Chen, and S. Wang, "Porphyrin-based metal-organic framework materials: design, construction, and application in the field of photocatalysis," *Molecules*, vol. 29, no. 2, p. 467, 2024.

[44] K. Ladomenou, M. Natali, E. Iengo, G. Charalampidis, F. Scandola, and A. G. Coutsolelos, "Photochemical hydrogen generation with porphyrin-based systems," *Coordination Chemistry Reviews*, vol. 304, pp. 38–54, 2015.

[45] J. H. Lee, Y. Kim, S. Oh, and W.-D. Jang, "Porphyrin-based nanoporous materials for photocatalytic applications," *Applied Physics Reviews*, vol. 11, p. 031319, 08 2024.

[46] T. Han, S. Wang, G. A. Salazar, and M. A. Rawashdeh-Omary, "Porous porphyrin-based photocatalysts: Recent progress and applications in environmental remediation," *Materials Chemistry Frontiers*, 2025.

[47] M. K. Panda, K. Ladomenou, and A. G. Coutsolelos, "Porphyrins in bio-inspired transformations: Light-harvesting to solar cell," *Coordination Chemistry Reviews*, vol. 256, no. 21-22, pp. 2601–2627, 2012.

[48] J. M. Park, J. H. Lee, and W.-D. Jang, "Applications of porphyrins in emerging energy conversion technologies," *Coordination Chemistry Reviews*, vol. 407, p. 213157, 2020.

[49] N. Tsolekile, S. Nelana, and O. S. Oluwafemi, "Porphyrin as diagnostic and therapeutic agent," *Molecules*, vol. 24, no. 14, p. 2669, 2019.

[50] Y. Lin, T. Zhou, R. Bai, and Y. Xie, "Chemical approaches for the enhancement of porphyrin skeleton-based photodynamic therapy," *Journal of enzyme inhibition and medicinal chemistry*, vol. 35, no. 1, pp. 1080–1099, 2020.

[51] C. Qi, J. Chen, Y. Qu, X. Luo, W. Wang, and X. Zheng, "Recent advances in porphyrin-based covalent organic frameworks for synergistic photodynamic and photothermal therapy," *Pharmaceutics*, vol. 16, no. 12, p. 1625, 2024.

[52] F. Yang, C. Li, Y. Wei, N. Yan, X. Wang, F. Liu, S. You, J. Wang, W. Ma, and W. Li, "A simple, small-bandgap porphyrin-based conjugated polymer for application in organic electronics," *Macromolecular Rapid Communications*, vol. 39, no. 21, p. 1800546, 2018.

[53] P. Zwick, D. Dulić, H. S. Van Der Zant, and M. Mayor, "Porphyrins as building blocks for single-molecule devices," *Nanoscale*, vol. 13, no. 37, pp. 15500–15525, 2021.

[54] S. N. Shet, D. H. Murthy, S. Chandrappa, S. J. Galbao, M. Patil, and V. S. Shetti, "Synthesis, optoelectronic, and photoelectrochemical properties of an azulene-bridged porphyrin dimer," *ACS omega*, 2025.

[55] R. Paolesse, S. Nardis, D. Monti, M. Stefanelli, and C. Di Natale, "Porphyrinoids for chemical sensor applications," *Chemical reviews*, vol. 117, no. 4, pp. 2517–2583, 2017.

[56] G. Magna, F. Mandoj, M. Stefanelli, G. Pomarico, D. Monti, C. Di Natale, R. Paolesse, and S. Nardis, "Recent advances in chemical sensors using porphyrin-carbon nanostructure hybrid materials," *Nanomaterials*, vol. 11, no. 4, p. 997, 2021.

[57] I. Di Filippo, Z. Anfar, G. Magna, P. Pranee, D. Monti, M. Stefanelli, R. Oda, C. Di Natale, and R. Paolesse, "Chiral porphyrin-sio 2 nano helices-based sensors for vapor enantiomers recognition," *Nanoscale Advances*, vol. 6, no. 17, pp. 4470–4478, 2024.

[58] Z. Li, X. Zeng, C. Gao, J. Song, F. He, T. He, H. Guo, and J. Yin, "Photoswitchable diarylethenes: from molecular structures to biological applications," *Coordination Chemistry Reviews*, vol. 497, p. 215451, 2023.

[59] K. Kuntze, J. Isokuortti, J. J. van der Wal, T. Laaksonen, S. Crespi, N. A. Durandin, and A. Priimagi, "Detour to success: photoswitching via indirect excitation," *Chemical Science*, vol. 15, no. 30, pp. 11684–11698, 2024.

[60] D. Villarón, N. Duindam, and S. J. Wezenberg, "Push-pull stiff-stilbene: proton-gated visible-light photoswitching and acid-catalyzed isomerization," *Chemistry–A European Journal*, vol. 27, no. 69, pp. 17346–17350, 2021.

[61] L. Zhao, G. Xu, Y. Guo, H. Zheng, P. Dong, and J. Chen, "The competitive mechanism between photoisomerization and excited state intramolecular proton transfer process of 2-hydroxychalcone system," *Journal of Photochemistry and Photobiology A: Chemistry*, vol. 434, p. 114255, 2023.

[62] S. Jia, H. Ye, P. He, X. Lin, and L. You, "Selection of isomerization pathways of multistep photoswitches by chalcogen bonding," *Nature Communications*, vol. 14, no. 1, p. 7139, 2023.

[63] N. Duindam, M. van Dongen, M. A. Siegler, and S. J. Wezenberg, "Monodirectional photocycle drives proton translocation," *Journal of the American Chemical Society*, vol. 145, no. 38, pp. 21020–21026, 2023.

[64] A. Goulet-Hanssens, F. Eisenreich, and S. Hecht, "Enlightening materials with photoswitches," *Advanced Materials*, vol. 32, no. 20, p. 1905966, 2020.

[65] A.-L. Leistner and Z. L. Pianowski, "Smart photochromic materials triggered with visible light," *European Journal of Organic Chemistry*, vol. 2022, no. 19, p. e202101271, 2022.

[66] J. Volarić, W. Szymanski, N. A. Simeth, and B. L. Feringa, "Molecular photoswitches in aqueous environments," *Chemical Society Reviews*, vol. 50, no. 22, pp. 12377–12449, 2021.

[67] A. Mukherjee, M. D. Seyfried, and B. J. Ravoo, "Azoheteroarene and diazocine molecular photoswitches: Self-assembly, responsive materials and photopharmacology," *Angewandte Chemie International Edition*, vol. 62, no. 42, p. e202304437, 2023.

[68] R. Dorel and B. L. Feringa, "Photoswitchable catalysis based on the isomerisation of double bonds," *Chemical Communications*, vol. 55, no. 46, pp. 6477–6486, 2019.

[69] P. Kobauri, F. J. Dekker, W. Szymanski, and B. L. Feringa, "Rational design in photopharmacology with molecular photoswitches," *Angewandte Chemie International Edition*, vol. 62, no. 30, p. e202300681, 2023.

[70] Y. Liu, T. Wang, and W. Wang, "Photopharmacology and photoresponsive drug delivery," *Chemical Society Reviews*, 2025.

[71] S. Molla, J. Ahmed, and S. Bandyopadhyay, "All-photonic switching of a benzo [e]-fused dimethyldihydropyrene-azobenzene dyad in solid state for logic operations," *Chemical Science*, 2025.

[72] F. A. Jerca, V. V. Jerca, and R. Hoogenboom, "Advances and opportunities in the exciting world of azobenzenes," *Nature Reviews Chemistry*, vol. 6, no. 1, pp. 51–69, 2022.

[73] C. Fedele, T.-P. Ruoko, K. Kuntze, M. Virkki, and A. Priimagi, "New tricks and emerging applications from contemporary azobenzene research," *Photochemical & Photobiological Sciences*, vol. 21, no. 10, pp. 1719–1734, 2022.

[74] D. Keefer, F. Aleotti, J. R. Rouxel, F. Segatta, B. Gu, A. Nenov, M. Garavelli, and S. Mukamel, "Imaging conical intersection dynamics during azobenzene photoisomerization by ultrafast x-ray diffraction," *Proceedings of the National Academy of Sciences*, vol. 118, no. 3, p. e2022037118, 2021.

[75] A. K. Schnack-Petersen, M. Pápai, and K. B. Møller, "Azobenzene photoisomerization dynamics: Revealing the key degrees of freedom and the long timescale of the trans-to-cis process," *Journal of Photochemistry and Photobiology A: Chemistry*, vol. 428, p. 113869, 2022.

[76] J. Fregoni, G. Granucci, E. Coccia, M. Persico, and S. Corni, "Manipulating azobenzene photoisomerization through strong light–molecule coupling," *Nature communications*, vol. 9, no. 1, p. 4688, 2018.

[77] J. Fregoni, G. Granucci, M. Persico, and S. Corni, "Strong coupling with light enhances the photoisomerization quantum yield of azobenzene," *Chem*, vol. 6, no. 1, pp. 250–265, 2020.

[78] H. D. Bandara and S. C. Burdette, "Photoisomerization in different classes of azobenzene," *Chemical Society Reviews*, vol. 41, no. 5, pp. 1809–1825, 2012.

[79] S. Axelrod, E. Shakhnovich, and R. Gomez-Bombarelli, "Thermal half-lives of azobenzene derivatives: virtual screening based on intersystem crossing using a machine learning potential," *ACS Central Science*, vol. 9, no. 2, pp. 166–176, 2023.

[80] E. N. Cho, D. Zhitomirsky, G. G. Han, Y. Liu, and J. C. Grossman, "Molecularly engineered azobenzene derivatives for high energy density solid-state solar thermal fuels," *ACS applied materials & interfaces*, vol. 9, no. 10, pp. 8679–8687, 2017.

[81] B. Zhang, Y. Feng, and W. Feng, "Azobenzene-based solar thermal fuels: A review," *Nano-Micro Letters*, vol. 14, no. 1, p. 138, 2022.

[82] M. Kaźmierczak, S. Giannini, and S. Osella, "Photoinduced energy and electron transfer at graphene quantum dot/azobenzene interfaces," *Journal of Materials Chemistry C*, vol. 12, no. 1, pp. 143–153, 2024.

[83] A. Capretti, A. Lesage, and T. Gregorkiewicz, "Integrating quantum dots and dielectric mie resonators: a hierarchical metamaterial inheriting the best of both," *ACS photonics*, vol. 4, no. 9, pp. 2187–2196, 2017.

[84] J. Liu, H. He, D. Xiao, S. Yin, W. Ji, S. Jiang, D. Luo, B. Wang, and Y. Liu, "Recent advances of plasmonic nanoparticles and their applications," *Materials*, vol. 11, no. 10, p. 1833, 2018.

[85] B. García García, M. G. Fernández-Manteca, D. C. Zografopoulos, C. Gómez-Galdós, A. A. Ocampo-Sosa, L. Rodríguez-Cobo, J. F. Algorri, and A. Cobo, "Plasmonic and dielectric metasurfaces for enhanced spectroscopic techniques," *Biosensors*, vol. 15, no. 7, p. 401, 2025.

[86] H. Yu, Y. Peng, Y. Yang, and Z.-Y. Li, "Plasmon-enhanced light–matter interactions and applications," *npj Computational Materials*, vol. 5, no. 1, p. 45, 2019.

[87] E. Coccia and S. Corni, "Role of coherence in the plasmonic control of molecular absorption," *The Journal of Chemical Physics*, vol. 151, p. 044703, 07 2019.

[88] L. Bonatti, G. Gil, T. Giovannini, S. Corni, and C. Cappelli, "Plasmonic resonances of metal nanoparticles: atomistic vs. continuum approaches," *Frontiers in chemistry*, vol. 8, p. 340, 2020.

[89] T. Hutter, F. M. Huang, S. R. Elliott, and S. Mahajan, "Near-field plasmonics of an individual dielectric nanoparticle above a metallic substrate," *The Journal of Physical Chemistry C*, vol. 117, no. 15, pp. 7784–7790, 2013.

[90] A. I. Kuznetsov, A. E. Miroshnichenko, M. L. Brongersma, Y. S. Kivshar, and B. Luk'yanchuk, "Optically resonant dielectric nanostructures," *Science*, vol. 354, no. 6314, p. aag2472, 2016.

[91] F. P. García de Arquer, D. V. Talapin, V. I. Klimov, Y. Arakawa, M. Bayer, and E. H. Sargent, "Semiconductor quantum dots: Technological progress and future challenges," *Science*, vol. 373, no. 6555, p. eaaz8541, 2021.

[92] Y.-S. Park, J. Roh, B. T. Diroll, R. D. Schaller, and V. I. Klimov, "Colloidal quantum dot lasers," *Nature Reviews Materials*, vol. 6, no. 5, pp. 382–401, 2021.

[93] G. Rainò, M. A. Becker, M. I. Bodnarchuk, R. F. Mahrt, M. V. Kovalenko, and T. Stöferle, "Superfluorescence from lead halide perovskite quantum dot superlattices," *Nature*, vol. 563, no. 7733, pp. 671–675, 2018.

[94] A. Houtepen, E. Sargent, I. Infante, J. Owen, P. Green, R. Schaller, S. Bals, S. Zeiske, T. Stöferle, and Z. Hens, "Colloidal quantum dots for optoelectronics," *Nature Reviews Methods Primers*, vol. 5, no. 1, p. 42, 2025.

[95] F. T. Rabouw and C. de Mello Donega, "Excited-state dynamics in colloidal semiconductor nanocrystals," *Topics in Current Chemistry*, vol. 374, no. 5, p. 58, 2016.

[96] A. Sahu and D. Kumar, "Core-shell quantum dots: A review on classification, materials, application, and theoretical modeling," *Journal of Alloys and Compounds*, vol. 924, p. 166508, 2022.

[97] A. Ghaffarkhah, E. Hosseini, M. Kamkar, A. A. Sehat, S. Dordanihaghighi, A. Allahbakhsh, C. van der Kuur, and M. Arjmand, "Synthesis, applications, and prospects of graphene quantum dots: a comprehensive review," *Small*, vol. 18, no. 2, p. 2102683, 2022.

[98] K. Agarwal, H. Rai, and S. Mondal, "Quantum dots: an overview of synthesis, properties, and applications," *Materials Research Express*, vol. 10, no. 6, p. 062001, 2023.

[99] H. Kalt and C. F. Klingshirn, "Excitons in low-dimensional semiconductor structures," in *Semiconductor Optics 1: Linear Optical Properties of Semiconductors*, pp. 405–452, Springer, 2019.

[100] P. Wang, C. Jia, Y. Huang, and X. Duan, "Van der waals heterostructures by design: from 1d and 2d to 3d," *Matter*, vol. 4, no. 2, pp. 552–581, 2021.

[101] M. Chukeev, S. Zheng, E. Khramtsov, I. Ignatiev, S. Eliseev, V. Lovtcius, Y. P. Efimov, and M. Lozhkin, "Excitonic sensor of electric field in quantum-well heterostructures," *Physical Review B*, vol. 109, no. 23, p. 235305, 2024.

[102] Y. Chen, Q. Lin, H. Wang, and D. Li, "Interlayer excitons diffusion and transport in van der waals heterostructures," *Materials Futures*, vol. 4, no. 1, p. 012701, 2025.

[103] S. Misra, M. Stern, A. Joshua, V. Umansky, and I. Bar-Joseph, "Experimental study of the exciton gas-liquid transition in coupled quantum wells," *Physical Review Letters*, vol. 120, no. 4, p. 047402, 2018.

[104] P. R. Wrona, E. Rabani, and P. L. Geissler, "A pair of 2d quantum liquids: Investigating the phase behavior of indirect excitons," *ACS nano*, vol. 16, no. 9, pp. 15339–15346, 2022.

[105] G. Kiršanskė, P. Tighineanu, R. S. Daveau, J. Miguel-Sánchez, P. Lodahl, and S. Stobbe, "Observation of the exciton mott transition in the photoluminescence of coupled quantum wells," *Physical Review B*, vol. 94, no. 15, p. 155438, 2016.

[106] P. Andreakou, S. Poltavtsev, J. Leonard, E. Calman, M. Remeika, Y. Kuznetsova, L. Butov, J. Wilkes, M. Hanson, and A. Gossard, "Optically controlled excitonic transistor," *Applied Physics Letters*, vol. 104, no. 9, 2014.

[107] Y. Liu, K. Dini, Q. Tan, T. Liew, K. S. Novoselov, and W. Gao, "Electrically controllable router of interlayer excitons," *Science advances*, vol. 6, no. 41, p. eaba1830, 2020.

[108] Y. Peter and M. Cardona, *Fundamentals of semiconductors: physics and materials properties*. Springer Science & Business Media, 2010.

[109] C. Kittel and P. McEuen, *Introduction to solid state physics*. John Wiley & Sons, 2018.

[110] T. Schwartz, J. A. Hutchison, C. Genet, and T. W. Ebbesen, "Reversible switching of ultrastrong light-molecule coupling," *Physical review letters*, vol. 106, no. 19, p. 196405, 2011.

[111] J. A. Hutchison, T. Schwartz, C. Genet, E. Devaux, and T. W. Ebbesen, "Modifying chemical landscapes by coupling to vacuum fields," *Angewandte Chemie International Edition*, vol. 51, no. 7, pp. 1592–1596, 2012.

[112] A. Shalabney, J. George, J. a. Hutchison, G. Pupillo, C. Genet, and T. W. Ebbesen, "Coherent coupling of molecular resonators with a microcavity mode," *Nature communications*, vol. 6, no. 1, p. 5981, 2015.

[113] J. George, A. Shalabney, J. A. Hutchison, C. Genet, and T. W. Ebbesen, "Liquid-phase vibrational strong coupling," *The journal of physical chemistry letters*, vol. 6, no. 6, pp. 1027–1031, 2015.

[114] A. Thomas, J. George, A. Shalabney, M. Dryzhakov, S. J. Varma, J. Moran, T. Chervy, X. Zhong, E. Devaux, C. Genet, *et al.*, "Ground-state chemical reactivity under vibrational coupling to the vacuum electromagnetic field," *Angewandte Chemie*, vol. 128, no. 38, pp. 11634–11638, 2016.

[115] A. Thomas, L. Lethuillier-Karl, K. Nagarajan, R. M. Vergauwe, J. George, T. Chervy, A. Shalabney, E. Devaux, C. Genet, J. Moran, *et al.*, "Tilting a ground-state reactivity landscape by vibrational strong coupling," *Science*, vol. 363, no. 6427, pp. 615–619, 2019.

[116] B. Xiang, R. F. Ribeiro, M. Du, L. Chen, Z. Yang, J. Wang, J. Yuen-Zhou, and W. Xiong, "Intermolecular vibrational energy transfer enabled by microcavity strong light–matter coupling," *Science*, vol. 368, no. 6491, pp. 665–667, 2020.

[117] M. Barra-Burillo, U. Muniain, S. Catalano, M. Autore, F. Casanova, L. E. Hueso, J. Aizpurua, R. Esteban, and R. Hillenbrand, "Microcavity phonon polaritons from the weak to the ultrastrong phonon–photon coupling regime," *Nature communications*, vol. 12, no. 1, p. 6206, 2021.

[118] H. Zeng, J. B. Pérez-Sánchez, C. T. Eckdahl, P. Liu, W. J. Chang, E. A. Weiss, J. A. Kalow, J. Yuen-Zhou, and N. P. Stern, "Control of photoswitching kinetics with strong light–matter coupling in a cavity," *Journal of the American Chemical Society*, vol. 145, no. 36, pp. 19655–19661, 2023.

[119] J. Kuttruff, M. Romanelli, E. Pedrueza-Villalmanzo, J. Allerbeck, J. Fregoni, V. Saavedra-Becerril, J. Andréasson, D. Brida, A. Dmitriev, S. Corni, *et al.*, "Sub-picosecond collapse of molecular polaritons to pure molecular transition in plasmonic photoswitch-nanoantennas," *Nature Communications*, vol. 14, no. 1, p. 3875, 2023.

[120] G. Parolin, N. Peruffo, F. Mancin, E. Collini, and S. Corni, "Molecularly detailed view of strong coupling in supramolecular plexcitonic nanohybrids," *Nano Letters*, vol. 24, no. 7, pp. 2273–2281, 2024.

[121] M. Romanelli and S. Corni, "Identifying differences between semiclassical and full-quantum descriptions of plexcitons," *The Journal of Physical Chemistry Letters*, vol. 15, no. 37, pp. 9326–9334, 2024.

[122] K. Bennett, M. Kowalewski, and S. Mukamel, "Novel photochemistry of molecular polaritons in optical cavities," *Faraday discussions*, vol. 194, pp. 259–282, 2016.

[123] R. F. Ribeiro, L. A. Martínez-Martínez, M. Du, J. Campos-Gonzalez-Angulo, and J. Yuen-Zhou, "Polariton chemistry: controlling molecular dynamics with optical cavities," *Chemical science*, vol. 9, no. 30, pp. 6325–6339, 2018.

[124] J. Feist, J. Galego, and F. J. Garcia-Vidal, "Polaritonic chemistry with organic molecules," *ACS Photonics*, vol. 5, no. 1, pp. 205–216, 2018.

[125] P. A. Thomas, K. S. Menghrajani, and W. L. Barnes, "Cavity-free ultrastrong light-matter coupling," *The journal of physical chemistry letters*, vol. 12, no. 29, pp. 6914–6918, 2021.

[126] A. P. Ravishankar, F. Vennberg, and S. Anand, "Strong optical coupling in metallo-dielectric hybrid metasurfaces," *Optics Express*, vol. 30, no. 23, pp. 42512–42524, 2022.

[127] S. Choudhary, S. Iqbal, M. Karimi, O. Reshef, M. Z. Alam, and R. W. Boyd, "Strongly coupled plasmon polaritons in gold and epsilon-near-zero bifilms," *ACS photonics*, vol. 10, no. 1, pp. 162–169, 2023.

[128] W. Adi, S. Rosas, A. Beisenova, S. K. Biswas, H. Mei, D. A. Czaplewski, and F. Yesilkoy, "Trapping light in air with membrane metasurfaces for vibrational strong coupling," *Nature Communications*, vol. 15, no. 1, p. 10049, 2024.

[129] W. Sun, F. Yang, X. Shi, Y. Dong, R. Dai, Y. Jia, W. Xin, J. H. Li, Z. Wu, and Z. Liang, "All-dielectric quasi-bic metasurface with strong coupling control by adjusting the loss—potential for vibrational strong coupling," *Applied Physics Letters*, vol. 126, no. 26, p. 261703, 2025.

[130] S. A. Díaz, L. Giordano, J. C. Azcarate, T. M. Jovin, and E. A. Jares-Erijman, "Quantum dots as templates for self-assembly of photoswitchable polymers: small, dual-color nanoparticles capable of facile photomodulation," *Journal of the American Chemical Society*, vol. 135, no. 8, pp. 3208–3217, 2013.

[131] F. Grasselli, *Time–dependent propagation of quantum complexes: the case of indirect excitons in semiconductor heterostructures*. Ph.D. thesis, University of Modena and Reggio Emilia, https://morethesis.unimore.it/theses/available/etd-02032017-111315/, 2017.

[132] F. Grasselli, A. Bertoni, and G. Goldoni, "Classical and quantum dynamics of indirect excitons driven by surface acoustic waves," *Physical Review B*, vol. 98, no. 16, p. 165407, 2018.

[133] M. Yuan, K. Biermann, and P. V. Santos, "Manipulation of flying and single excitons by ghz surface acoustic waves," *AVS Quantum Science*, vol. 4, no. 3, 2022.

[134] A. Violante, K. Cohen, S. Lazić, R. Hey, R. Rapaport, and P. V. Santos, "Dynamics of indirect exciton transport by moving acoustic fields," *New Journal of Physics*, vol. 16, no. 3, p. 033035, 2014.

[135] R. A. Friesner, "Ab initio quantum chemistry: Methodology and applications," *Proceedings of the National Academy of Sciences*, vol. 102, no. 19, pp. 6648–6653, 2005.

[136] C. A. Flory, C. B. Musgrave, and Z. Zhang, "Quantum dot properties in the multiband envelope-function approximation using boundary conditions based upon first-principles quantum calculations," *Physical Review B—Condensed Matter and Materials Physics*, vol. 77, no. 20, p. 205312, 2008.

[137] A. Delgado, S. Corni, and G. Goldoni, "Modeling opto-electronic properties of a dye molecule in proximity of a semiconductor nanoparticle," *The Journal of Chemical Physics*, vol. 139, no. 2, p. 024105, 2013.

[138] F. Grasselli, A. Bertoni, and G. Goldoni, "Space- and time-dependent quantum dynamics of spatially indirect excitons in semiconductor heterostructures," *The Journal of Chemical Physics*, vol. 142, p. 034701, 01 2015.

[139] F. Grasselli, A. Bertoni, and G. Goldoni, "Exact two-body quantum dynamics of an electron-hole pair in semiconductor coupled quantum wells: A time-dependent approach," *Physical Review B*, vol. 93, no. 19, p. 195310, 2016.

[140] F. Grasselli, A. Bertoni, and G. Goldoni, "Time-dependent scattering of a composite particle: a local self-energy approach for internal excitations," *Physical Review B*, vol. 94, no. 12, p. 125418, 2016.

[141] M. P. Bircher, E. Liberatore, N. J. Browning, S. Brickel, C. Hofmann, A. Patoz, O. T. Unke, T. Zimmermann, M. Chergui, P. Hamm, U. Keller, M. Meuwly, H.-J. Woerner, J. Vaníček, and U. Rothlisberger, "Nonadiabatic effects in electronic and nuclear dynamics," *Structural Dynamics*, vol. 4, p. 061510, 01 2018.

[142] H. L. Luk, J. Feist, J. J. Toppari, and G. Groenhof, "Multiscale molecular dynamics simulations of polaritonic chemistry," *Journal of chemical theory and computation*, vol. 13, no. 9, pp. 4324–4335, 2017.

[143] Y. Zhang, T. Nelson, and S. Tretiak, "Non-adiabatic molecular dynamics of molecules in the presence of strong light-matter interactions," *The Journal of Chemical Physics*, vol. 151, no. 15, p. 154109, 2019.

[144] J. Fregoni, S. Corni, M. Persico, and G. Granucci, "Photochemistry in the strong coupling regime: A trajectory surface hopping scheme," *Journal of Computational Chemistry*, vol. 41, no. 23, pp. 2033–2044, 2020.

[145] O. Schalk and E. Tapavicza, *Photochemistry*, vol. 7. American Chemical Society, 2021.

[146] F. Jensen, *Introduction to computational chemistry*. John wiley & sons, 2017.

[147] R. M. Martin, *Electronic structure: basic theory and practical methods*. Cambridge university press, 2020.

[148] M. E. Casida, "Time-dependent density-functional theory for molecules and molecular solids," *Journal of Molecular Structure: THEOCHEM*, vol. 914, no. 1-3, pp. 3–18, 2009.

[149] C. Ullrich, *Time-dependent density-functional theory: concepts and applications*. Oxford University Press, 2012.

[150] R. E. Stratmann, G. E. Scuseria, and M. J. Frisch, "An efficient implementation of time-dependent density-functional theory for the calculation of excitation energies of large molecules," *The Journal of Chemical Physics*, vol. 109, pp. 8218–8224, 11 1998.

[151] T. Lu, *Multiwfn: A Multifunctional Wavefunction Analyzer*. Beijing Kein Research Center for Natural Sciences, 2017. Version 3.4.

[152] V. I. Klimov, *Nanocrystal quantum dots*. CRC press, 2017.

[153] G. Bastard, *Wave mechanics applied to semiconductor heterostructures*. New York, NY (USA); John Wiley and Sons Inc., 1990.

[154] P. Harrison and A. Valavanis, *Quantum wells, wires and dots: theoretical and computational physics of semiconductor nanostructures*. John Wiley & Sons, 2016.

[155] A. Orlandi, G. Goldoni, F. Manghi, and E. Molinari, "The effect of dielectric polarization-induced surface states on many-body configurations in a quantum dot," *Semiconductor science and technology*, vol. 17, no. 12, p. 1302, 2002.

[156] D. Bellucci, F. Troiani, G. Goldoni, and E. Molinari, "Neutral and charged electron-hole complexes in artificial molecules: Quantum transitions induced by the in-plane magnetic field," *Physical Review B—Condensed Matter and Materials Physics*, vol. 70, no. 20, p. 205332, 2004.

[157] M. Rontani, C. Cavazzoni, D. Bellucci, and G. Goldoni, "Full configuration interaction approach to the few-electron problem in artificial atoms," *The Journal of chemical physics*, vol. 124, no. 12, p. 124102, 2006.

[158] A. Ballester, J. Planelles, and A. Bertoni, "Multi-particle states of semiconductor hexagonal rings: Artificial benzene," *Journal of Applied Physics*, vol. 112, no. 10, p. 104317, 2012.

[159] A. Sitek, M. Urbaneja Torres, K. Torfason, V. Gudmundsson, A. Bertoni, and A. Manolescu, "Excitons in core–shell nanowires with polygonal cross sections," *Nano Letters*, vol. 18, no. 4, pp. 2581–2589, 2018.

[160] L. Biancorosso, P. D'Antoni, S. Corni, M. Stener, and E. Coccia, "Time-dependent quantum/continuum modeling of plasmon-enhanced electronic circular dichroism," *The Journal of Chemical Physics*, vol. 161, p. 214104, 12 2024.

[161] M. J. Frisch, G. W. Trucks, H. B. Schlegel, G. E. Scuseria, M. A. Robb, J. R. Cheeseman, G. Scalmani, V. Barone, G. A. Petersson, H. Nakatsuji, X. Li, M. Caricato, A. V. Marenich, J. Bloino, B. G. Janesko, R. Gomperts, B. Mennucci, H. P. Hratchian, J. V. Ortiz, A. F. Izmaylov, J. L. Sonnenberg, D. Williams-Young, F. Ding, F. Lipparini, F. Egidi, J. Goings, B. Peng, A. Petrone, T. Henderson, D. Ranasinghe, V. G. Zakrzewski, J. Gao, N. Rega, G. Zheng, W. Liang, M. Hada, M. Ehara, K. Toyota, R. Fukuda, J. Hasegawa, M. Ishida, T. Nakajima, Y. Honda, O. Kitao, H. Nakai, T. Vreven, K. Throssell, J. A. Montgomery, Jr., J. E. Peralta, F. Ogliaro, M. J. Bearpark, J. J. Heyd, E. N. Brothers, K. N. Kudin, V. N. Staroverov, T. A. Keith, R. Kobayashi, J. Normand, K. Raghavachari, A. P. Rendell, J. C. Burant, S. S. Iyengar, J. Tomasi, M. Cossi, J. M. Millam, M. Klene, C. Adamo, R. Cammi, J. W. Ochterski, R. L. Martin, K. Morokuma, O. Farkas, J. B. Foresman, and D. J. Fox, "Gaussian˜16 Revision B.01," 2016. Gaussian Inc. Wallingford CT.

[162] T. Lu, "A comprehensive electron wavefunction analysis toolbox for chemists, multiwfn," *The Journal of Chemical Physics*, vol. 161, no. 8, p. 082503, 2024.

[163] J. S. Dai, "Euler-rodrigues formula variations, quaternion conjugation and intrinsic connections," *Mechanism and Machine Theory*, vol. 92, pp. 144–152, 2015.

[164] S. M. Sze, Y. Li, and K. K. Ng, *Physics of semiconductor devices*. John wiley & sons, 2021.

[165] W. H. Press, *Numerical recipes 3rd edition: The art of scientific computing*. Cambridge university press, 2007.

[166] D. V. Talapin, J.-S. Lee, M. V. Kovalenko, and E. V. Shevchenko, "Prospects of colloidal nanocrystals for electronic and optoelectronic applications," *Chemical reviews*, vol. 110, no. 1, pp. 389–458, 2010.

[167] X. Chen, X. Lin, L. Zhou, X. Sun, R. Li, M. Chen, Y. Yang, W. Hou, L. Wu, W. Cao, *et al.*, "Blue light-emitting diodes based on colloidal quantum dots with reduced surface-bulk coupling," *Nature Communications*, vol. 14, no. 1, p. 284, 2023.

[168] E. Madden and M. A. Zwijnenburg, "Quantum dot or not? the effect of ligands on the nature of excitations in cds nanoparticles," *Nanoscale*, 2026.

[169] D. López Díaz, G. Gil, S. Corni, and G. Goldoni, "Hybrid configuration interaction: A multiscale, non-perturbative approach for molecule–nanoparticle nanohybrids." Manuscript in preparation, 2025.

[170] O. Madelung, *Semiconductors: data handbook*. Springer Science & Business Media, 2004.

[171] S. Shokhovets, O. Ambacher, B. K. Meyer, and G. Gobsch, "Anisotropy of the momentum matrix element, dichroism, and conduction-band dispersion relation of wurtzite semiconductors," *Phys. Rev. B*, vol. 78, p. 035207, Jul 2008.

[172] National Center for Biotechnology Information, "Pubchem compound summary for cid 66868, porphyrin," 2025. Retrieved August 10, 2025.

[173] J. Charry and A. Tkatchenko, "van der waals radii of free and bonded atoms from hydrogen (z= 1) to oganesson (z= 118)," *Journal of Chemical Theory and Computation*, vol. 20, no. 17, pp. 7469–7478, 2024.

[174] T. Fransson, T. Saue, and P. Norman, "Four-component damped density functional response theory study of uv/vis absorption spectra and phosphorescence parameters of group 12 metal-substituted porphyrins," *Journal of Chemical Theory and Computation*, vol. 12, no. 5, pp. 2324–2334, 2016.

[175] D. López Díaz, G. Gil, S. Corni, and G. Goldoni, "Exciton-driven photoisomerization in photoswitch–quantum dot nanohybrids," *Submitted to Nanoscale*, 2025. Under peer review.

[176] A. L. Efros, "Luminescence polarization of cdse microcrystals," *Physical Review B*, vol. 46, no. 12, p. 7448, 1992.

[177] J. P. Malhado, M. J. Bearpark, and J. T. Hynes, "Non-adiabatic dynamics close to conical intersections and the surface hopping perspective," *Frontiers in chemistry*, vol. 2, p. 97, 2014.

[178] H. Nakamura, *Nonadiabatic transition: concepts, basic theories and applications*. World Scientific, 2012.

[179] D. López Díaz, F. Grasselli, A. Bertoni, and G. Goldoni, "Correlated transport of spatially indirect excitons driven by surface acoustic waves in the presence of impurities." Manuscript in preparation, 2025.

[180] J. M. Pietryga, Y.-S. Park, J. Lim, A. F. Fidler, W. K. Bae, S. Brovelli, and V. I. Klimov, "Spectroscopic and device aspects of nanocrystal quantum dots," *Chemical reviews*, vol. 116, no. 18, pp. 10513–10622, 2016.

[181] D.-E. Zacharioudaki, I. Fitilis, and M. Kotti, "Review of fluorescence spectroscopy in environmental quality applications," *Molecules*, vol. 27, no. 15, p. 4801, 2022.

[182] E. O. Odewale, S. T. Wanasinghe, and A. S. Rury, "Assessing the determinants of cavity polariton relaxation using angle-resolved photoluminescence excitation spectroscopy," *The Journal of Physical Chemistry Letters*, vol. 15, no. 21, pp. 5705–5713, 2024.

[183] G. Schinner, E. Schubert, M. Stallhofer, J. Kotthaus, D. Schuh, A. Rai, D. Reuter, A. Wieck, and A. Govorov, "Electrostatically trapping indirect excitons in coupled in x ga 1-x as quantum wells," *Physical Review B—Condensed Matter and Materials Physics*, vol. 83, no. 16, p. 165308, 2011.

[184] F. W. Olver, *NIST handbook of mathematical functions hardback and CD-ROM*. Cambridge university press, 2010.